Department of Material Science

PhD program: Material Science and Nanotechnology Cycle: XXXIII

Curriculum in (se presente / if it is) _____

Single photon sources integrated on Ge Mie resonator fabricated by solid state dewetting

Surname: Toliopoulos Name: Dimosthenis

Registration number: 835511

Tutors: prof. Sanguinetti Stefano and prof. Massimo Gurioli

Coordinator: prof. Bernasconi Marco

ACADEMIC YEAR 2017 – 2020

Thesis Title: Single photon sources integrated on Ge Mie resonator fabricated by solid state dewetting

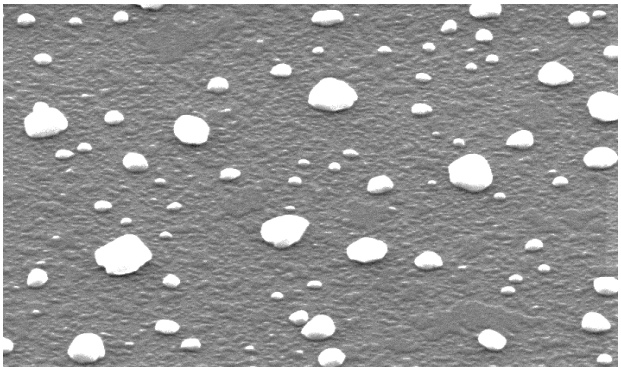

Supervisors: Prof. Stefano Sanguinetti

Prof. Massimo Gurioli

Candidate: Dimosthenis Toliopoulos

The research was supported by the funding from the European Union's Horizon 2020 research and innovation program under the Marie Skłodowska-Curie grant agreement № 721394.

To my pappou…

Abstract

The following Ph.D. thesis summarizes the work that has been made aiming at the fabrication and characterization of quantum emitters integrated inside Ge nano-island on Si substrates.

We choose to induce localized Ge impurities centers inside a thin layer of $Al_{0.25}Ga_{0.75}As$ epitaxially grown on Ge islands acting as dielectric Mie Resonators (MR's). These centers are working as light sources, capable of single photon emission and quantum entanglement properties. Fabrication of the Ge islands was done by solid state dewetting in an ultra-high vacuum environment, obtaining both amorphous and monocrystalline islands, with sizes ranging from 50 to 500 nm. These islands are also photonic Mie-resonators enhancing light-matter interaction and steering the localized defects emission, acting as dielectric nanoantennas. The experiments, show some emission light but still the light matter interaction is not yet achieved.

This thesis exploits molecular beam epitaxy, solid state dewetting and electron assisted lithography for realizing patterned samples. Many different characterization methods have been used to assess the quality of the fabricated samples. We use morphological characterization via scanning electron microscopy (SEM) and atomic force microscopy (AFM). Optically, we characterized the Mie resonators by dark field (DF) spectroscopy to ensure their photonic mode appearance. Also, the crystallinity of the Ge seeds was investigated by RAMAN spectroscopy. In the end, the optical response of the samples will be tested by micro and macro Photoluminescence, time-resolved measurements, and auto-correlation measurements to assess the quantum nature of the emission at low temperatures.

Towards our goal we faced three main different topics: i) the growth of Ge nanoisland via solid state dewetting, ii) the optimization of the photonic response of semiconductor Mie resonators by engineering the geometry of the substrates, iii) the integration of III-V layers on Ge islands and the observation of interesting associated defects. Each of these aspects is described in detail in chapters 3, 4 and 5. During my secondments at UNIFI, I had also been involved in a quite different approach towards the deterministic realization of quantum emitters integrated beneath a glass nanoantenna, an activity which led to article submission, but it is not reported in this thesis.

Περίληψη

Η παρούσα διατριβή συνοψίζει τα συμπεράσματα πειραμάτων που πραγματοποιήθηκαν στην ανάπτυξη και τον χαρακτηρισμό πηγών ατομικών φωτονίων πάνω σε υποστρώματα πυριτίου. Εντοπισμένες παραπλεγματικές θέσεις μέσα στον ημιαγωγό, μπορούν να λειτουργούν σαν πηγές φωτός, ικανές για εκπομπή μοναδιαίων φωτονίων και κβαντική διεμπλοκή. Αυτοί οι πομποί φωτονίων βρίσκονται ενσωματωμένοι μέσα στον AlGaAs ημιαγωγό ενώ ταυτόχρονα είναι συνδεδεμένοι με νανο-σωματίδια φτιαγμένα από Γερμάνιο, επίσης καλούμενα ως Mie-ενισχυτές. Η ανάπτυξη των σωματιδίων Γερμανίου, πραγματοποιείται με θερμική ανόπτηση λεπτών υμενίων γερμανίου που βρίσκονται πάνω σε υπόστρωμα πυριτίου και μέσα σε θάλαμο υψηλού κενού σε υψηλές θερμοκρασίες, μια τεχνική που λέγεται αποδιαβροχή. Μέσω της αποδιαβροχής είναι δυνατόν να φτάσουμε σε μονοκρύσταλλους, ιδανικό για επιταξιακή ανάπτυξη υψηλής ποιότητας III/V ημιαγωγό, μέσω στον ίδιο θάλαμο. Οι πηγές φωτός ενσωματωμένες με τους Mie-

ενισχυτές, προωθούν την αλληλεπίδραση του φωτός με την ύλη και την πιθανότητα μοναδιαίων πηγών φωτός. Η ενοποίηση της αλληλεπίδρασης του φωτός με την ύλη επιτυγχάνεται με την ύπαρξη του Γερμανίου σε παραπλεγματικές θέσεις του ημιαγωγού και την φωτονική ενίσχυση των νανοσωματιδίων. Οι συσκευές θα κατασκευαστούν με την λειτουργικοποίηση λεπτών υμενίων Πυριτίου και Γερμανίου ή και σε κάποιες περιπτώσεις χωρίς καν την χρήση λεπτών υμενίων.

Αργότερα, τα δείγματα θα χαρακτηριστούν μορφολογικά με ηλεκτρονική μικροσκοπία σάρωσης και μικροσκοπία ατομικής δυναμικής, για την κατανόηση της ατομικής δυναμικής, κινητικότητας και μορφολογίας της επιφάνειας των δειγμάτων. Αποτελέσματα των παρατηρήσεων σε δείγματα μετά την θερμική ανόπτηση, μελετώνται, οδηγώντας σε μια λεπτομερής ανάλυση της αποδιαβροχής των λεπτών υμενίων και την μορφολογία των νανοσωματιδίων. Παράλληλα, οι ενισχυτές-νανοσωματίδια χαρακτηρίζονται με μικροσκοπία σκοτεινού πεδίου για την επισφράγιση της εμφάνισης των φωτονικών δομών τους. Ύστερα, όταν η υψηλής ποιότητας κρυσταλλικότητα των δειγμάτων πιστοποιηθεί, τα ίδια τα νανοσωματίδια γίνονται και ο κατάλληλος φορέας για την κατάθεση ημιαγωγού ευθέως ζώνης χάσματος. Τέλος, η οπτική απόκριση των δειγμάτων εξετάζεται με την τεχνική της μικρο και μακρο-φωτοφασματοσκοπείας.

Contents

List of common Acronyms

AFM	Atomic Force Microscope
AlGaAs	Aluminium Gallium Arsenide
a-Ge	Amorphous Germanium
CMOS	Complementary metal–oxide–semiconductor
DF	Dark Field
EBL	Electron Beam Lithography
ED	Electric Dipole
FDTD	Finite-difference time-domain
HBT	Hanbury Brown and Twiss
IBL	Ion Beam Lithography
LDOS	Local Density of Optical State
LEPECVD	Low-Energy-Plasma-Enhanced-Chemical-Vapor Deposition
MBE	Molecular Beam Epitaxy
MD	Magnetic Dipole
MR’s	Mie Resonators
μ-PL	micro Photoluminescence
QI	Quantum Information
QC’s	Quantum Computers
QD’s	Quantum Dots
QIT	Quantum Information Technology
RIE	Reactive Ion etching

RHEED	Reflection High Energy Electron Diffraction
SOI	Silicon on Insulator
S.P.S	Single Photon Sources
S.S.D	Solid State Dewetting
SEM	Scanning Electron Microscope
UHV	Ultra High Vacuum

Chapter 1: Introduction and literature review

This first chapter aims to give an introduction to our projects, followed by sections reporting brief summaries of the state of the art in the several different topics that we crossed in our research path.

Quantum supremacy, at least when these lines were written, was one of the biggest events in the scientific community [1]. Big companies have announced their breakthroughs in developing quantum computers capable of performing significantly quicker and better than any other computer in the world [2]. Quantum processors, therefore, are expected to initiate the manufacturing of new concepts in science, such as biology, medicine, and new drug development. Powerful simulations on vaccine development could accelerate the research for covid-19 pandemic, which in 2020 was one of the major problems in all the globe. Moreover, a quantum computer could solve problems in the field of telecommunication, artificial intelligence methods, materials science, semiconductor physics, or even financial strategies, as well as algorithms for supply chain problems inefficiency [3]. We may see the benefits of conventional computers in our everyday life, however, there are problems that today's most powerful computers won't be able to tackle. For some complex challenges which go beyond a certain size, there is not enough computational power to face them, even if we use clusters or supercomputers. To be able to attempt to deal with some of these problems, we need to scale up computing capabilities and computational power [4].

Conventional computers to manipulate and store the information, rely on a

fundamental ability to utilize individual bits, which can exist as a binary 0 and 1 state. Quantum computers, on the other hand, are using quantum phenomena to handle information. Instead of bits that can be 0 or 1, they use the superposition of quantum states between |0> and |1> to generate the so-called quantum bits (or qubits). The main problem and the focus of the scientific community nowadays are to find different ways to create this qubit, the fundamental unit of quantum processors [5]. To work with qubits and keep them in a stable state for a long time, it is necessary to keep the quantum system very cold, close to absolute zero, since interaction with the thermal bath can introduce error and break the coherence of the qubits. Today, real quantum processors in big companies and laboratories such as GOOGLE [1] and IBM [6] are made by superconducting circuits that are kept at ultra-cold temperatures. They are already used by researchers from all over the world to test out algorithms for applications. However, it was only in 2019 when a quantum computer was able to run an algorithm faster than a classical computer, and that moment was called 'quantum supremacy' [7]. A quite important achievement, if we think that quantum computers a few years ago existed only in theory.

Quantum computers and Quantum Information Technology (QIT) will be a disruptive technology shortly. This goal imposes to seek for other strategies for realizing QIT based on semiconductors, which are at the core of classical computers. Breakthroughs in nano-photonics and semiconductor quantum emitters are quite promising for a QIT integrated into semiconductor technologies [8]. The leading topic in the field is on semiconductor quantum dots (QD's) with the ability to be grown on several substrates compatible with the existing CMOS technology [9]. Quantum dots can be grown in several substrates with different lattice parameters such as Silicon, Germanium [10], or Gallium Arsenide (GaAs), substrate orientations, but also with properties to be tuned in structural, optical, and electrical

modes. QD's act as artificial atoms in a solid state environment and their electronic and optical properties are intrinsically quantum. In this framework, the field of nano-photonics, which implements knowledge of photonics, quantum mechanics, material technology, and micro-scale device fabrication, is aimed to tailor on demand the properties of quantum light states emitted by QD's in view of a solid-state QIT development [11]. Several breakthroughs are still needed in device fabrication, as well in developing efficient quantum emitters with properties easily tunable, in enabling advanced experimental results and in fabrication of devices at the single/multiple quantum level. Recent technological, experimental, and theoretical findings in this field, have however demonstrated rapid potential for further development [12].

Nowadays, lots of applications utilizing QIT protocols are developed with optical fiber networks that produce commercial quantum cryptographic systems, where secure keys are encoded by quantum bits, which refers to a two-level quantum state. Indeed, the extended goal of QIT is to develop a massive network based on quantum processing, the so-called Quantum Internet, where information among quantum computers will be transported by photonic structure able to produce, process, and store qubits [13].

The first building block of QIT relies on quantum emitters of one single photon at a time [14]. There are several ways to produce these single-photon sources, which can be atoms and molecules or localized excitons in semiconductors (including the emerging field of 2D materials) [15]. Among them, semiconductor QD's are certainly the most extensively studied systems, but recently isolated impurity centers are attracting a lot of interest for their unique scalability associated with an intrinsic equivalence of all the centers.

Aiming to target semiconductor quantum emitters, one has to face the fact that the market of microelectronics nowadays is dominated by widespread silicon technology, as it provides an inexpensive and vigorous way to fabricate processors, light detectors, and photovoltaics [16]. Therefore, the integration of efficient light emitters on a silicon-based platform is a bet that the nanophotonics community needs to win [17]. However, a fully Si-based light source is extremely inefficient by the indirect bandgap of Si. By introducing ad-hoc emitting impurities can be a suitable alternative path to integrate light sources by epitaxial growth of direct gap semiconductor photonic devices on silicon [18, 19]. Although these demonstrations of quantum light emitters on a silicon substrate were not easily achieved for on-chip-integration. At the same time, light extraction from bulk semiconductors, spontaneous emission rate, and directionality can be major issues for the exploitation of light sources.

In the present thesis, we are going to address the topic of semiconductor QIT with a study of a special category of semiconductor single-photon sources, i.e. the lattice impurities inside the III-V semiconductor [18]. To follow the natural need for integration in silicon technologies we seek a method to embed them on a silicon wafer. In addition, the quest to tailor the properties of the emitted photons leads us to center this thesis on the advancement of a recently emerged approach of Mie resonators [20], based on the development of sub-wavelength Si and Ge islands. These dielectric particles present resonances in the visible and near-IR range and in analogy with metallic particles, this class of dielectric resonators present ultra-small photonic mode volumes [21]. These properties turn them into a suitable platform for light manipulation in nanoscale for semiconductor devices [22]. Specifically, the integration of dielectric Mie resonators with light emitters can enable the efficient

control of light-matter interaction, and therefore favoring the light collection with conventional optics [23].

The thesis will focus on the integration of light emitters on Si- and Ge- based small-sized crystalline seed-islands, formed via solid-state dewetting followed by epitaxial deposition of III-V compounds. For sake of illustration, Figure 1a reports scanning electron microscopy (SEM) images of a dewetted Si on insulator thin film. The formed islands can act both as seeds for the epitaxial regrowth as well as sub-wavelength antennas, as shown in Fig. 1a. Individual Si islands are formed via dewetting process on a silicon substrate. In Fig. 1b crystallinity of Si is demonstrated with the exposed facets visible. The use of 3D objects for hetero-epitaxy on small islands (~100-300 nm) is expected to drive the structure to an unstrained lattice parameter, producing dislocation-free material by interpreting unsteady dislocations. This will allow the monolithic integration of materials featuring a large lattice and thermal expansion coefficient mismatch in a sub-wavelength antenna.

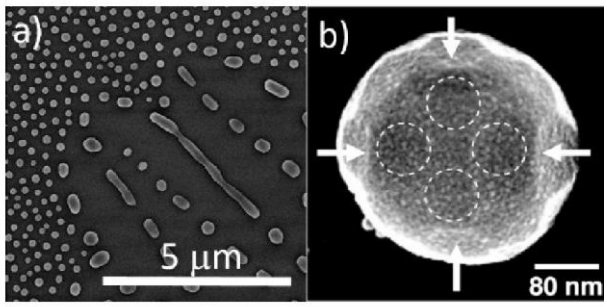

Figure 1: a) SEM image of a spontaneously dewetted Silicon on insulator substrate b) High-resolution SEM image of a dewetted Si island (Top view). Facets are highlighted by circles and arrows [24].

More specifically, for the current thesis experiments, investigations were done on deposition by molecular beam epitaxy (MBE) some III/V materials on dewetted structures for engineering the optical properties of $Al_{0.25}Ga_{0.75}As$ as Mie-resonators.

Small crystalline Ge particles ranging from 50 nm to 500 nm, have been obtained by spontaneous and assisted solid-state dewetting after the annealing of the thin Ge films on SiO_2/Si (001) [25]. These Ge islands have been then used as crystalline seeds for epitaxial growth of AlGaAs. $Al_{0.25}Ga_{0.75}As$ film has been deposited in situ on the top of Ge islands resulting in Ge atoms embedded in AlGaAs. Later, these Ge islands, except for their strong ability for resonances, are working also as providers of Ge atoms inside the bulk AlGaAs, creating, based on our speculations, some impurities inside the bulk. However, further investigations needed to be sure that Ge and other impurities are working as emission centers. In Fig, 2 we report a sketch of the system we aim to fabricate.

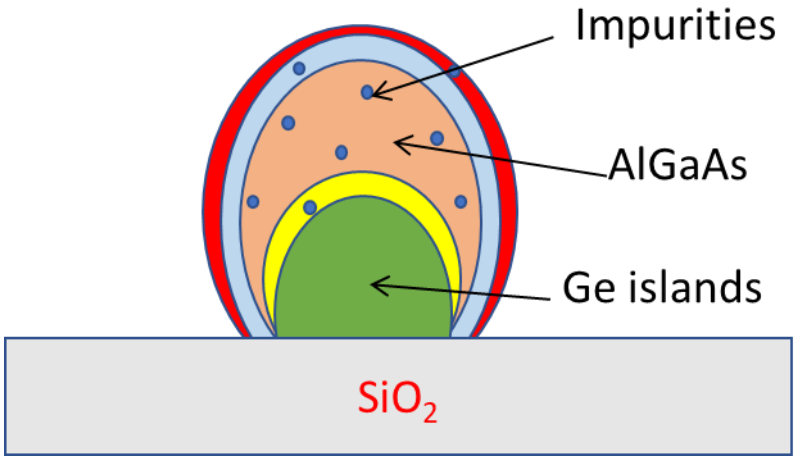

Figure 2: Schematic representation of impurity center inside the bulk material covering a Ge island. The chosen architecture of deposition was done to simulate a sandwich, where yellow and light blue layers are higher bandgap AlGaAs than the orange one with lower bandgap AlGaAs (i.e. in orange regions the Al content is reduced). In the end, the red layer is the GaAs capping layer. Ge atoms and molecules diffuse through the AlGaAs creating bulk impurities (blue points).

The impurities in the AlGaAs define localized states for electrons and holes, working as quantum emitters inside the cavity of bi-shell AlGaAs/Ge islands. In principle, we aimed to promote Ge impurities in the AlGaAs by diffusion from the

Ge seed, however, any defects can play the role of quantum emitters and we will show that it is possible to obtain a single photon source also by exploiting unintentional contamination. Very bright and sharp single photoluminescence lines are observed in micro photoluminescence. These emission lines behave very much as single excitons in QD's, but their realization is by far much easier since it does not require 3D nucleation or spatially selective doping as previously reported in the introduction. The photon antibunching is demonstrated by time-resolved Hanbury Brown and Twiss measurements, but their photonic nature is still under discussion.

All in all, in the present **chapter 1**, the concept of single photon, its characteristics, and the possibilities to develop single photon sources for QIT is discussed. In **chapter 2**, we address the experimental methods used to develop and characterize single photon sources. In **chapter 3,** the results of solid state dewetting is presented as a potential way to build easy, cheap, and efficient ways for seeds to deposit. **Chapter 4** refers to the characterization of nano-antennas, the so-called Mie resonators by studying the dark field spectroscopy of individual islands obtained by solid state dewetting. In **chapter 5** we discussed the possibility of impurities in semiconductors as single photon sources. Finally, during my secondments at UNIFI, I also had been involved in the laser writing of quantum dots integrated beneath dielectric nanoantennas, an activity which led to article submission, but it is not reported in this thesis.

In the following sections of this introductory chapter, we will briefly review the main topics of the state of the art in the existing literature for a better understanding of our thesis work.

1.1.1 Single Photon Sources

Why do we want to study single photon sources? As mentioned in the introduction before, single photon sources are the building blocks for QIT and among others, quantum dots are the ones dominating the market and the research as an ideal single photon source [26]. Another possibility is the use of color centers working as quantum dot-like single photon sources. Hereafter a non-exhaustive review of few important results in the field.

There is a wide range of semiconductor materials that can cover all desired wavelengths for different applications in QIT. For example, GaAs/AlGaAs Quantum Dots can emit around 700 – 900 nm, compatible with quantum memory and quantum repeater technology [27, 28] based on Rb and Cs atoms. The study of single-photon emitters operating at the telecommunication wavelength by many researchers and developers, revealed the exploration of the use of InAs quantum dots in the development of quantum computers and quantum information systems [29, 30]. InAs QD's can be embedded inside GaAs/AlGaAs Bragg reflectors, enabling a DBR that can be exploited to form a planar micro activity that improves its quantum dots emission [26, 31]. Bulu et al. in 2011, further indicate that the GaAs based InAs quantum dots can be capable of emitting high-brightness single-photon emission below 1000 nanometers. However, due to material limitations, it was hard to generate a wavelength of about 1.3 micrometers or longer.

Further extension of the emission wavelength from the quantum dots at telecommunication wavelength has been attempted by using a variety of methods that addresses different elements of the photon emitters. InGaAs, GaAs dot in a quantum well structure with a 30% indium content, strain engineered quantum dots, vertically coupled quantum dots, metamorphic structure, and InGaAs capping layer

are some of the methods proposed to mitigate the problem [32]. However, the bilayer quantum dots structure, i.e. a vertically coupled quantum dots, provide a reliable growth parameter that can be controlled depending on the application. For instance, high-density bilayer quantum dots have been grown to develop laser diodes of about 1.6 micrometers. Bulu et al. indicate that several studies have proposed the regulation of bilayer quantum dots to grow low QD's density to produce telecommunication band, single-photon sources [26]. The control of the interlayer strain coupling must be monitored closely to realize low-density bilayer quantum dots and proper distribution [32].

A second very famous category of single photon sources is colloidal quantum dots, which are the most used and easier to be fabricated, but are profoundly affected by blinking. Therefore, self-organizing single quantum dots with large gaps have been explored to replace the colloidal quantum dots because they are not affected by blinking [33]. Structures with epitaxy from different compounds have been demonstrated to have excellent single-photon emission capability at high temperatures. Therefore, most of the systems have been demonstrated to function appropriately at room temperature through electrical and optical pumping. The density of the photon hinders the selection process of a single excitonic line in the array, needed for a classic light observation [26]. However, scientists are working to address the issue through the formation of the etched structure, inserting a single quantum dot in a nanowire by masking the nano aperture in a transparent mask. Nevertheless, all the methods require low photon density to be effective as single photon sources.

Changing surface energy with thermal annealing has been proposed to produce an array of quantum dots with reduced density. The method is expected to facilitate two-dimensions to the three-dimension transformation of the strained layer

into a quantum dots ensemble [34]. The experimental application of the system produced a lateral density of about 4×10^{10} cm^2. However, the objects formed were not canonical Stranski Krastanov quantum dots [26]. Still, they only produced a flat nanoisland with average sizes of about 5 nanometers in the lateral direction and 50 nanometers in the vertical direction. The micro photoluminescence spectra demonstrated a narrow emission line that may be related to the fluctuation in the localized potential within the islands [26]. At a size above 10 nanometers, the exciton density states are equal to that of the quantum well, which can prevent the generation of indistinguishable photon generation [33].

However, QD's serving as single photon sources can present several drawbacks [35] when coming to applications, such as the enhancements of radiative lifetime along with the efficiency of light extraction from QD's in a cavity, and secondly, the interference between photons from different sources. To overcome this limitation, single photon sources from individual impurity centers were used. In particular, the topic has been studied since the beginning of the '00s as an alternative approach emerged by using anti-bouncing photons from the bulk diamond crystals at room temperature [36]. Extrinsic color centers are embedded inside the bulk sample, making it a good candidate to antagonize the QD's as single photon sources for quantum applications. However, to maximize the efficiency, the coupling of the impurity center with a cavity is needed in order to emit in a single mode. Single nitrogen vacancy centers are another well-studied field for generating single photon sources from defects in diamond [37]. A substitutional N atom inside the diamond lattice position works as individual impurity centers. However, introducing more N atoms inside the lattice on purpose, serve in a brighter luminescence from the sample. The unconventional light extracted from such a class of samples lies in the red and near IR region. The concept of single photon sources from individual centers is

presented also in a ZnSe quantum-well structure [38]. In this case, nitrogen impurity centers inside a quantum well can trigger single photon emission under continuous excitation laser source. However, even if these light sources exhibit anti-bunching behavior, still the autocorrelation measurements suffer for limited demonstration of $g^{(2)}$ (τ) below 0.2. Accordingly, impurity centers inside the ZnSe bulk from individual Te atoms demonstrate single photon source characteristics [39]. Sharp emission originating from the Te impurity centers indicates quantum single photon entities. Entangled pairs of photons, from an individual impurity generated source, were demonstrated in the ZnMgSe/ZnSe quantum-well nanostructures [40]. Impurity centers inside GaAs were studied by introducing N vacancies as single photon sources inside the GaAs matrix [41]. The bright N centers courses tend to show faster radiative decay rates. Although, the most important category of impurities for the current thesis are the Ge impurity centers inside the AlGaAs matrix which first studied in 2012 [35]. Epitaxial growth by MBE of AlGaAs 30% epilayer on top of Ge and Si substrates, present unconventional contamination of Ge and Si atoms through diffusion inside the III-V matrix. Each of the Ge or Si atoms behave as a single photon source, very much like the single excitons found on QD's. It is worth mentioning that Ge or Si impurities working as single photon sources, do not require any 3D nucleation like the one we find in QD's case or even any intentional introduction of N and Te centers in the matrix. Hanbury Brown and Twiss measurements were used to demonstrating the antibunching behavior of the bright and sharp photoluminescence lines in such kind of systems. The single photon character is, however, demonstrated $g^{(2)}(\tau=0)$ not far below the limit of 0.5. The same approach is demonstrated in the use of Ge and Si substrates to introduce unavoidably Ge and Si atoms inside the epitaxially developed AlGaAs layers [42]. The sharp lines that were found by micro-photoluminescence were attributed to the exciton and bi-

exciton contribution by time resolved and power measurements. Finally, sharp lines (40 μeV) were still found even at a higher temperature (at 70K) confirming that there is good thermal stability in this class of impurity centers for the application of single photon emitters. Detailed investigation on the literature in this kind of single photon emitters was the purpose for this Ph.D thesis.

1.1.2 Single Photon Sources made by Molecular Beam Epitaxy

How are we able to build single photon sources? Historically the first way to make a highly efficient semiconductor single photon source was by the Molecular beam epitaxy (MBE) method. MBE is based on the interaction of a beam of atoms with a crystal surface at a high temperature inside an ultra-high vacuum environment. Molecular beam epitaxy is adapted to have a consistent and precise deposition. There are several types of molecular beam epitaxy used in nanotechnology. Gas source molecular beam epitaxy uses hydride materials such as arsine and phosphine. Metalorganic molecular beam epitaxy uses metalorganic compounds such as trimethylgallium and trimethylindium [43]. However, the reliable source molecular beam epitaxy uses an effusion cell generated through the evaporation of ultra-pure source materials in a crucible. The effusion cell produces the molecular beams that are then directed on the heated substrate. The temperature within the effusion cells is used to adjust the flux intensity of the beam produced. The deposition chambers are equipped with a pump system that records the pressure in the 10^{-11} Torr range [44]. The molecular beam epitaxy growth is often facilitated by the reaction of the beam with a crystalline substrate that is maintained at high temperatures [45]. However, the ultra-high vacuum pressure is needed for the reduction of the background contaminant that may be incorporated into the solid. Furthermore, vacuum conditions allow atoms to have a mean free path longer than the distance

between the source cell and the substrate [32]. Shutters can be used to control the deposition process of the atoms even at the level of single layer deposition. The development of interfaces in the range of one atomic layer can be developed by the shutter in front of the orifice by opening it and closing it within a shorter time compared to the growth time of the molecular beam epitaxy. Consequently, opening and closing different shutters can be used to control the heterostructure multilayer composition and doping elements.

Precise control of composition, doping, and material quality, made possible the fabrication of GaAs/AlGaAs lasers, making them usable at room temperature, has drastically improved the production of semiconductor optoelectronic devices. The efficiency of the devices has further been improved through the provision of electrical and optical confinement through the heterojunction [46]. The production of compound semiconductors with a definite composition profile, promises to improve optoelectronic technology. However, the molecular beam epitaxy may be used to obtain high quality and high precision epitaxial growth. The capability of layered epitaxies presents an opportunity to develop devices with a multilayer epitaxial structure tailored to meet specific needs. For instance, the development of semiconductors quantum dots has made it possible to demonstrate quantum computing principles [46].

1.1.3 Single photon detection

How do we know that our light source is a single photon source? The answer relies on the measurement of photon statistics and in particular to the pure quantum effect of photon antibunching by second order autocorrelation $g^{(2)}(\tau)$ experiments. The relation from where the statistics of the number of photons coming out of the sources is calculated by eq. (1.1):

$$g^{(2)}(\tau)=\frac{\langle I(t)\cdot I(t+\tau)\rangle}{\langle I(t)\rangle^{2}} \qquad (1.1)$$

where τ is time delay. For $g^{(2)}(0)= 2$ then the light source is a single mode thermal source with various frequencies; an example of such a case is the blackbody where the photon stream is bunched. A coherent light, such as a laser beam, gives $g^{(2)}(0) = 1$, since the photons are all in phase, resulting in a Poissonian distribution. For a quantum source $g^{(2)}(0)<1$, and more specifically for a perfect single photon source, $g^{(2)}(0)=0$, and in the case of two photon generation, the $g^{(2)}(0) =0.5$. Each distribution case is reported by Fig. 3 for a) coherent, b) antibunching, and c) bunching light source.

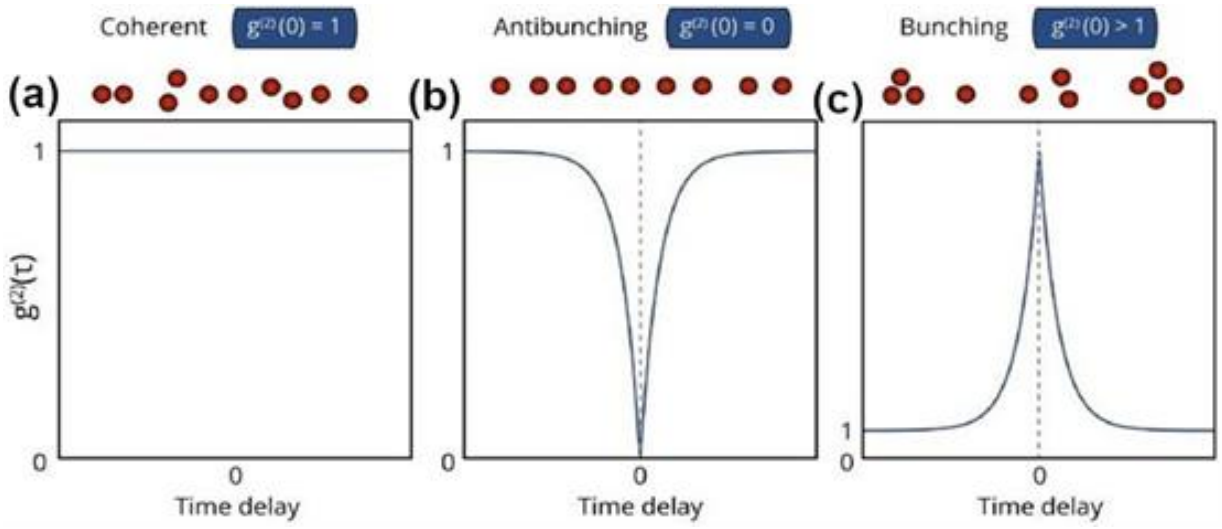

Figure 3. Auto-correlation functions of (a) a coherent light source such as a laser, (b) a single photon source, and (c) a thermal light source like a blackbody.

A peculiar type of set-up that originally was used for astronomical observations is used to measure the autocorrelation function as we can see in Fig. 4, named Hanbury Brown and Twiss interferometer, by the names of the astronomers [47]. Here we used a modified version for testing the photon antibunching. A pulsed

laser usually in the UV spectral region is split in half by a beam-splitter for exciting the sample with two pulses delayed by a time interval τ. The PL signal is also split and two detectors, placed after the PL splitting, are counting the number of emitted photons that follow each path. Note that an electronic delay τ1 is introduced in the signal from one detector in order to measure also the coincidence with inverted time. Therefore, a correlation histogram of events occurring on detectors with time difference dependence is slowly built. The number of events recorded from the detectors for time difference τ2 is proportional to the probability of the presence of a single photon when t = τ2 given the presence of a photon at time t = 0.

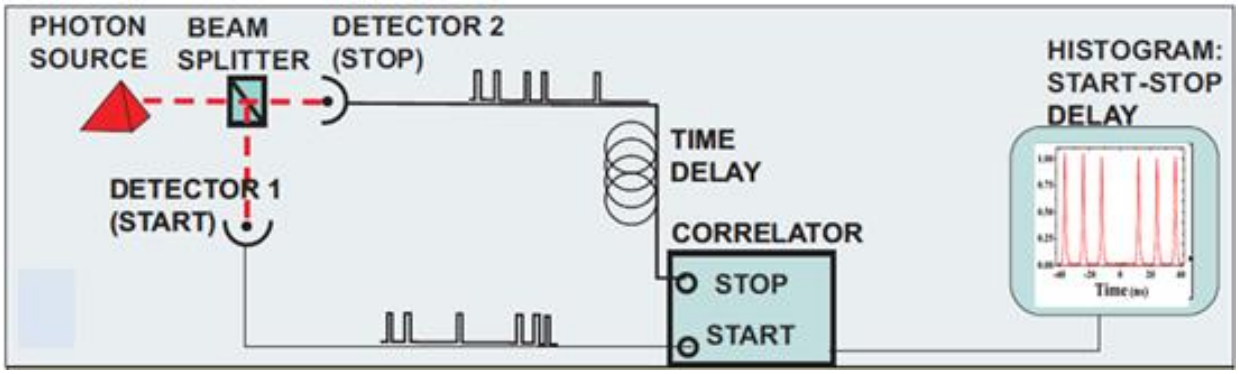

Figure 4. Scheme of the $g^{(2)}(\tau)$ Hanbury Brown and Twiss autocorrelation measurements setup. A photon source, usually a pulsed UV laser excites a sample with single photon emitters. Then, the emitted signal from the sample is splinted with a beam-splitter. Later two single photon detectors are placed, with the difference that one of them has a time delay line with long optic fiber. Finally, the histogram of the time delay between photons detected is developed.

Another way to perform the auto-correlation measurements is by using a continuous laser as an excitation source for the single photon sources on the sample. The histogram, this way can be considered to look like the one from Fig. 3 (b) and eventually gives information on the exciton lifetime. The drawback is that the value of $g^{(2)}(0)$ depends on the detector temporal resolution and deconvolution is needed to extract the purity of the single photon emitter.

1.2.1 Nano-antennas and Mie Resonators

Why do we use nano-antennas via the Mie resonators? Light management in nanoscale is one of the most studied fields in optics technology. Nanophotonics captured the scientific community's interest in the last years with breakthroughs such as photonic cavities and antennas in the nanoscale and their integration with light [48].

Joining a single emitter with a suitable cavity/antennas is essential in many applications due to the benefits generated from the coupling [49]. Emitter inside a semiconductor cavity is a standard method for light manipulation in nanoscale. Coupling the emitter with a cavity improves the quantum efficiency, increases the repetition rate, and makes the photons more distinguishable upon reception [50]. Photons emitted from quantum dots are not directional, and coupling it with a cavity transforms the emission to cavity mode that can be controlled with ease. Cavity mode also presents a better polarization that is essential for some linear optical quantum computing systems. For instance, the modern semiconductors are majorly made out of micropillar cavities and microdisk cavities with resonator structures that are made of complete spectral and spatial mode profiles. The strong coupling in the photons improves the efficiency of the single-photon source, with the efficiency almost coming close to unity [51]. The indistinguishability of the photons can be surpassed through the Purcell effect and is essential in matching the spontaneous emission of the coupling regime to fix the rate by developing a strong coupling [52]. These planar structures are made to take advantage of the strong lateral and vertical light confinement from single emitters, which leads to high-quality factor (Q) but within relatively large volume (V) cavities. Therefore, a perfect single-photon source with a strong coupling can be used to enhance efficiency in a quantum network system.

The need to reduce the modal volume drove the research towards sun-micrometer resonators. Metallic nanoparticles offer a solution where the volume mode can be significantly smaller with extremely small nanoparticles but they suffer from serious ohmic losses because of strong absorption, and therefore small quality factor Q. In both cases, planar cavities and metallic nanoparticles Purcell factor is limited, and therefore there is an alternative path, where all-dielectric nanoparticles are used [51]. Dielectric nanoantennas are an alternative solution to plasmonics to direct the light of an emitter to the far-field and they have much lower ohmic losses [20].

Applications with metallic nanoparticles formulate cavities for light interference, like Fabry-Perot or even more complex geometries. In other words, nanophotonics is the area where the resonances and light interference are met. We succeed at this interference by inserting mirrors and object-like mirrors in nanoscale to manipulate light. The nanoantennas provide a reliable way to transfer directly propagated radiation into a localized subwavelength mode at a nanoscale. Therefore, the technology can be used in a variety of systems with a remarkable output and reliability. The original antennas operated through the production of radio waves through the oscillating of current. The size of the antenna increases with an increase in range and the number of signals modulated. The initial designs of nanoantenna used the metallic nanorods, which were then arranged in a way that satisfied all the properties of radiofrequency antennas.

The metallic nano-antennas suffer from severe quenching of the fluorescence emissions that often arise from the generation of high losses. Furthermore, the interband transmission also leads to increased metallic absorption that leads to heating of the antenna and its environment. So, the use of dielectric nanoparticles

materials has been identified as a significant way to reduce the heat generated by the nanoantenna [53].

In order to overcome these drawbacks, a new type of all-dielectric resonators is rapidly used for application in light manipulation, called Mie resonators. Located in-between photonic crystal cavities and plasmonic nanoparticles, Mie resonators offer an alternative way to enhance light-matter interaction at the nanoscale. Mie Resonators will be discussed in the next section in more depth.

1.2.2 All-dielectric Resonators and Mie resonances

Photonic crystals resonators present resonances with high Q factors but large volumes mode, while metallic nanoparticles are offering small Q factors in very small volumes, but losses in plasmonic optical cavities are a limitation that sabotages their performances. As a viable compromise, dielectric Mie resonators can substitute both planar cavities and plasmonics as an alternative way to enhance light-matter interaction in nanoscale [54]. The dielectric resonators antenna is a well-established technology used in the propagation and reception of microwaves. Together with other nanoantenna technology, dielectric resonators have been advanced for the propagation of higher frequencies and even visible optics. The dielectric nanoantennas are made by high-index semiconductor materials, like Si or Ge and they support resonances near or below the frequency range of the combining material [24].

The distribution of the electromagnetic field around the nanoparticles led to denomination modes via a multipolar expansion. The two most important modes are the denominated magnetic dipole, known as the first Mie-resonance, and the electric dipole, which is the second Mie resonance accordingly as shown in Fig. 5a below (from Ref. [20], supporting information). Fig. 5b demonstrates the electric and

magnetic field rise around a Mie resonator. We can see the electric and magnetic near field distribution for the two modes from a dielectric nanoparticle.

The development of dielectric resonators has been improved by the development of nanofabrication techniques that have been developed to manipulate a variety of materials that can be used in the development of the antennas [24]. Dielectric resonators have been found useful in a variety of fields due to their two significant advantages. As an example, if made of highly permeable materials, the dielectric resonators can support a variety of resonance modes, making them very versatile radiation materials [53]. Dielectric resonators have been found to have high efficiency, reduced size, and efficient excitation methods that make them desirable in multiple applications such as the development of pure magnetic resonance.

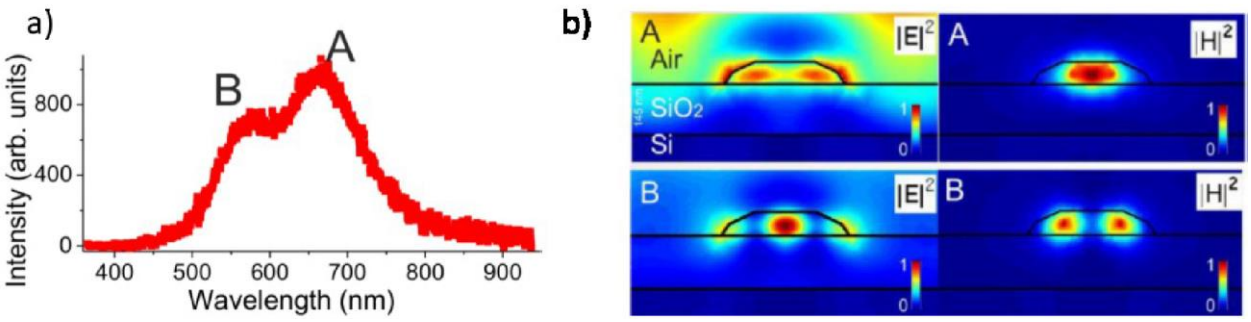

Fig. 5: a) Dark field scattering spectrum of an individual silicon-based Mie resonator obtained by dewetting. A and B, highlight respectively the dipolar magnetic and the dipolar electric resonances. b) Reconstruction of the electric $|E|^2$ and magnetic $|H|^2$ field intensity at the wavelength of A and B resonances [20].

There is a significant development in the production and use of dynamically controlled optical response of Mie resonators for optical and signal processing. Some of the state-of-the-art applications consist of antireflective coatings with the utilization of ordered nanodisks for light interaction between the disks [22].

Moreover, dielectric resonators can be used as detectors [55] or even dielectric metasurfaces for optical elements [56]. More sophisticated applications consist of topological edge states [57], electromagnetically induced transparency [58], and subwavelength resolution imaging [59]. Advancements also in electric tuning due to it have a broader range and better switching speed [53]. However, there is a strong proposal for the electric tuning of metamaterials based on plasmonic nanostructures. The tuning method relies on layers of semiconductors made of graphene or electromechanical deformation of nanomaterials. All in all, the advancement of optical nanoantenna is promising to improve the field of nanotechnology that is taking route in many areas of electronics development [53].

In addition, the dielectric particles still support Mie resonance which may be used to enhance the nanoantenna's local nearfield intensity [60]. The presence of electric and magnetic modes presents an opportunity to develop products with tailored light scattering [60]. Modification of the light scattering, together with the chirality of the light emitted, may enhance the decay rate of the nearby emitters, a property that may be used to improve the directivity of the dielectric optical transmitters.

1.2.3 Working Principles of nano-resonators

Coupling between quantum emitters and nanoscale optical resonators have been optimized to reduce the impact of spontaneous photon emissions. The idea is similar to telecommunication via radio frequencies, which are optimized to reduce the power emitted by the subwavelength electric bipolar emitters. In practice, most of the antennas are designed to improve the local density of the electromagnetic field, enhancing the coupling process of the dipolar emitters in the nearfield [53]. The

coupling for the dipolar emitter in the near field is essential for the radiation of the waves in the far-field.

In quantum theory, Fermi's golden rule may be used to evaluate the spontaneous decay rate of the emitter with a weak coupling regime using eq. (1.2):

$$\Gamma = \frac{2}{3h\epsilon_o}\omega|P^2\rho(r,\omega) \text{ [53]} \quad (1.2)$$

Ƥ represents the electric dipole moment operator between the ground and the excited state of the emitter. ρ (r, ω) represents the local density of optical state (LDOS) at the r position of the emitter achieved within the frequency ω. The total local density denotes the cumulative electric field at the emitter. One of the main goals of nano-photonics is to tailor the LDOS to optimize the emission of a quantum source. This occurs not only by increasing the radiative rate via the Purcell effect but also via color filtering and emission steering, as discussed in the next section.

1.2.4 Practical Implementation of the Directional Nanoantenna

The implementation of dielectric resonators in the development of nanoantenna, imitating the traditional radiofrequency antennas, has been explored by a large number of researchers and developers. Materials with a wide array of dielectric permittivity may be implemented by tuning the real part of the dielectric constant to improve the quality factor of the resonance. Tuning of the dielectric can be done to develop a nanoantenna that can operate in areas where broadband and narrowband are required [53]. Spectral overlap of different multipolar modes may be achieved by the use of a broader Mie resonance because a large number of modes involved in the system allow for the development of a higher directivity capability.

In Ref. [61] the light scattering of Titania nano-sphere is given in Fig. 6. Note that the nanoparticles acquire structural colors depending on their size, which reveals sharp resonances, neat structural colors, and high directivity.

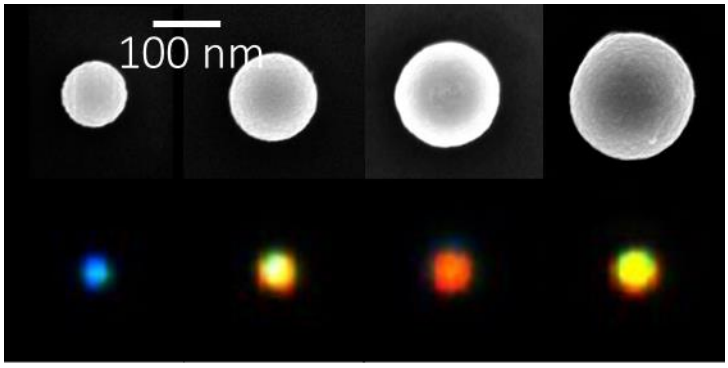

Figure 6: Scattering color profile of dielectric nanoparticles according to their size. Small size particles scatter in blue colors, while bigger islands more towards red [61].

Nanoantenna technology still has a vast potential of improving a variety of devices used for communication and other elements. One of the major devices that can be size reduction and improvement of antennas can be mobile phone and television [62]. The size and capabilities of the antennas have a considerable impact on the overall size and capabilities of mobile phones. Poor antenna limits the application of mobile phones as they cannot receive weak signals and send signals at the required intensity [63]. Likewise, large antennas lead to an increase in mobile phone sizes as they are majorly used for signal demodulation and modulation. Furthermore, the reduction of antenna size will open the field of nano communication devices that can be used for the development of small communication devices.

1.3.1 Solid State Dewetting

How we can fabricate all-dielectric Mie resonators? Among the popular techniques to develop suitable all-dielectric nanoparticle seeds for single-photon emission, is to manipulate the surface morphology of thin films. Several nano-patterning technologies (Fig. 7) such as Reactive Ion etching (RIE), Ion Beam Lithography (IBL), or Electron Beam Lithography (EBL) [22] may be applied to generate arrays of pillars or more complicated arrangements to form a metasurface. However, a purely top-down technique, in spite of its broad use and precision, is not appropriate for the integration of light emitters owing to the large defectivity that induces on the lateral walls of the etched structures. For this reason, we concentrate our attention on an emerging technique, solid state dewetting that allows forming disordered and ordered sub-micrometric islands acting as Mie resonators. The hybrid use of top-down patterning prior to dewetting and the bottom-up assembly of 3D structures provide the necessary precision in organizing the antennas and atomically smooth surfaces that minimize the surface defects.

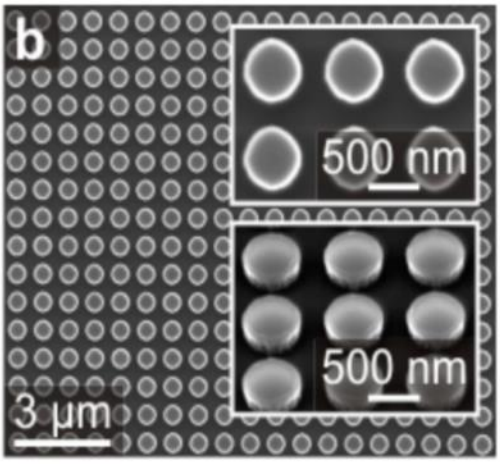

Figure 7: EBL and RIE nano-patterning on Si substrate with well-defined position of Si or Ge islands or disks [22].

Therefore, there is a need to describe some of the patterning techniques and their applications in nanotechnology and the development of electronics.

1.3.2 Solid & liquid state dewetting phenomenon

Among other techniques to achieve such kind of nano-patterning is a spontaneous phenomenon, so-called solid state dewetting or just dewetting. Dewetting can occur in liquid state of matter, such as when rain falling on a window may break down into smaller particles as its roles in a dirty window [64] (Fig. 8). However, dewetting may be undesirable as it leads to breakage of elements that should remain intact to have the desired shape and function [65]. For instance, dewetting in the paint may lead to poor surface finish. However, the process may be essential in some industrial applications where fast drying of fluids is desirable [66]. For example, in aviation, the impact of water on the fuselage should be minimized for the proper operation of the elements. As observed by Takenaka et al. [64], the fuselage is sprayed with anti-ice fluid that makes it non-wettable. In some cases, residues left by drying fluid may be undesirable. Therefore, a chemical may be used to remove the residue together with the fluid. For instance, dishwashers are specifically made to prevent the wetting of the dish surface.

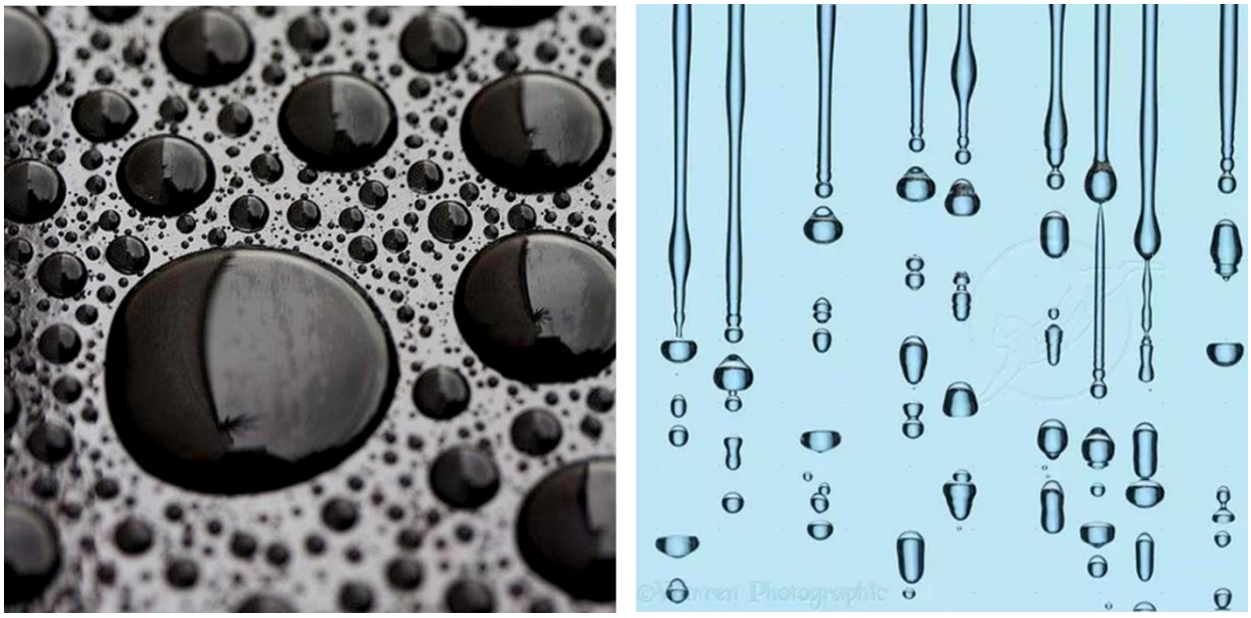

Figure 8: Left panel: Wetting layer of water droplets on a hydrophobic surface. Right panel: Liquid forming droplets after surpassing a certain neck size.

However, dewetting can also occur in the solid phase of the matter especially in thin films. The so-called solid-state dewetting is the process that breaks a continuous thin film into separate objects such as droplets and stripes. Thin films are in general in the metastable condition when they are deposited on a substrate. Thus, when they are treated at high temperatures, they tend to agglomerate forming arrays of nano-islands. The thin film, when perturbed, often rearrange into separate elements instead of forming a continuous surface. The whole process can occur below the melting temperature of the thin film, which means that the thin film is in solid state (i.e. solid state dewetting). The main player in this metamorphosis is the minimization of the total energy between the surfaces of the film and the substrate [67]. Thus, different behavior is observed with crystalline thin films of different materials with various substrates. In Fig. 9 a thin solid film is resting on top of the substrate and after the annealing solid state dewetting occurs resulting in individual

islands. Moreover, dewetting is accelerated when the thin film's thickness decreases, and is much easier for the dewetting process to start at a lower temperature [25].

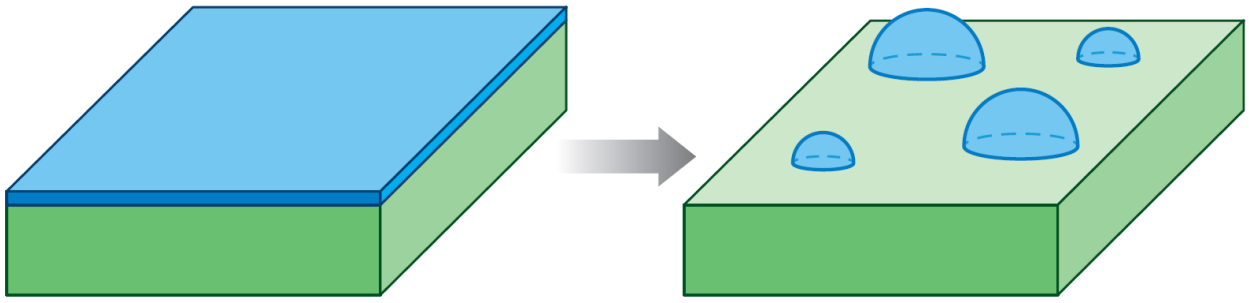

Figure 9: Solid-state dewetting of thin films can dewet to create isolated nanoislands. This occurs while the material remains in the solid state [67].

Thus, dewetting indeed has a wide variety of applications both at home, in research, and in an industrial setting. Biscarini et al. [68] indicate that most of the technological applications of dewetting require precise size control to improve the application of the particles generated. This control may result in a final arrangement of particles with predefined sizes and spatial distribution by Ion-beam nanopatterning [69]. Therefore, the process may be used instead of expensive and complicated lithographic processes, like those mentioned above.

Nevertheless, dewetting can form much more complicated structures and state-of-the-art applications. Dewetting is used to form nanoparticles arrays for sensors, or even semiconductor nanowires [67]. An important application of dewetting has emerged in the field of light matter interaction objects, where nanoislands formed via solid state dewetting, working as resonators and photonic cavities [54].

1.3.3 Physical-Chemical dynamics of Dewetting

Solid state dewetting is a commonly used technique in microelectronics and integrated circuits applications. In particular, Silicon on Insulator (SOI) substrates are substrates with popular use in the research of dewetting films [20]. A number of examples showed that dewetting is on purpose used to determine a substrate with particles and arrays. Solid state dewetting usually arises from the undesired interaction of different surfaces and surface molecules and their attractive forces between them. Dewetting involves a physical-chemical process that it may be considered as a reverse process of spreading a liquid as it involves the withdrawal of fluid elements from a wet surface [70].

The fundamental interaction between the contacting substrates, they follow some rules according to equation 1.2. The wetting elements may be grouped into two distinct groups that include partial and full wetting depending on the difference between the surface tensions and the surface energy per unit area covered (E_{sub}). Arscott [71] states that surface energy considered must include the wet and dry substrate. The spreading parameter of the two stated can be calculated using the eq. (1.3) as follows:

$$s = [Esub]dry - [Esub]wet = \gamma so - (\gamma sl + \gamma) \quad (1.3)$$

The coefficients γ indicate the surface tension of the liquid at the solid air, solid-liquid, and solid air, respectively. The wetting parameter S is positive when the wetting is complete. Fig. 10, is indicated that dewetting can be found also in nature with the raindrops to form a round droplet on top of different surfaces.

Figure 10: Examples of a raindrop on the top of a hydrophobic surface.

Therefore, due to the balance of the capillary forces, the film spreads uniformly on the substrate surface to form a continuous film [71, 72]. When partial wetting happens, the wetting coefficient is negative, and the liquid forms droplets on the surface of the solid. For partial wetting, the wetting angle is greater than zero, as presented in Fig. 11a. Concerning the thin films, dewetting is driven by the atomic motion, from their metastable equilibrium. Usually, the dewetting initiates from some preexisted holes or scratches on the surface, or even from the edges of the sample. Therefore, when the temperature is increased the atoms start to travel and the rate of dewetting is strongly affected by the temperature (Fig. 12). Generally, the process consists of 3 distinguishable phases. First the hole formation, then the hole growth, and finally the ligament breakup.

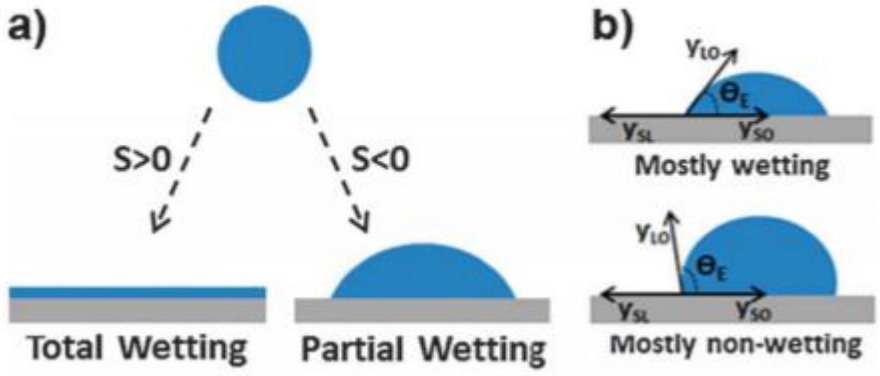

Figure 11: Representation of wetting regimes on a solid surface [74].

The island's formation is driven by the well-known Rayleigh-Plateau instability [67] from solid cylinders, which are unstable by a range of perturbations. An example is the droplet formation from the running water coming from the sink in our kitchen. In Fig. 12 we can see the island's formation from the breakage of the cylindrical shape rim moving towards the black boundaries. A hole is important to be formed, in order for the process to be started. When the hole formation is done, then the thin film starts to retreat to enlarge the hole formation into a bigger one. Then, the fingers-like rims appear and eventually, leave behind a row of islands.

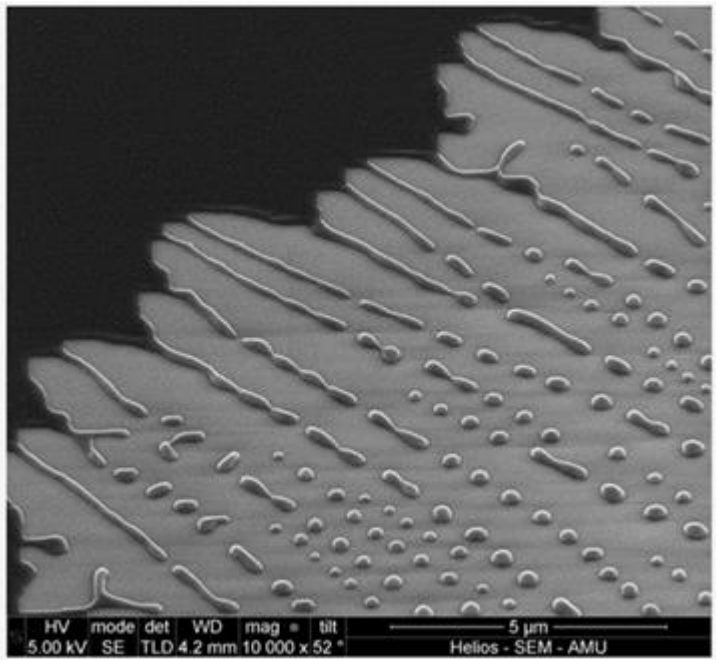

Figure 12: Spontaneous solid state dewetting of a thin film (black area) on a substrate (white area). The arrays of nanoislands appear as droplets on the surface [74].

Finally, after dewetting occurred and it reached its fully dewetting conditions, further annealing led to an effect where atoms from a smaller island de-attached and joined a larger island with higher surface energy, the so-called Ostwald ripening process [74]. The coalescence may continue until an equilibrium molecule size and shape is achieved. The growth of the island often leads to a depletion of the region where the previous island was situated. However, the process may stop as other forces kick in and begin to reshape the particles, their spatial distance, and size.

1.3.5 Dewetting evolution of single crystal thin films

In normal circumstances, dewetting leads to the rapid formation of particles with considerable spatial correlations. However, the particles may not form a desirable pattern over a large area. The precise positions and size of multiple lengths

may be controlled by patterning the thin film prior to annealing and controlling the surface tension of the substrate [75].

Coming back to single crystal thin films, like the Silicon on insulator (SOI), dewetting is a very common technique to perturb the thin film and engineer the surface in a desirable way. However, the original pre-existing hole to initiate the solid state dewetting process seems to be unlikely. Thus, an intentional introduction of a hole or more complex structures on the film surface that react locally to make the film discontinuous and eventually, assist the dewetting process to begin [76]. Fig. 13 presents examples of holes in single-crystal films. Assisted dewetting can be obtained not only by introducing intentionally holes and pins on thin films' surface but also lithographic processes can be used to arrive in more complex scenarios of dewetting according to the desired application. Lithographic and other patterning procedures can modify the substrate surface or pre-patterning the film before dewetting occurs [67]. This can provide arrays and formulated islands to control self-organization in order to obtain desirable patterns formed by solid-state dewetting.

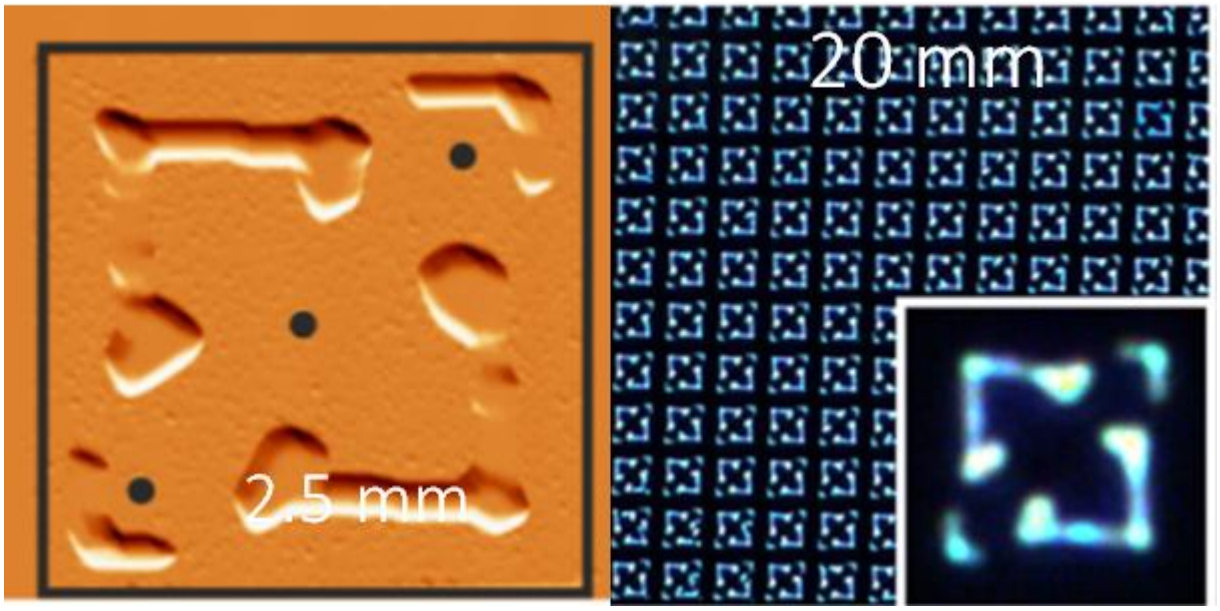

Figure 13: Arrays of dewetted patches by introducing 3 holes along with the patch. The dewetting appears to be identical in all cases [76].

.

More assisted methods introduce techniques such as stamp-assisted dewetting which involves the deposition of material between a stamp and a substrate. The dewetting process is conducted with a constrained position and time to generate the desired shape and size. Quasi-equilibrium conditions can be attained within a short time due to a reduction in the size of the dewetting area. This method can be used to overcome the limitation of thin-film technology by providing a superior surface quality within a short time. The stamp assisted dewetting also enhances the sizes of the nanoparticles through the imposition of the motif on the nanoparticles. Therefore, stamp protrusion can be used to generate versatile patterns.

By changing dewetting parameters, for instance, the substrate temperature during the annealing process, different assemblies can be achieved. Thermal dewetting has been explored also for generating two-component SiGe or pure Si and Ge nanoparticles. In ref. [25], an amorphous thin Ge layer film, after a single thermal annealing step, we can observe step by step the occurring dewetting mechanism leading to single crystal Ge islands on the top of SiO_2/Si (001) substrate. A further potential of joining silicon dewetting with germanium deposition is presented in chapter 3 of this thesis, where it is highlighted how this technique allows a modification of the size distribution and the shape of the dewetted particles.

All in all, solid state dewetting is an easy and efficient technique to fabricate nanoparticles on demand. However, the need to control the size, shape, and position within the entire sample with spontaneous dewetting is impossible to achieve. To overcome this problem there is the need for assisted dewetting methods such as lithography or other laser-assisted methods which in many cases the current thesis implements to reach the desirable architecture for the experimental process.

1.3.7. Nano-islands' faceting shape fabricated from dewetting

A relevant advantage of dewetting over other fabrication methods is the possibility to form faceted objects and thus atomically smooth. In the work of A.A. Shklyaeva et.al. [65], SiGe islands arising during the deposition of Ge on the top of Si (001) in high temperatures. The formation of the islands occurs when the kinetic limitations are reduced and the growth conditions are close to thermodynamically equilibrium. Islands' shapes indicate that the atom diffusion rate becomes large enough to provide the corresponding massive atom transport along the surface. The upper part of the islands is covered with facets, such as {501}, {311}, {23 15 3} and {111}, which are usually observed on the sides of large Ge and Si islands as shown in Fig. 14.

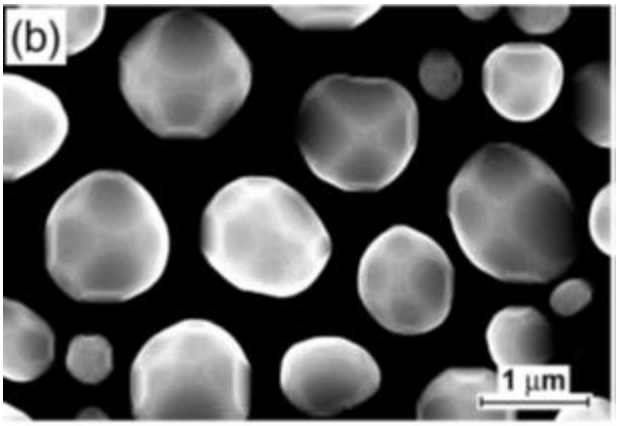

Figure 14: Faceting shape with the minimum energy exposed facets [65].

Faceting during deposition or growth is a much more complex mechanism that relies on material properties and morphological configurations. In ref [77], it is shown that deposition kinetics anisotropy is the root cause of facet propagation in Si, especially for the {311} facets that are very usually observed as shown in Fig. 15.

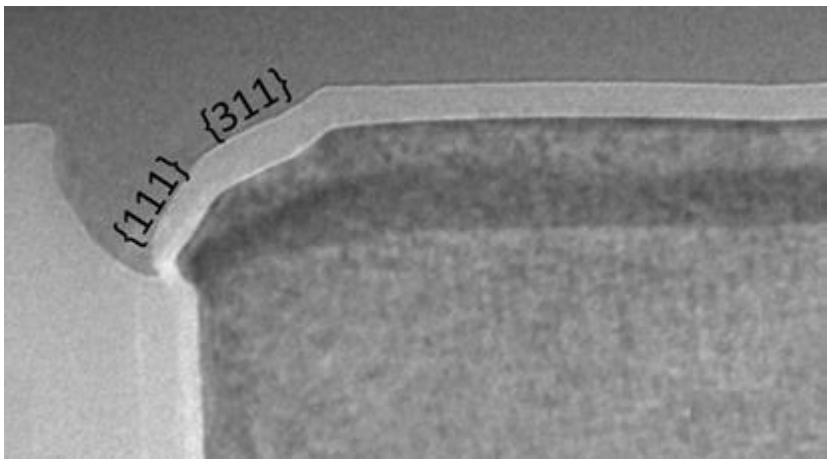

Figure 15: TEM picture of a SiGe faceting shape with the dominant {111} and {311} facets exposed [77].

The authors of ref [13] showed the influence of heteroepitaxial grown on Ge on the thermal dewetting and agglomeration of the Si (0 0 1) template layer in ultrathin silicon-on-insulator (SOI). The dewetted islands are still facetted, but not predominantly bounded by the {3 1 1} facets like the previous reports. Instead, the dominant exposed facet {1 0 5} is observed in certain growing conditions as shown in Fig. 16.

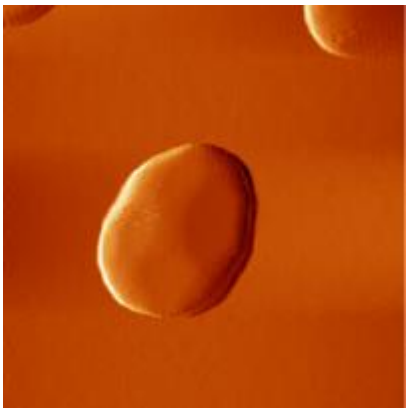

Figure 16: AFM of exposed facets on the Ge nano-island [13].

The influence of solid state dewetting in the faceting shape of Ge islands on the top of Si (001) substrate is studied in [78]. Specifically, in this study, X-ray diffraction technique was used to reveal the main physical parameters (activation energy and kinetic pre-factors) that govern the dewetting dynamics of Ge (001) solid-state thin films on amorphous SiO_2 substrate (Fig. 17). A real-space imaging technique (GISAXS) can give access to the mean shape of the agglomerated 3D island, including facets. The main facets are {113}, {15 3 23}, and {111} facets. Besides, the most intense signal comes from the {113}, meaning that the mean shape of the Ge islands exhibits large {113} facets.

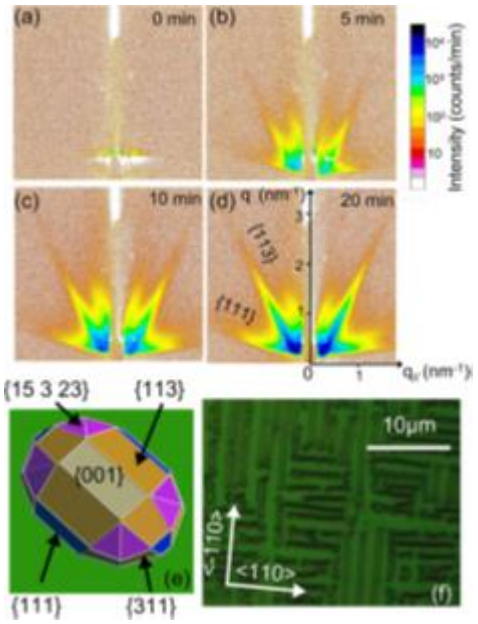

Figure 17: A real-space imaging technique (GISAXS) gives the 3D representation of the island including the faceting shape [79].

The influence of faceting on solid state dewetting mechanisms is studied in [79]. They show the effects of facets on the dewetting properties of an anisotropic material and that {15 3 23} can be “switched off” or can be “switched on” by varying

the temperature. However, at temperatures higher than 800 degrees, {15 3 23} facets disappear, and the {311} facets re-introduce.

Bibliography

1) Arute, F., Arya, K., Babbush, R. et al. 'Quantum supremacy using a programmable superconducting processor'. Nature 574, 505–510 (2019).
2) HAN-SEN ZHONG, HUI WANG et. al. 'Quantum computational advantage using photons', SCIENCE 1460-1463, 2020.
3) G. Brassard, 'Brief history of quantum cryptography: a personal perspective' IEEE Information Theory Workshop on Theory and Practice in Information-Theoretic Security, 2005.
4) XIAO YUAN, 'A quantum-computing advantage for chemistry', SCIENCE, 1054-1055, 2020.
5) Trabesinger, A. Quantum computing: towards reality. Nature 543, S1 (2017).
6) Alvarez-Rodriguez, U., Sanz, M., Lamata, L. et al. Quantum Artificial Life in an IBM Quantum Computer. Sci Rep 8, 14793 (2018).
7) Harrow, A., Montanaro, A. Quantum computational supremacy. Nature 549, 203–209 (2017).
8) Simmons, M. A new horizon for quantum information. npj Quantum Inf 1, 15013 (2015).
9) Zhong, H., Wang, Y. Quantum dots on demand. Nat. Photonics 14, 65–66 (2020).
10) Scappucci, G., Kloeffel, C., Zwanenburg, F.A. et al. The germanium quantum information route. Nat Rev Mater (2020).
11) Piquero-Zulaica, I., Lobo-Checa, J., Sadeghi, A. et al. Precise engineering of quantum dot array coupling through their barrier widths. Nat Commun 8, 787 (2017).
12) Nurmikko, A. What future for quantum dot-based light emitters?. Nature Nanotech 10, 1001–1004 (2015).
13) Kimble, H. The quantum internet. Nature 453, 1023–1030 (2008).

14) Somaschi, N., Giesz, V., De Santis, L. et al. Near-optimal single-photon sources in the solid state. Nature Photon 10, 340–345 (2016).
15) Reimer, M.E., Cher, C. The quest for a perfect single-photon source. Nat. Photonics 13, 734–736 (2019).
16) Paesani, S., Borghi, M., Signorini, S. et al. Near-ideal spontaneous photon sources in silicon quantum photonics. Nat Commun 11, 2505 (2020).
17) Lin, X., Dai, X., Pu, C. et al. Electrically-driven single-photon sources based on colloidal quantum dots with near-optimal antibunching at room temperature. Nat Commun 8, 1132 (2017).
18) Khramtsov, I.A., Vyshnevyy, A.A. & Fedyanin, D.Y. Enhancing the brightness of electrically driven single-photon sources using color centers in silicon carbide. npj Quantum Inf 4, 15 (2018).
19) Grosso, G., Moon, H., Lienhard, B. et al. Tunable and high-purity room temperature single-photon emission from atomic defects in hexagonal boron nitride. Nat Commun 8, 705 (2017).
20) Marco Abbarchi, Meher Naffouti, Benjamin Vial, et al, 'Wafer Scale Formation of Monocrystalline Silicon-Based Mie Resonators via Silicon-on-Insulator Dewetting', ACS Nano, 8, 11, 11181–11190, (2014).
21) Andrey B. Evlyukhin, Carsten Reinhardt, Andreas Seidel, Boris S. Luk'yanchuk, and Boris N. Chichkov, 'Optical response features of Si-nanoparticle arrays', Phys. Rev. B 82, 045404, (2010).
22) Spinelli, P., Verschuuren, M. & Polman, A. Broadband omnidirectional antireflection coating based on subwavelength surface Mie resonators. Nat Commun 3, 692 (2012).
23) Isabelle Staude, Andrey E. Miroshnichenko, Manuel Decker, et al, 'Tailoring Directional Scattering through Magnetic and Electric Resonances in Subwavelength Silicon Nanodisks', ACS Nano, 7, 9, 7824–7832, 2013.
24) Berbezier, I., Aouassa, M., Ronda, A., Favre, L., Bollani, M., Sordan, R., Delobbe, A., & Sudraud, P. 'Ordered arrays of SI and GE nanocrystals via dewetting of pre-patterned thin films', Journal of Applied Physics, 113(6), 064908, (2013).
25) Dimosthenis Toliopoulos, Alexey Fedorov, Sergio Bietti, Monica Bollani, Shiro Tsukamoto, Emiliano Bonera, Marco Abbarchi, Andrea Ballabio, Giovanni Isella, Stefano

Sanguinetti,'Solid-state dewetting of amorphous Ge thin film SiO2/Si (001)', Nanomaterials, 10, 2542, (2020).

26) Bulu, I., Babinec, T., Hausmann, B., Choy, J. T., & Loncar, M, 'Plasmonic resonators for enhanced diamond NV- center single photon sources', Optics Express, 19(6), 5268, (2011).

27) Akopian, N., Wang, L., Rastelli, A., Schmidt, O. G. & Zwiller, V., 'Hybrid semiconductor-atomic interface: Slowing down single photons from a quantum dot', Nat. Photonics 5, 230–233 (2011).

28) Trotta, R. et al. 'Wavelength-tunable sources of entangled photons interfaced with atomic vapours', Nat. Commun. 7, 10375 (2016).

29) Ward, M. B. et al. 'Coherent dynamics of a telecom-wavelength entangled photon source', Nat. Commun. 5, 3316 (2014).

30) Portalupi, S. L., Jetter, M. & Michler, P., 'InAs quantum dots grown on metamorphic buffers as non-classical light sources at telecom C-band: a review', Semicond. Sci. Technol. 34, 053001 (2019).

31) Cirlin, G. E., Reznik, R. R., Shtrom, I. V., Khrebtov, A. I., Samsonenko, Y. B., Kukushkin, S. A., Kasama, T., & Akopian, N, 'Hybrid GaAs/AlGaAs nanowire quantum dot system for single photon sources', Technical Physics, 52(4), 469, (2018).

32) Abdellatif, M., Song, J., Choi, W., Cho, N., & Lee, J., 'Quantum dot-like effect in InGaAs/GaAs quantum well,' The European Physical Journal Applied Physics, 55(2), 20402, (2012).

33) Bergman, K., 'Nanophotonic interconnection networks for performance-energy optimized computing', IEEE International Interconnect Technology Conference (2012).

34) Wakayama, Y., Tagami, T., & Tanaka, S. (1999). Three-dimensional islands of SI and GE formed on SiO2 through crystallization and agglomeration from amorphous thin films. Thin Solid Films, 350(1-2), 300-307.

35) S. Minari, L. Cavigli, F. Sarti, M. Abbarchi, N. Accanto, G. Mu~noz Matutano, S. Bietti, S. Sanguinetti, A. Vinattieri, and M. Gurioli,'Single photon emission from impurity centers in AlGaAs epilayers on Ge and Si substrates', APPLIED PHYSICS LETTERS 101, 172105 (2012).

36) Rosa Brouri, Alexios Beveratos, Jean-Philippe Poizat, and Philippe Grangier, "Photon antibunching in the fluorescence of individual color centers in diamond," Opt. Lett. 25, 1294-1296 (2000)
37) Christian Kurtsiefer, Sonja Mayer, Patrick Zarda, and Harald Weinfurter, 'Stable Solid-State Source of Single Photons', Vol. 85, Iss. 2 , (2000).
38) S. Strauf P. Michler J. Gutowski M. Klude D. Hommel D. Wolverson J.J. Davies, 'Negatively Charged Donor Centers in Ultrathin ZnSe:N Layers', 229, 1, 245-250, (2002).
39) A. Muller, P. Bianucci, C. Piermarocchi, M. Fornari, I. C. Robin, R. Andre, and C. K. Shih, 'Time-resolved photoluminescence spectroscopy of individual Te impurity centers in ZnSe', Phys. Rev. B 73, 081306 (2006).
40) K. Sanaka, A. Pawlis, T. D. Ladd, D. J. Sleiter, K. Lischka, and Y. Yamamoto, 'Entangling Single Photons from Independently Tuned Semiconductor Nanoemitters', Nano Lett. 12, 4611 (2012).
41) M. Ikezawa, Y. Sakuma, L. Zhang, Y. Sone, T. Mori, T. Hamano, M. Watanabe, K. Sakoda, and Y. Masumoto, 'Quantum interference of two photons emitted from a luminescence center in GaAs:N', Appl. Phys. Lett. 100, 042106 (2012).
42) F. Sarti, G. Muñoz Matutano, D. Bauer, N. Dotti, S. Bietti, G. Isella, A. Vinattieri, S. Sanguinetti, and M. Gurioli,'Multiexciton complex from extrinsic centers in AlGaAs epilayers on Ge and Si substrates', Journal of Applied Physics 114, 224314 (2013).
43) Frigeri, P., Seravalli, L., Trevisi, G., & Franchi, S, 'Molecular beam epitaxy: An overview', Reference Module in Materials Science and Materials Engineering, (2016).
44) Raghavan, S., Schumann, T., Kim, H., Zhang, J. Y., Cain, T. A., & Stemmer, S. 'High-mobility BaSnO3 grown by oxide molecular beam epitaxy', Apl Materials, 4(1), 016106, (2016).
45) Paik, H., Chen, Z., Lochocki, E., Seidner H, A., Verma, A., Tanen, N. & Brützam, M. . 'Adsorption-controlled growth of La-doped BaSnO3 by molecular-beam epitaxy', APL Materials, 5(11), 116107, (2017).
46) Shimamune, Y., Jimbo, K., Nishida, G., Murayama, M., Takeuchi, A., & Katagiri, H. 'Cu2ZnSnS4 formation by co-evaporation and subsequent annealing in S-flux using molecular beam epitaxy system', Thin Solid Films, 638, 312-317, (2017).

47) Kako, S. et al. ‘A gallium nitride single-photon source operating at 200 K’, Nat. Mater. 5, 887–892 (2006).
48) Sortino, L., Zotev, P.G., Mignuzzi, S. et al. ‘Enhanced light-matter interaction in an atomically thin semiconductor coupled with dielectric nano-antennas’, Nat Commun 10, 5119 (2019).
49) Engel, M., Steiner, M., Lombardo, A. et al. ‘Light–matter interaction in a microcavity-controlled graphene transistor’, Nat Commun 3, 906 (2012).
50) Siegle, T., Schierle, S., Kraemmer, S. et al. ‘Photonic molecules with a tunable inter-cavity gap’, Light Sci Appl 6, e16224 (2017).
51) De Liberato, S. ‘Light-matter decoupling in the deep strong coupling regime: The breakdown of the Purcell effect’, Physical review letters, 112 (1), 016401, (2014).
52) Reitz, M., Mineo, F., & Genes, C. ‘Energy transfer and correlations in cavity-embedded donor-acceptor configurations’, Scientific reports, 8(1), 1-11, (2018).
53) Bidault, S., Mivelle, M., & Bonod, N. ‘Dielectric nanoantennas to manipulate solid-state light emission’, Journal of Applied Physics, 126(9), 094104, (2019).
54) Meher Naffouti, Thomas David, Abdelmalek Benkouider, Luc Favre, Antoine Ronda, Isabelle Berbezier, Sebastien Bidault, Nicolas Bonod and Marco Abbarchi, ‘Fabrication of poly-crystalline Si-based Mie resonators via amorphous Si on SiO2 dewetting’, Nanoscale, 2016, 8, 2844.
55) Garín, M., Fenollosa, R., Alcubilla, R. et al. ‘All-silicon spherical-Mie-resonator photodiode with spectral response in the infrared region’, Nat Commun 5, 3440 (2014).
56) G. LI, Z. XIANG, F. YU, T. ASABA, B. LAWSON, P. CAI, C. TINSMAN, A. BERKLEY, S. WOLGAST, Y. S. EO, DAE-JEONG KIM, C. KURDAK, J. W. ALLEN, K. SUN, X. H. CHEN, Y. Y. WANG, Z. FISK, LU LI, ‘Two-dimensional Fermi surfaces in Kondo insulator SmB6’, SCIENCE, 1208-1212, (2014).
57) Alexey P. Slobozhanyuk, Alexander N. Poddubny, Andrey E. Miroshnichenko, Pavel A. Belov, and Yuri S. Kivshar, ‘Subwavelength Topological Edge States in Optically Resonant Dielectric Structures’, Phys. Rev. Lett. 114, 123901, (2015).
58) Gu, J., Singh, R. Liu, X. et al. ‘Active control of electromagnetically induced transparency analogue in terahertz metamaterials’, Nat Commun 3, 1151 (2012).
59) MOHAMMADREZA KHORASANINEJAD, WEI TING CHEN, ROBERT C. DEVLIN, JAEWON OH, ALEXANDER Y. ZHU, FEDERICO CAPASSO, ‘Metalenses at visible

wavelengths: Diffraction-limited focusing and subwavelength resolution imaging', SCIENCE, 1190-1194, (2016).

60) Checcucci, S. (2018). 'Mie resonators for photonic applications at optical frequencies', International Doctorate in Atomic and Molecular Photonics.

61) Simona Checcucci, Thomas Bottein, Jean-Benoit Claude, Thomas Wood, Magali Putero, Luc Favre, Massimo Gurioli, Marco Abbarchi, David Grosso, 'Titania-Based Spherical Mie Resonators Elaborated by High-Throughput Aerosol Spray: Single Object Investigation', Adv. Fun. Mat, Volume 28, Issue 31, (2018).

62) Aouassa, M., Berbezier, I., Favre, L., Ronda, A., Bollani, M., Sordan, R., Delobbe, A., & Sudraud, P. 'Design of free patterns of nanocrystals with ad hoc features via templated dewetting', Applied Physics Letters, 101(1), 013117, (2012).

63) Sandoval, L., Reina, C., & Marian, J. 'Formation of Nanotwin networks during high-temperature crystallization of amorphous germanium', Scientific Reports, 5(1), (2015).

64) Takenaka, Y., Sumino, Y., & Ohzono, T. 'Dewetting of a droplet induced by the adsorption of surfactants on a glass substrate', Soft Matter, 10(30), 5597, (2014).

65) A.A. Shklyaeva, A.E. Budazhapova, 'Submicron- and micron-sized SiGe island formation on Si (100) by dewetting', Thin Solid Films 642 (2017) 345–351.

66) Sutter, E., & Sutter, P. 'Assembly of GE nanocrystals on SiO2 via a stress-induced dewetting process', Nanotechnology, 17(15), 3724-3727, (2006).

67) Carl V. Thompson, 'Solid-State Dewetting of Thin Films', Annu. Rev. Mater. Res, 42, 399, (2012).

68) Biscarini, F., Gentili, D., Margapoti, E., & Cavallini, M. (2013). Technological applications of Dewetting. Nanoscale Liquid Interfaces.

69) Pochon, S. P. 'Ion-beam nanopatterning: Experimental results with chemically-assisted beam', Advanced Etch Technology for Nanopatterning, (2018).

70) Souda, R. 'On sub-tg dewetting of nanoconfined liquids and autophobic dewetting of crystallites', Physical Chemistry Chemical Physics, 14(12), 4118, (2012).

71) Arscott, S. 'Dynamic chemically driven Dewetting, spreading, and self-running of sessile droplets on crystalline silicon', Langmuir, 32(48), 12611-12622, (2016).

72) Leroy, F., Cheynis, F., Passanante, T., & Müller, P. (2013). Influence of facets on solid state dewetting mechanisms: Comparison between GE and SI onSiO2. Physical Review B, 88(3).

73) Gentili, D., Foschi, G., Valle, F., Cavallini, M., & Biscarini, F. 'Applications of Dewetting in micro and nanotechnology', Chem. Soc. Rev., 43(35), 12 (2012).
74) David T. Danielson, Daniel K. Sparacin, Jurgen Michel, and Lionel C. Kimerling, 'Surface-energy-driven dewetting theory of silicon-on-insulator agglomeration', Journal of Applied Physics, 100, 083507, (2006).
75) Chame, A., & Pierre-Louis, O. 'Modeling dewetting of ultra-thin solid films', Comptes Rendus Physique, 14(7), 553-563, (2013).
76) Meher Naffouti, Rainer Backofen, Marco Salvalaglio, Thomas Bottein, Mario Lodari, Axel Voigt, Thomas David, Abdelmalek Benkouider, Ibtissem Fraj, Luc Favre, Antoine Ronda, Isabelle Berbezier, David Grosso, Marco Abbarchi, Monica Bollani, 'Complex dewetting scenarios of ultrathin silicon films for large-scale nanoarchitectures', Sci. Adv. 3, 1472 (2017).
77) D. Dutartre, A. Talbot and N. Loubet, 'Facet Propagation in Si and SiGe Epitaxy or Etching', ECS Transactions, 3 (7) 473-487 (2006).
78) F. Cheynis, F. Leroy, T. Passanante, and P. Muller,'Agglomeration dynamics of germanium islands on a silicon oxide substrate: A grazing incidence small-angle x-ray scattering study', APPLIED PHYSICS LETTERS 102, 161603, (2013).
79) F. Leroy, F. Cheynis, T. Passanante, and P. Muller, 'Influence of facets on solid state dewetting mechanisms: Comparison between Ge and Si on SiO2', PHYSICAL REVIEW B 88, 035306, (2013).

Chapter 2: Experimental methods

In the present chapter, we are going to discuss all different experimental methods we use throughout the current Ph.D. thesis, to achieve the goal of fabrication of single photon sources coupled with Mie resonances via solid state dewetting. A presentation of each experimental instrumentation along with their use on each experimental step is located in this chapter.

2.1 MBE GEN II

The semiconductor growth performed for the experiments of this thesis was carried out in an EPI Veeco Gen II MBE machine installed in LNESS laboratory in Como. The scheme of the MBE machine is presented in Figure 1.

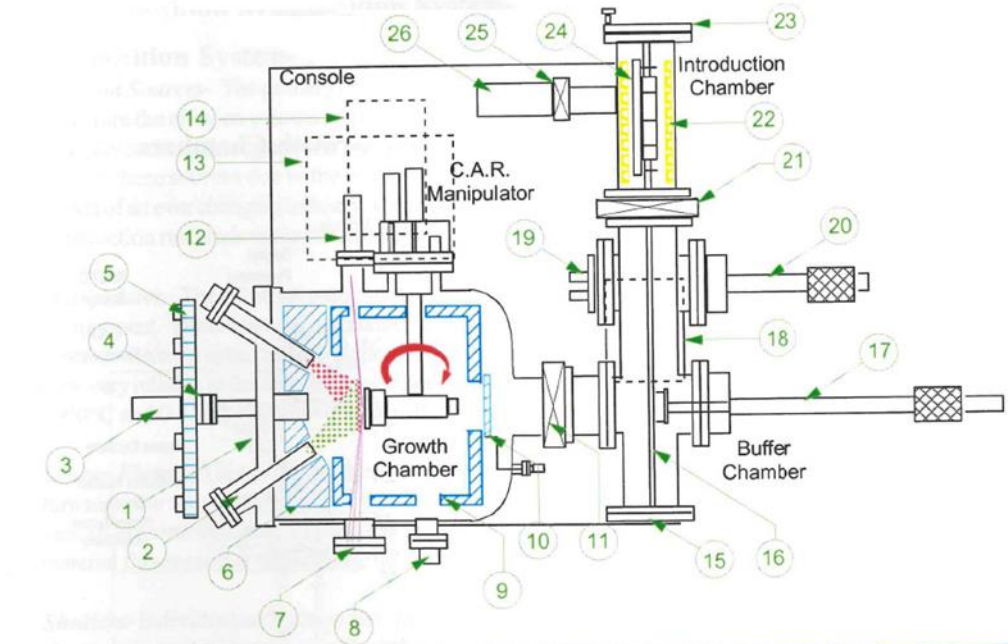

ITEM #	DESCRIPTION	ITEM #	DESCRIPTION	ITEM #	DESCRIPTION	ITEM #	DESCRIPTION	ITEM #	DESCRIPTION
1	Source Flange	6	Source Cryo-panel	11	Growth/Buff Gate Valve	16	Trolley Rail	21	Intro/Buffer Gate Valve
2	Effusion Furnaces	7	RHEED Screen	12	RHEED Source	17	CAR Transfer Arm	22	Outgas Lamps
3	Pyrometer	8	Quad Mass Analyzer	13	Ion Pump (sump)	18	Buffer Ion Pump	23	Quick-hatch Door
4	Heated Pyrometer Viewport	9	Growth Cryo-panel	14	Cryo-pump (sump)	19	Heated Station (HS)	24	Multiple-sample Trolley
5	Removable Shutter Solenoids	10	Master Shutter	15	Buffer End Viewport	20	HS Transfer Arm	25	Intro Pump Gate Valve
								26	Intro Pump (Turbo/Cryo)

Figure 1: Functional block diagram of the Gen II MBE system [photo: Veeco Gen II manual].

The equipment is composed of operating the experimental process in three different chambers separated between them by gate valves. The first chamber is an introduction chamber where it is possible to open inside a connected class 100 flow-box. Inside the flow-box, the substrates can be mounted on special blocks made by molybdenum and loaded on a trolley by using pins attachers, and a driver to set the holder inside them. The trolley has 4 holding positions and therefore, 4 holders with 4 separate substrates can be mounted. Inside the flow-box, there is a heater capable of reaching 400°C, which allows support pieces of the substrate on molybdenum blocks using melted indium spread in a wide area of the molyblock. The sample can stay on the holder due to capillary forces and therefore it doesn't fall out of the holder. This is achieved by moving around the sample by making a simple and weak push from the edge of the sample using a thin teaser. After that, the rest of the indium is collected in order to not leave behind any traces which can affect the experimental process. A different molybdenum block model allows mounting directly a 3" wafer without using indium. Such an approach with an in-house made holder was made to hold the substrates in higher annealing temperatures. Pins were holding the substrates in the corners, leaving unattached most of the surface area of the sample. From the introduction chamber, it is also possible to collect the samples after the growth. When the trolley is mounted back to the trolley base it is necessary to regain the vacuum conditions in this chamber. The vacuum is provided by a rotary pump to establish a primary vacuum and a Leybold Turbovac 361 turbomolecular pump to reach ultra-high vacuum, which allows it to reach 10^{-9} torr. The pressure inside the chamber is monitored by a Pirani gauge and a cold cathode gauge measurement system. To prevent any contamination from the inserted molybdenum blocks to the other chambers or even from the wall of the chamber which has been exposed to the atmosphere every time the vacuum is broken, a baking system capable of reaching

200 °C is available to be used after every opening. The substrate with its holder can be mounted on the top of this heater and remain for a couple of hours. Passing to the second chamber which is a buffer chamber where substrates are maintained ready to be introduced to the main chamber for the growth. This chamber is also in an ultra-high vacuum environment. By using a long arm the holders can be transferred inside the main chamber and mounted in the holder position. The substrate is heated up to 600 °C as a degassing stage which is available to heat a single substrate for annealing experiments or even to desorb impurities without introducing contamination in the main chamber. In this chamber, the vacuum is provided by a Varian Triode Vac Ion ion pump that allows it to reach 10^{-10} torr. The pressure inside the chamber is monitored with a UHV nude Bayard-Alpert gauge connected to a Granville-Phillips 350 measurement system. A mass spectrometer can monitor the composition of the atmosphere of this chamber. An overview of the MBE system is shown in Fig. 2. Three different pumps obtain the vacuum in the main chamber. A cold head connected with a water supply cooled can reach 10 K and works as a cryogenic pump. A second system is composed of a titanium sublimation and Varian Triode VacIon ion pumps. Combining these pumps allows it to reach a 10^{-10} torr pressure level inside the main chamber. To monitor the pressure level inside the main chamber two different UHV nude Bayard-Alpert gauges are used and they are connected to a Granville-Phillips 350 measurement system. The first is capable of monitoring the background pressure, while the second can be rotated in the growth position to measure the equivalent pressure of the atomic or molecular beam coming from the effusion cells. It is possible to mount up to eight effusion cells at this MBE system which can be arranged radially in front of the substrate holder. The effusion cells are connected to Eurotherm 900 EPC controllers for each one cell. Each controller is able to monitor the temperature of each crucible with the use of a thermocouple. The

As cell is a valved cracker cell which allows to finely tune the As flux with a needle valve. To stop or open suddenly the flux, the effusion cells have a pneumatic shutter. Substrate temperature can be monitored by a thermocouple also connected with a Eurotherm 900 EPC controller. Rotation and the rotation speed is used to improve the homogeneity of the deposited sample. Inside the main chamber are present three cryo-shrouds that can be filled with liquid nitrogen to improve the vacuum and reduce the contamination of the growth films. The main chamber is also provided with a position for a Staib reflection high energy electron diffraction (RHEED) composed of an electron gun with a maximal voltage of 15 keV and a RHEED fluorescent screen with a CCD camera to acquire the RHEED pattern changes in real-time during the growth.

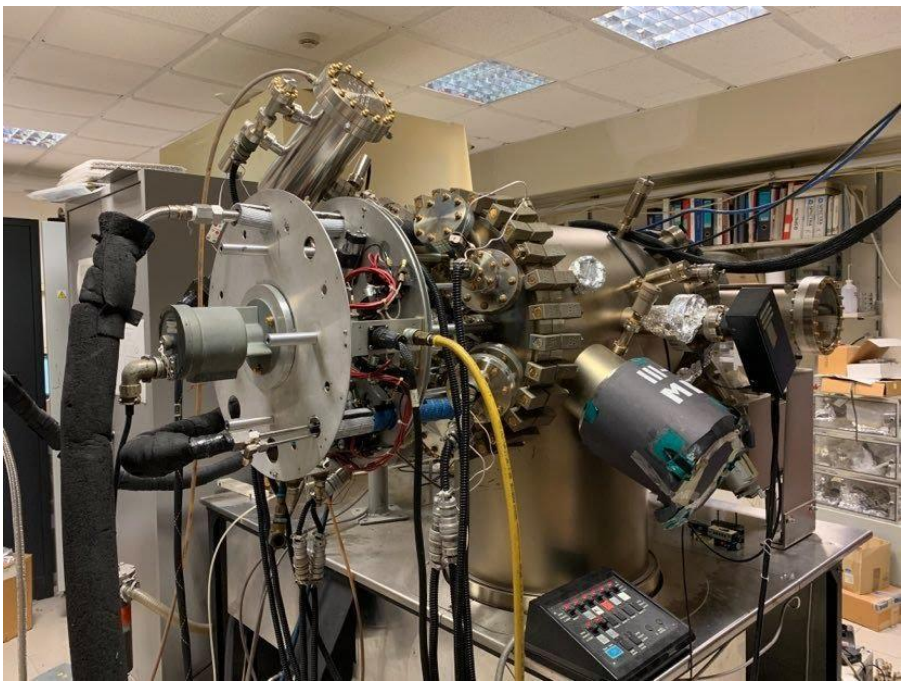

Figure 2: MBE system in LNESS Como Laboratory.

2.2 RHEED

Reflection high energy electron diffraction (RHEED) is a technique through which important information is gathered about the crystallinity and surface morphology of the sample, inside the main chamber during the deposition and allows observing the growth process in situ. An electron gun produces a collimated electron beam (typically between 4-50 keV) which shoots the specimen at a very small angle in respect to the sample surface (few degrees). From the RHEED information collected, the average scattering over a macroscopic area is calculated, based on the dimension of the beam on the sample. The incident electrons are diffracted by the atoms on the surface of the specimen and interfere constructively at certain angles leading to the formation of regular patterns in fluorescence imaging.

One of the most important features of RHEED is the monitoring of layer-by-layer growth during deposition. A notable phenomenon recorded in the literature is the observation of oscillations in the intensity of the RHEED pattern, during the growth of GaAs film into the molecular beam epitaxy chamber. These oscillations in the intensity appeared immediately after the onset of GaAs deposition over a wide range of substrate temperatures (500−720 ºC), growth rates (Ga flux from 1×10^{13} to 1.5×10^{15} atoms cm^{-2} s^{-1}) both for doped and undoped material and irrespectively of the surface reconstruction. The aforementioned oscillations are displayed in Figure 3. It turned out that the period of the oscillation correlated exactly to the monolayer growth rate on a (001) oriented substrate, where a monolayer is determined by one complete Ga layer along with one complete As layer.

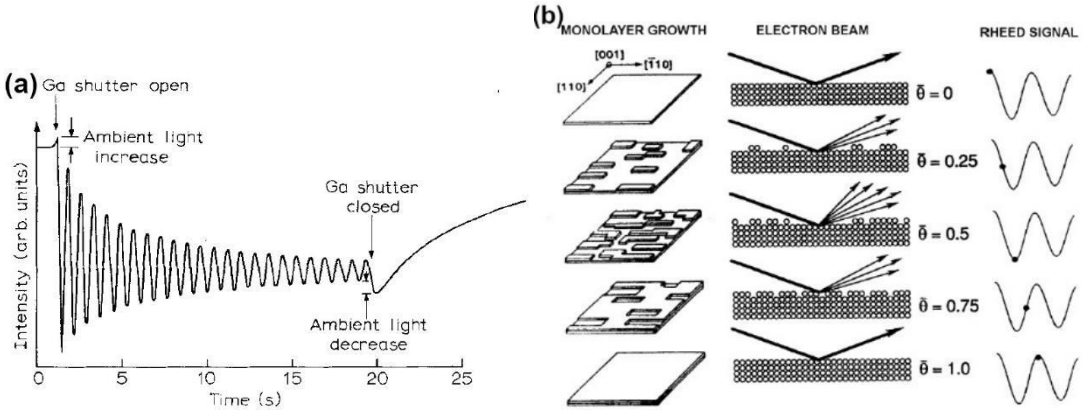

Figure 3: (a) Intensity oscillations of the specular beam in the RHEED pattern from a GaAs (001) – 2×4 reconstructed surface. The period exactly corresponds to the growth rate of a single Ga+As layer and the amplitude gradually decreases. The marked inflections at the beginning and end of growth result from the ambient light change as the shutters are opened and closed. (b) The representation of the formation of a single complete layer and its correspondence with RHEED intensity signal.

Although the amplitude of the oscillations is damped, it was possible to distinguish at least ten complete periods. It was therefore obvious that the observed oscillations provided an accurate picture of the growth rate. In an attempt to explain the observed behavior, there is initially the assumption of the formation of random clusters during growth and then the surface is described as fairly smooth. As growth begins, most adatoms are absorbed before being incorporated into growing clusters, but as stable clusters form nuclei and spread, the growth rate increases to a maximum close to a fraction of a complete layer. Then, when the nucleation of the next layer began, the growth rate reduced. As this sequence was repeated, and as the growth was distributed in several layers, it gradually faded and therefore the complete surface, which was formed over multiple levels, became rough. It is finally concluded that the changes observed in the spectral beam intensity in the RHEED pattern are directly related to the changes in surface roughness.

Observation of the RHEED pattern during growth allows the monitoring of the conditions and the reconstruction of the surface, the control of possible defects in the lattice and the presence of three-dimensional surface development. The appearance of Debye rings is attributed to the presence of poly-crystalline islands on the surface as depicted in Figure 4.

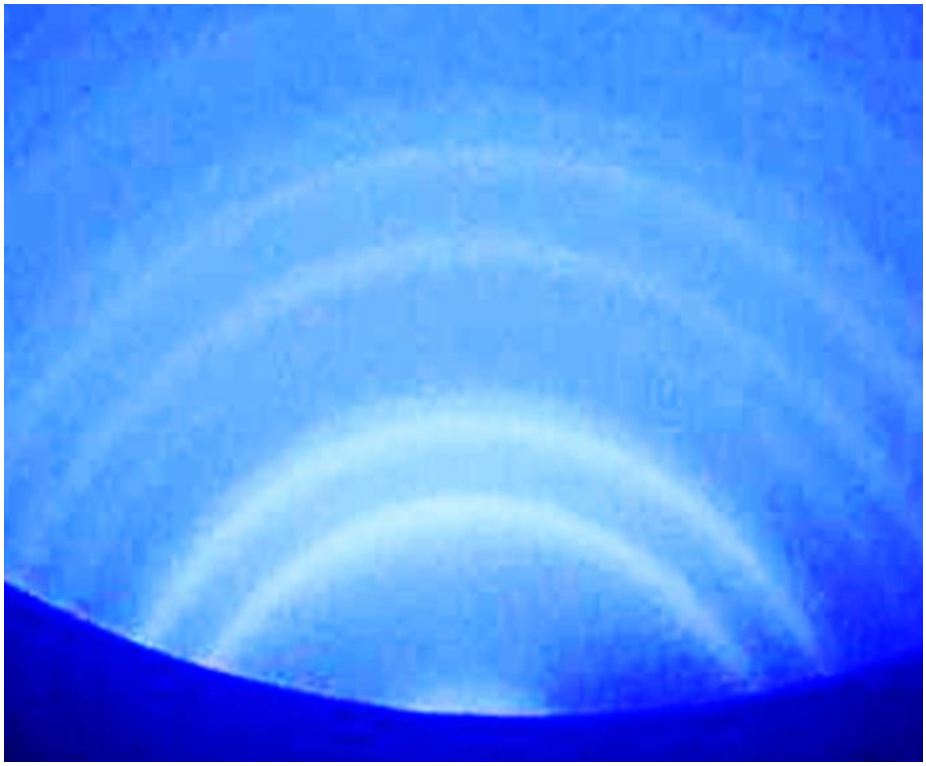

Figure 4: Debye rings indicating the presence of poly-crystalline islands.

2.3 LEPECVD

A modified version of Plasma Enhanced Chemical Vapor Deposition (PECVD) has been used for the deposition of a-Ge thin films. The characteristics of plasma in PECVD allow the growth of epitaxial layers at variance compared to standard PECVD, which is commonly used for the deposition of amorphous/polycrystalline layers [citation]. This modified version is known as Low-Energy Plasma Enhanced Chemical Vapor Deposition (LEPECVD). The LEPECVD reactor employs aspects from both standard and plasma-enhanced CVD. The plasma of standard PECVD is characterized by high energy, while there is additionally high pressure of the precursor gases, in the range of a few mbar. Thus, due to the collision between the ions and the surface of the sample attributed to the high energy plasma, which subsequently leads to damages at the surface of the substrate, epitaxial layers cannot be formed, constituting epitaxially inefficient. Nanocrystals are also a part of the standard PECVD plasma as they are formed by a low mean free path, and subsequently, reach the surface and form a polycrystalline layer. The different characteristics of LEPECVD along with its operative pressure allow it to have just activated species (mainly radicals), absorbed on the surface. The surface remains unaltered since the ions have not enough energy (only a few eV) to produce any damage on it.

2.4 Atomic Force Microscopy (AFM)

Figure 5: Atomic Force Microscope in LNESS Laboratory in Como. Objective lens mounted on a stationary arm on the top of the sample position. The sample holder below can be seen.

For the morphological characterization of some samples, Atomic Force Microscopy (AFM) was used. The AFM used for the measurements was a Veeco Innova installed in the L-NESS laboratory in Como (see Fig. 5). The images were obtained by tapping mode characterization. We monitor the oscillation amplitude and phase from a cantilever probe.

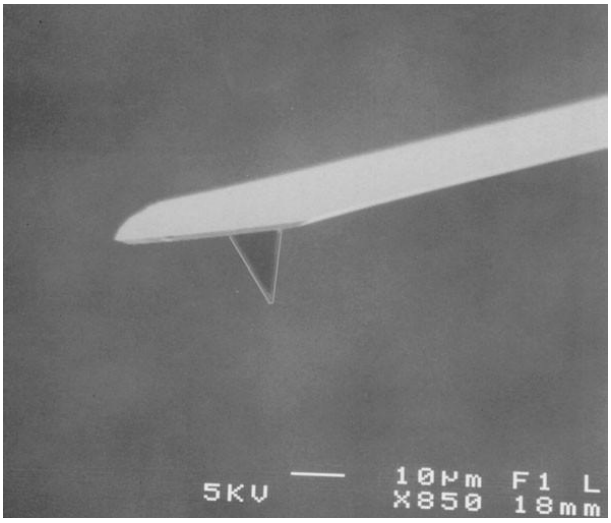

Figure 6: The image of a silicon cantilever AFM probe.

The distance between the examined sample and the probe was set for the tip to perform oscillations tapping softly on the sample's surface (see Fig. 6). The interaction between the probe and the surface provides a feedback signal about its amplitude and phase. Foremost, the friction produced between the probe and the surface is reduced using the tapping mode, which is its biggest advantage. On the other hand, in the contact mode, the cantilever keeps constant contact with the surface, which is the biggest difference in this tapping mode. A laser beam is directed and is reflected from a micro-cantilever, onto a mirror, and later in a photodiode. An AC voltage signal is produced by the oscillating laser spot across the diode as also the cantilever oscillates. The produced signal from the diode is then refined and rectified into a DC voltage. The root mean square (RMS) amplitude is then measured which is proportional to the amount of cantilever oscillation. The setpoint voltage is compared with the feedback system and the two voltages are kept equal to control the amplitude of the cantilever. The RMS voltage is reduced to the setpoint voltage by the feedback loop moving the sample nearer to the tip. The sample reduces the cantilever movement until the desired RMS voltage is reached (see Fig. 7).

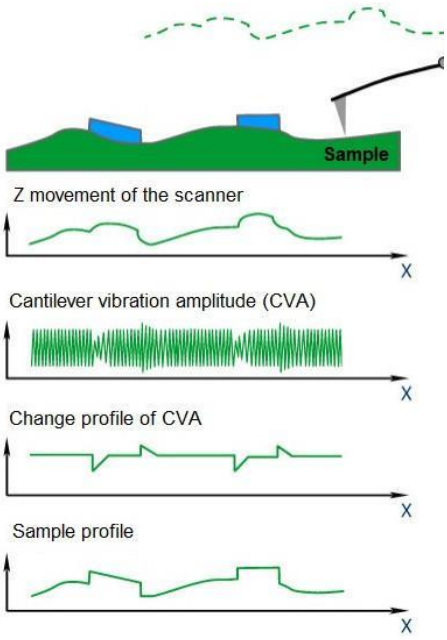

Figure 7: Schematic representation of the use of the cantilever vibrational amplitude (CVA) changes for the feedback in tapping mode AFM.

The piezoelectric movement in the Z direction is translated by the oscillation amplitude of the cantilever, while is in parallel moving the X and Y-axis. The tapping mode requires that the setpoint voltage should be smaller than the RMS voltage when the sample and the probe are far enough. To engage the tip on the surface, the cantilever is getting close until the RMS amplitude is at the setpoint. Usually, the tip of the cantilever is 10 nm but can be reduced to 2 nm for high-resolution imaging. The AFM images acquired in this work of thesis were corrected within the program Gwyddion. Figure 8 shows the cantilever amplitude and topology AFM images of the Ge islands on top of Si/SiO_2 substrates.

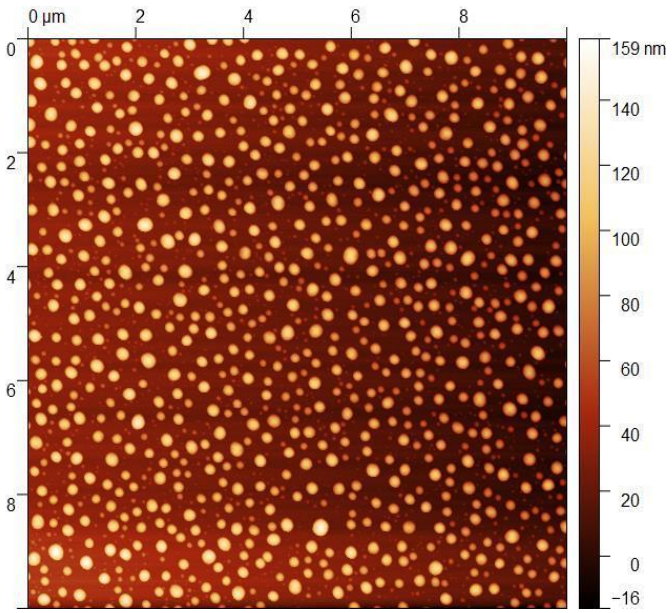

Figure 8: Cantilever amplitude AFM image of Ge islands randomly dispersed onto the SiO_2 substrate.

2.5 Scanning Electron Microscopy (SEM)

The SEM utilized for the surface morphology measurements is an FEI XL 30 FEG introduced in LNESS research facility in Como as appeared in Fig. 9. Four fundamental segments joined to deliver the pictures from the sample surface: an electron gun, a demagnification unit, an output unit, and a recognition unit. The electron gun, which is the electron source producer, provides electrons inside a little spatial volume with a small angular spread and selectable energy. The beam enters the demagnification unit, consisting of a few electron lenses. Electrons hitting the sample interact with the atoms of the sample surface and produce three sorts of signals: X-rays, electrons, and photons. The main detector gets the electrons, enhances them, and converts them into electrical voltage. The output generator signal moves the beam in a raster way over the sample area. In parallel, the final picture is, in the same way, a scan of the surface. The images were acquired in planar view to

estimate the density and the base size of the nanostructures and with a small tilting angle (typically < 10°) to evaluate the shape and the height of the nanostructures. The resolution of the instrument is 10 nm.

Figure 9: Scanning Electron Microscope in LNESS Lab in Como.

2.6 Micro-Photoluminescence (μ-PL)

Photoluminescence (PL) is a phenomenon in which when a substance is irradiated by a light source, that emits de-excitement photons. The analysis of the emitted radiation spectrum provides information about the optical properties of the investigated sample and gives an understanding of its electronic structure. In pursuance of attaining the spatial resolution required to study a nano-sized system, an objective lens is utilized, which aims to focus the excitation beam over a micron-sized area and collect the PL emission. The signal is then separated into its spectral components using a spectrometer and further analyzed. This method is known as micro-PL spectroscopy. In this work, an analog setup has been employed to perform PL measurements that have been both time-resolved and time-integrated, to measure formed QD's or any single photon source, by III-V semiconductors as shown below. A schematic representation of the experimental setup is given in Figure 10.

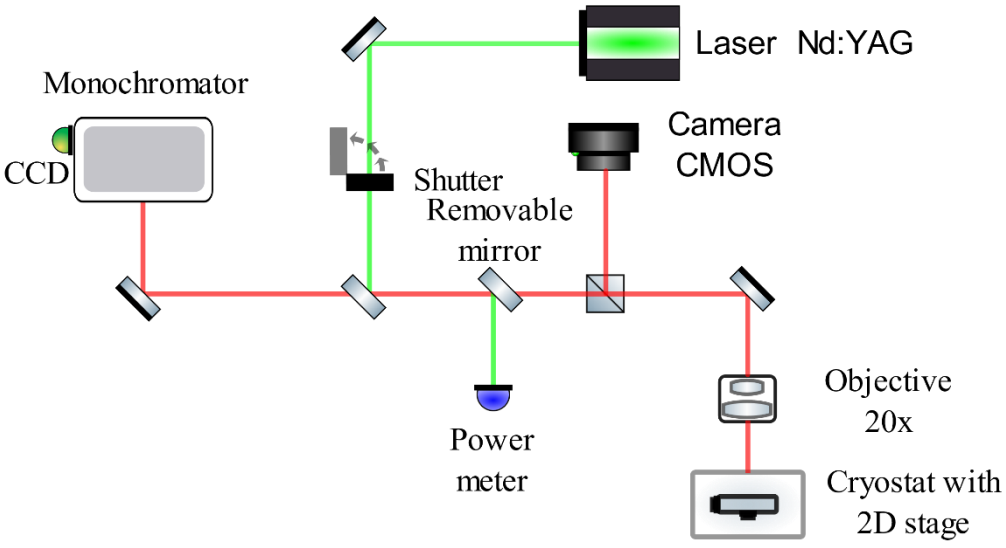

Figure 10: Schematic representation of the experimental set up of the micro Photoluminescence.

To excite a sample, the energy of the incident photons is selected greater than the barriers of the light source. The absorbed photons then create electron-hole pairs

that fill the extended states of the barrier material and interact with the phonons leading to instantaneous relaxation, within a few picoseconds, at the edge of the band where they recombine radiatively or are captured by a light source like QD. When carriers take over the excited levels of a quantum dot, they tend to relax at a slower rate, generally a few dozen picoseconds. This effect is known as phonon bottleneck and has been explained as the lack of available phonon for carrier relaxation, only after this relaxation they can recombine modes through which carriers can couple to radiatively recombine. Indeed, a confined exciton can couple to longitudinal-acoustic phonons (LA) with energies of few meV, while longitudinal-optical phonons (LO) have a nearly monochromatic dispersion relation (35meV for bulk GaAs) giving a very small energy range for the relaxation process.

In this experimental work, two laser sources were employed. The first is a mode-locked Spectra Physics Tsunami Ti: sapphire laser (tunable within 700-1000 nm) optically pumped at 532 nm by a Spectra Physics Millenia Nd: YAG laser, duplicated in frequency by a BBO crystal. This laser source emits pulses with a duration of 200 fs and a repetition rate of 82MHz, and it is employed both for time-integrated and time-resolved PL experiments. For additional research on time-integrated PL measurements, a CW laser source with emission wavelength at 532 nm is also used. It is composed of a Nd: YAG Coherent Antares 76-s, emitting pulses at 1064 nm with a duration of 130 ps and a repetition rate of 76MHz. In order to double the frequency of the pulses, a TBL nonlinear crystal is used, producing a power output of 3 Watt at 532 nm.

The experiments were conducted at very low temperature (10 K) to avoid both the non-radiative recombination of the carriers, which leads to quenching of the PL, and line broadening mechanisms due to phonon interactions. The samples have been placed in a cryostat, which is a cold finger continuum flux type and temperature

stabilized utilizing a heater. The advantage of the cryostat is that liquid helium can circulate without the need for a pump, thus avoiding any unwanted vibrations. Inside the cryostat, takes place a sequence of a turbomolecular and a rotative pump which (are) responsible for creating a vacuum (10^{-6} mbar). The cryostat is placed on an XY translation (stage) composed of two M-405CG Linear positioning Stages motors and two controllers C-863.11 Mercury of Princeton Instruments that achieves precise position control (with a resolution of 100nm). The real micro-PL setup in which the low temperature measurements were performed, is portrayed in Figure 11. The laser beam is focused through the objective lens (100x Mitutoyo) on a small sized area (1 μm diameter), which is also responsible for receiving the PL signal. The microscope is composed of the objective lens, a dichroic, and a removable mirror and a camera (Webcam Celestron NexImage) joined to a photographic objective (lens) (f = 200 mm).

The magnified image of the sample is obtained from the camera, by inserting the removable mirror. In order to position the excitation laser spot on the light source with maximum accuracy, a translation (stage) is employed to control the movements orthogonal to the beam. Besides, a piezoelectric translator (resolution 100 nm) provides control over the vertical position of the objective, allowing a detailed focus adjustment. The excitation beam and the PL signal share a portion of the optical path until the dichroic mirror, returning the PL signal which is directed to the spectrometer and filters the sections with high frequencies belonging to the excitation source. The PL signal is focused through a lens (f = 15mm) on the entrance slit of an Acton Spectra Pro 2300i monochromator in Czerny-Turner configuration, with a focal length of 300 mm, and three (selectable) gratings. For the measurements, a 750nm -blazed 1200 g/mm and a 1μm-blazed 600 g/mm grating has been selected. Moreover, the charge coupled device (CCD) PIXIS 100 of Princeton Instruments is

placed in the flat-field exit of the monochromator, which is cooled at -70 ºC with a double stage Peltier module and has a matrix of 1340 x 100 pixels with the dimensions of 20 μm x 20 μm, that responds to optical signals in the bandwidth of 400-1050 nm. The monochromator setting is driven by Mono Control software and the CCD spectra acquisition by the Winspec software. The monochromator also has a second exit slit which is used for time-resolved PL measurements and is described further in the next section. The spatial resolution of the micro-PL setup is ~1 μm and the spectral resolution around 500 μeV (using the 600 g/mm grating).

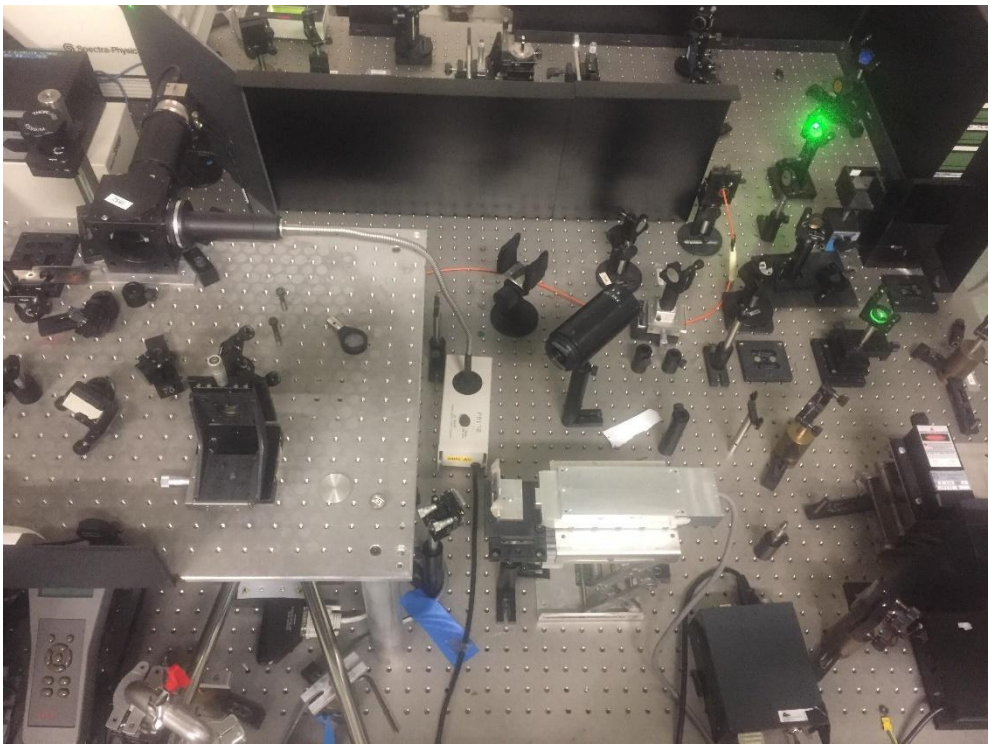

Figure 11: Micro-Photoluminescence set up in LENS laboratory in the University of Florence.

2.7 Time-resolved Photoluminescence (PL)

The time-resolved measurements performed in the same equipment the micro-PL characterization was done. The measurements were executed on the III-V semiconductors on Ge nano-islands onto SiO_2 substrates in order to study the carrier recombination dynamics. The most common approach is to implement a Time-Correlated Single Photon Counting (TCSPC) experiment and excite the sample with a pulsed laser with high repletion rate between 10 to 100 MHz. For each experiment was measured the time delay of the photons emitted towards the detector. By building a histogram of the events versus the time delay we can extract the decay curve for each single photon emitter. Furthermore, from the plot, we can calculate the lifetime of a confined emitted photon. In the following schematic, Fig. 12 indicated the differences in the set-up compared to the PL-set up.

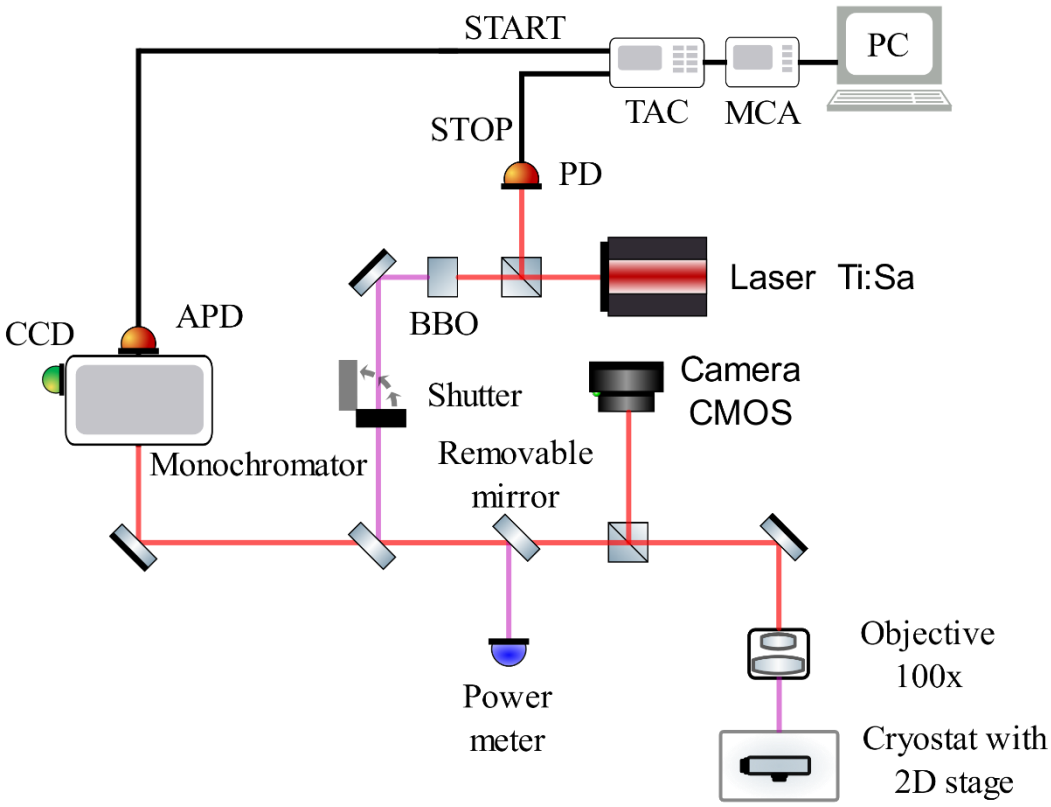

Figure 12: Time resolved measurements were done using the experimental configurations as shown in the figure above.

2.8 Dark Field Spectroscopy

The Dark field measurements were performed on each individual nano-island in order to extract their scattering profile. A microscope (ZEISS Axio Observer) with a 100-x magnification objective lens (numerical aperture NA = 0.9) was used in Dark field mode to collect the scattering light. Then an optical fiber (Ocean Optics multimode fiber, VIS-NIR, core diameter 200 mm) was used to collect the light and drive it to the spectrometer. The microscope is connected with a spectrometer and Si-based CCD linear array (Flame-T-VIS-NIR by Ocean Optics). A schematic representation of the DF set up is given in the following Figure 13.

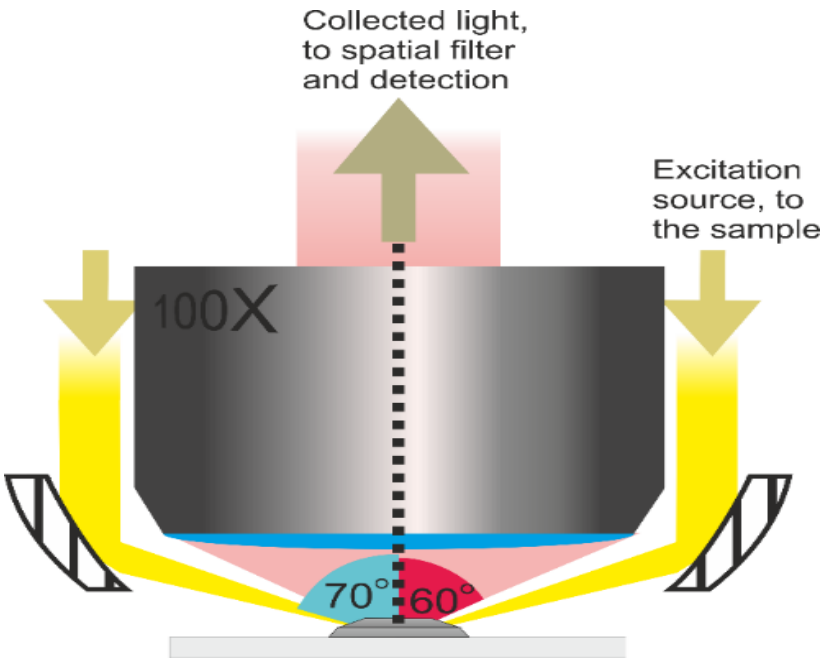

Figure 13: Dark Field Spectroscopy on the individual Dielectric Mie Resonators.

Chapter 3: Solid-state dewetting dynamics of amorphous Ge

In this chapter, the results of a detailed analysis of the solid state dewetting process of a-Ge thin films on a SiO_2/Si (001) substrate is presented. It is discussed the main results obtained in LNESS Laboratories in Como as part of the experimental training for the current thesis. The results were published and can be found in ref. [1]. The goal of this step is to create a suitable nano-antenna seed for the epitaxial regrow of III-V semiconductors, via solid state dewetting and the study of its dynamics. Therefore, the final goal of this chapter is about controlling the dewetting process in order to obtain islands with controlled size. Surface energy minimization, which drives the dewetting in crystalline layers in the major player on surface dynamics, along with Ge crystal nucleation and Ge diffusion on the a-Ge surface for the transformation of the amorphous thin films into crystalline nano-islands. Thin films in their two dimensional state are considered as unstable continuous films and therefore they could break into a more stable state such as nano-islands whenever a heat treatment occurs to them [2-4]. This process is kinetically controlled by surface diffusion [5], forming nanoparticles from a metastable state of equilibrium thin film. This process is a spontaneous phenomenon occurring and depends on the time and the temperature of the annealing. It is an easy and full wafer process and can organize nanoparticles according to the needs in nanoscale [6]. More details about the solid state dewetting process are presented in the introduction chapter 1 of this thesis report.

Solid state dewetting of the Si or Ge thin films is considered a scalable fabrication process and it can lead to complex and/or desirable configuration structures by tuning the size, size distribution, and surface distribution [7,8,9]. In this set of experiments, the main mechanism which drives this metamorphosis is surface energy minimization along with surface diffusion [10,11]. Si [12] and Ge [13] thin films deposited on an insulator have been reported from the research community to be exploited for light manipulation in visible and near infrared. The formed islands from the heat treatment of these class of thin films are called Mie-resonators and they are capable of light management. Such islands confine light and are considered to be the counterpart of the metallic particles with plasmonic effect for light matter interaction and the enhancement of light manipulation, as previously reported in chapter 1.

However, the use of crystalline Si and crystalline Ge on insulators for the fabrication of islands via solid state dewetting has several disadvantages, due to the constraint of the system on simple geometries. The preparation of such kinds of crystalline thin films is very difficult and costly. However, there is the possibility to obtain the same class of crystalline nano-islands as Mie-resonators for light manipulation by dewetting thin a-Ge films. The process allows for obtaining the desired particle size and size distribution from group IV semiconductor films deposited on top of SiO_2 in order to be implemented in applications in photonic technology with complicated geometries and patterned substrates such as obtaining a single photon emitter or entangled photon emitter. However, dewetting of this kind of thin film is not yet fully addressed and the results can be interesting for the scientific community since single photon emitters can be used for quantum computing and similar applications. Hereby, some of the observations are presented

and discussed to promote this class of crystalline islands from amorphous Ge thin films.

The substrates used for our experiments are three thin layers of Ge (5, 10, and 15 nm). All samples' thin films were deposited by low-energy plasma-enhanced chemical vapor deposition (LEPECVD) described in chapter 2, at 100 °C with a growth rate of 0.25 nm/s. Amorphous Ge thin film was grown on the top of 1 μm of SiO_2, obtained by thermal oxidation of a Si (001) substrate [14]. The wafers were cut into several pieces and were kept in the nitrogen flow fume hood inside a clean room. The size of the samples was about 1 cm^2 size. Once it was needed to mount a sample on a molyblock holder, the samples were washed with acetone and isopropanol for 5 min each and then introduced into the ultra-high vacuum (~10^{-9} torr) of a Molecular Beam Epitaxy chamber (MBE). Later the sample was baked for 8 hours at 200 °C inside the intro chamber to remove humidity and other components coming from the environment. The exact process is described in chapter 2 in detail. Eleven samples were annealed at increasing temperature, in the range T= 550 °C - 810 °C, for 2 hours in an ultra-high vacuum system. However, for the needs of the present thesis, we are going to present only a series of experiments from the wafer of 15 nm original thin film (see Table I) and therefore only 6 samples.

Sample	Temp. (ºC)	Average diameter (nm)	Density (10^8 island/cm^2)
S1	550	No dewetting	No dewetting
S2	580	115 ± 30	8 ± 1

S3	620	73 ± 23	25 ± 3
S4	680	55 ± 10	40 ± 2
S5	750	110 ±56	11 ± 1
S6	780	120 ± 102	9 ± 1

Table 1: Conditions and characteristics used for the solid-state dewetting experiments.

The samples were transferred inside the MBE system with the process explained in the experimental methods chapter. To start the experiment it needs the background pressure inside the MBE machine to be about 5×10^{-9} torr. The dewetting experiment during the annealing was monitored *in-situ* by Reflection High Energy Electron Diffraction technique (RHEED). This technique was explained in detail in the experimental methods chapter 2. When the dewetting process initiates, a blur appearance of rings (see Fig. 4), which are coming from the surface crystallization from the amorphous thin film. That gives the signal that dewetting and crystallization has already started. Later, when the experiment was finished the morphological characterization of the samples was tested *ex-situ* with a Scanning Electron Microscope (SEM) imaging and with an Atomic Force Microscopy tool. The crystallinity of the islands was confirmed by using a micro-Raman setup spectrometer using a λ= 532 nm laser as an excitation source. The used power of the laser illuminating the sample was less than W= 1 mW. The stage where the sample was mounted had a 0.1 μm lateral resolution movement. An objective lens of 100X

(0.90 numerical aperture) was used for the excitation and the collection in backscattering configuration.

3.1 Results

The experiments are designed in such a way to address the temperature dependence versus the original thin film's thickness by careful study and analyzing the dewetting dynamics (S1-S6, Table I). In the results, we present SEM pictures in step-by-step progress in the morphology of the surface of the samples with experiments of increasing temperatures from 550 °C to 780 °C. However, observations from experiments below T= 550 °C did not present any significant change between before and after the annealing of the sample, since no transformation happened on the thin film. Instead, we observe that if the experiment keeps in longer time a complete dewetting is expected even in the lower annealing temperature [15]. We observed that, when the temperature exceeds T= 620 °C, all the pristine a-Ge thin film transforms into 3-D islands, and then we consider the experiment completed. (Fig. 1c).

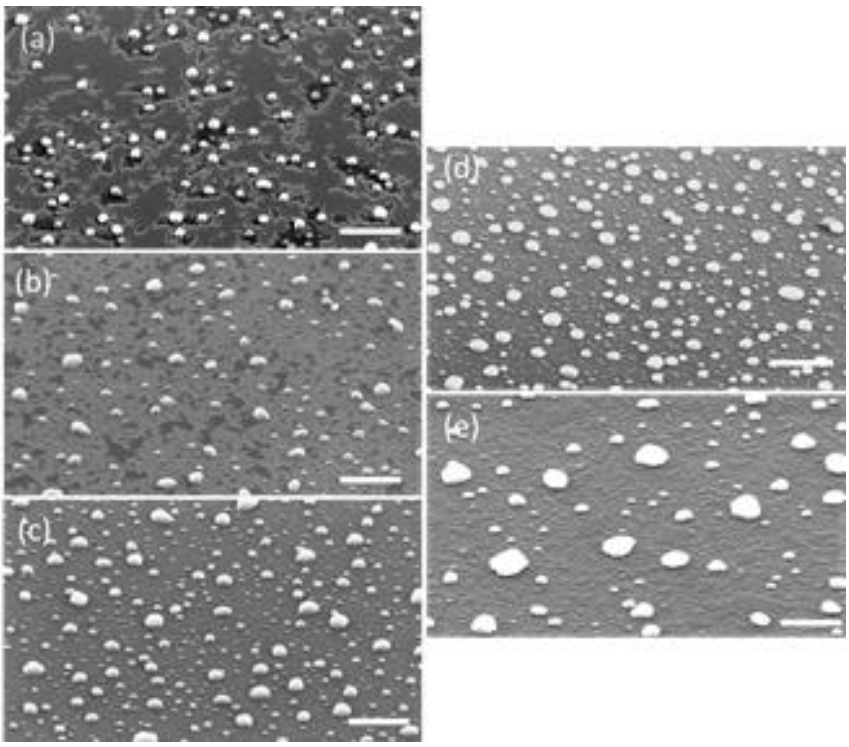

Figure 1: SEM pictures, captured at 45 degrees tilted view of the samples S2 (a), S3 (b), S4 (c), S5 (d), and S6 (e). The white bar corresponds to the distance of 1μm.

The typical dimensions of the formed islands observed by SEM, are between D= 40 nm to D= 150 nm in diameter size. For better understanding, in Figure 1, we can observe SEM imaging of 5 samples showing how increasing temperature leads to different stages in the dewetting process on the surface of the sample at the beginning (Fig. 1a), during (Fig. 1b), and after the end (Fig 1c-1e) of the dewetting process. The formed nanoparticles on the surface appear to co-exist with the amorphous Ge film. At T= 580 °C the original film is still in 2D conditions and another part of the sample is transformed into 3-D islands randomly dispersed onto the SiO_2 substrate. In picture (a) Fig.1, we also observe dendritic canyons (visible as dark trenches in the SEM images) between the Ge islands that are sitting on the underlying SiO_2 layer. These canyons, which appear as white lines in SEM images, are the step between the a-Ge thin film and the exposed SiO_2 substrate. The steps

between the a-Ge and the SiO_2 are formed without any preferential orientation. We can observe the openings on the top of the Ge thin film while uncovering the underlying SiO_2 layer with a parallel formation of the c-Ge island. Those cracks of a-Ge surface later will form bigger openings in a dendritic shape creating a canyon-like surface formation, resulting in the breakdown of the a-Ge film into a discontinuous array. Since the breakdown of the surface has occurred, we observe two different competitive surface areas. One is the a-Ge which is still in 2-D conditions and the other one is the surface of the exposed SiO_2. Openings and island formation are highly spatially non-uniform which is typical of spontaneous phenomena, where nucleation occurs randomly on the sample surface, as shown in Figure 2 a-c, where we report SEM images of three different locations on the S2 sample. We ascribe this feature to non-ideal thermal contact between the substrate and the molybdenum block that causes temperature gradients, in particular between center and edges, typical of small samples, which are more relevant at the onset of the dewetting process.

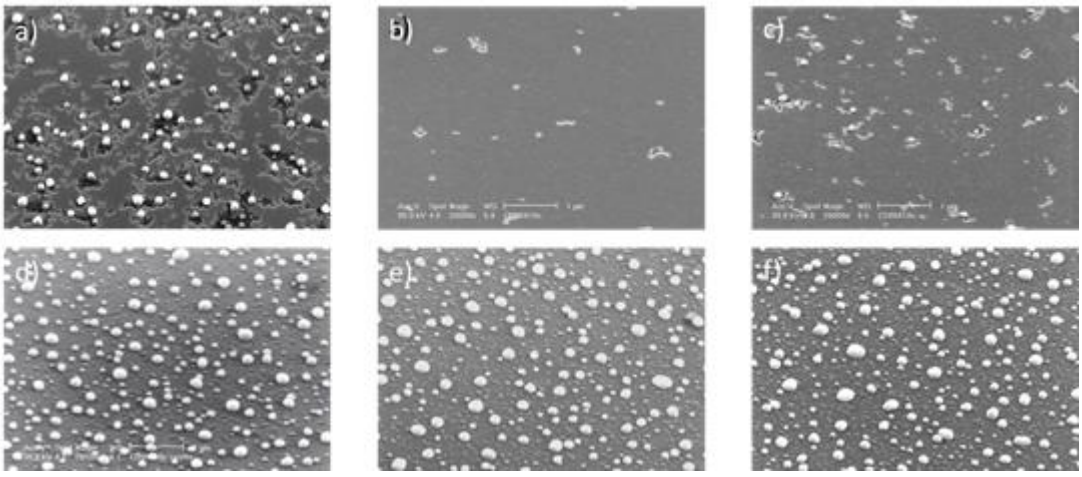

Figure 2: In upper line: SEM images were taken in different spots at low annealing temperature (T = 580 °C). The lower line (d)-(f): SEM images taken in different spots of the sample at high annealing temperature (T = 750 °C).

Obtaining more homogeneous samples in terms of dewetting stage and island size distribution would be preferable especially when applications are concerned (such as Mie resonators for light management). Although this issue goes beyond the aim of this thesis chapter, we mention that the use of larger substrates, higher temperature, or longer annealing time would improve these figures of merit. In the following, we give attention to SEM pictures collected at the sample's centers, minimizing edge effects narrowing the search only to the results from the D=15 nm original thin film thickness series.

In sample S3 in Fig. 1b we can observe that the thin film loses connectivity by increasing the temperature at T=620 °C accompanied by massive material diffusion towards the nano-islands. Island's surface density is about $25\pm 3 \times 10^8$ cm^{-2} and their average diameter as shown in Table 1, is 73 ± 23 nm. Increasing further the annealing substrate temperature at T = 680 °C (S4, Figure 1c), the film is now transformed and the SiO_2 is now dominant in the sample's area due to the complete dewetting process. We can observe that uniformity all over the sample concerning the nano-islands size. This a clue that the morphology of the surface can be obtained when dewetting is complete in contrast with the dewetting in lower temperature. The average nanoisland's size is reduced from D= 115 ± 30 nm at annealing temperature, T = 580 °C (S2) to D = 55 ± 10 nm at the experiment with annealing temperature, T = 680°C (S4), while the islands' density increases to $40\pm2 \times 108$ cm^{-2}. When the temperature goes beyond this point at T = 750 °C (S5, Fig. 1d) the surface density of the bigger islands didn't change significantly. However, we can see that small islands tend to disappear. In S5 the density of the island is $11\pm1 \times 10^8$ cm^{-2} and their average base size is 110 ± 56 nm. Finally, when the substrate temperature is increased at T = 780 °C (S6, Figure 1e), the small islands which were present in all

the other samples are now in complete extinction. The average size of the islands, in this case, is 120 ± 102 nm accompanied by a density of $9 \pm 1 \times 10^{8}$ cm^{-2}.

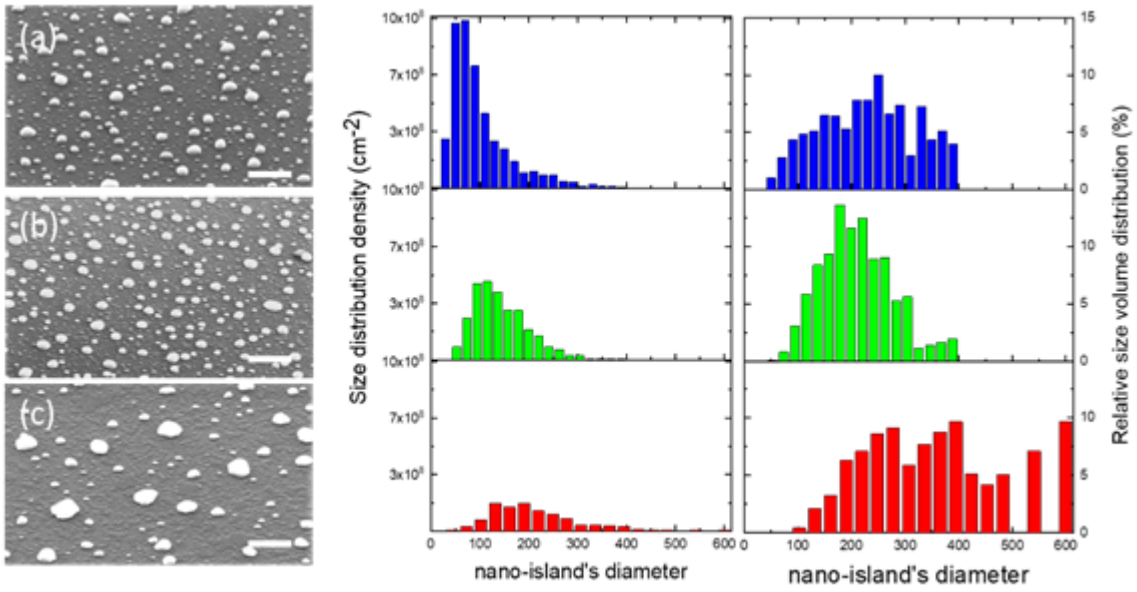

Figure 3: Left panel, from (a) to (c): SEM images in higher temperature 680 °C, 750 °C and 780 °C accordingly. Right panel: (a_1), (b_1) and (c_1) the correspondence size distribution density and (a_2), (b_2) and (c_2) corresponds to relative size distribution volume.

In the following, we analyze the size density distribution between the nano-islands in samples S4-S6 (Fig. 3), so we can understand in deeper detail the characteristics of the samples and their surface morphology. We focused in particular on samples on which the dewetting process is complete, that are of more practical interest. The sample S4 presents an asymmetrical monomodal size distribution with the majority of the islands to be around 50 nm with the presence of a lot of small islands. We can observe that when the temperature is increased to T = 750 °C (sample S5), the small islands do not appear anymore in such big numbers. As a result, the peak average size from the statistics moves towards the bigger islands at 100 nm. If temperature further increases (T = 780 °C - S6), it moves more the peak

average size of the formed islands with the parallel appearance of a tail of big island formation. We can estimate the island volume via the equation: $V_{ISL} = \eta d^3$, where d is the island diameter as estimated from the SEM image and η a geometrical constant that depends on the actual island shape. We assume from the observations that the aspect ratio and shape of the island are the same. The statistics of the volume of the islands are reported in Fig. 3. In samples S4 and S5, by increasing the temperature we drive the system towards the behavior of S5 where size distribution is narrower. Increasing more the annealing temperature we decrease more the broadening in the size distributions and finally, at T = 780 °C (Fig. 3c) the bigger islands whose diameter is larger than 400 nm contain the majority of the dewetted original thin film.

In order to assess in the first stage the crystalline nature of the nano-islands, we observe the dewetting experiment during the annealing process by RHEED. A RHEED halo pattern was observed in every experiment at the low-temperature at T= 550 °C. The arrival of Debye rings starts to appear at temperature T ~ 550 °C (Fig. 4).

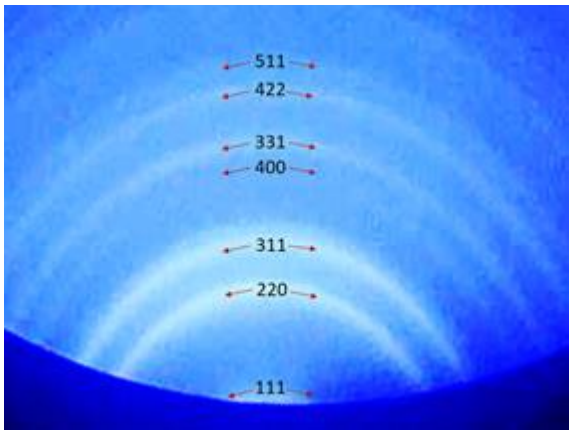

Figure 4: RHEED diffraction pattern obtained on the sample in annealed temperature T= 580 °C. The Bragg plane of the Ge lattice, corresponding to each Debye ring, is attributed.

The presence of Debye rings during the experiment indicates the existence of crystals on the surface. However, nano-islands appear to have random crystallite orientation between them. We observe also that the temperature of rings' appearance corresponds with the formation of the nano-islands in the SEM pictures of the post-annealed sample. The Debye rings are associated with the Ge crystal (511), (422), (331), (400), (311), (220), and (111) planes according to the reference [16], confirming the crystalline nature of the Ge nano-islands.

Another proof of the post-annealed crystallization of amorphous Ge thin films, came from micro-Raman measurements and the results indicate the crystalline nature of Ge islands locally, testing randomly picked areas. Indeed, Raman spectroscopy can give more detailed insight into the morphology and the structure of the islands. Fig. 5 is presented as the results of a Raman mapping of sample S6, where the dewetting is complete. The typical spectrum collected from the annealed sample is shown in panel (a), in comparison with a reference bulk Ge.

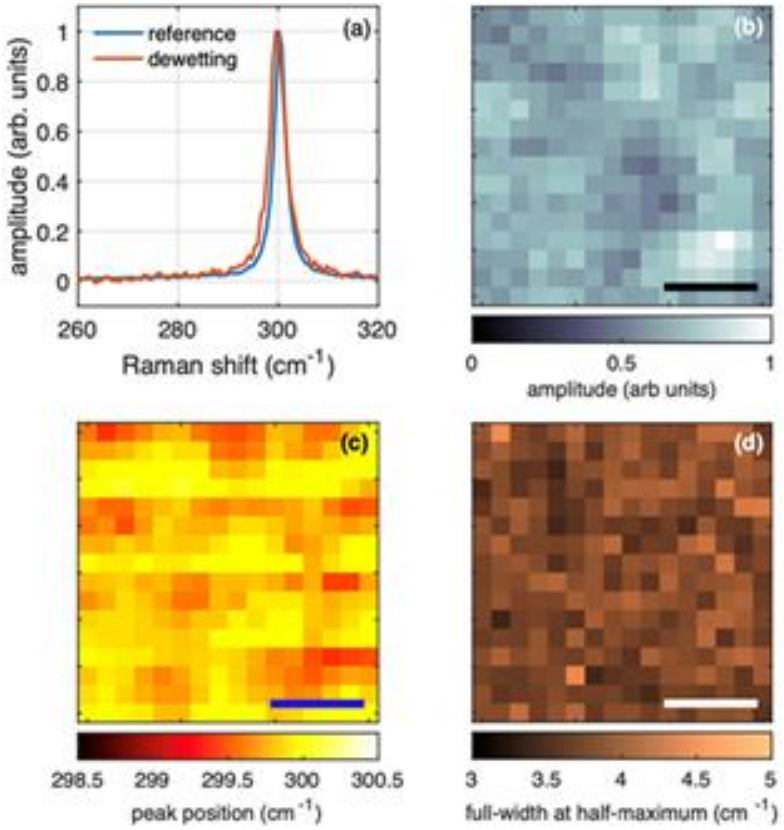

Figure 5: Micro-Raman spectroscopy measurements of sample S6. a) Crystalline Ge islands spectra and a reference bulk germanium sample, b) Peak intensity, c) Peak position, d) FWHM. The measurements were done in a 3 μm x 3 μm area and the spectra were done by a step of 200 nm. The micro-RAMAN characterization was done in a post-annealed sample at high temperature T=780°C to avoid any possibility of surviving a-Ge thin film between the c-Ge islands. The thick mark in (b), (c), and (d) is 1 μm wide.

Panel a), Fig. 5, shows typical micro-Raman measurements, where the Ge peak at 300 cm-1 the FWHM values indicates good crystal quality for the post-annealed islands formation and a good indication that no amorphous Ge thin film remained. The two spectra are nearly superimposed and we find no signal from the amorphous germanium, which typically is between 280 and 290 cm^{-1} [17]. The small shift towards lower frequency for the sample obtained by dewetting with respect to the bulk crystalline Ge we took as a reference sample, is a result of the small residual

strain of the order of 0.1% [18] which can occur due to a residual strain from the mismatch of the thermal expansion coefficient between Ge and SiO_2. The panels (b) to (d) present the result of the curve fitting of a Raman mapping collected from a 3×3 μm^2 region of sample S6. More specifically, Panel b), indicates the homogenous RAMAN scattering intensity of the measured islands. However, the small differences are coming from the fact that the intensity of each measurement is correlated with the volume within the spot. That means that whenever the laser spot is on the top of a bigger island that occupies most of the laser targeting spot, then the Raman intensity is higher. Smaller islands respectively, occupy less area and as result, they can appear as lower Raman intensity. This is visible in the same panel where the white area in the top right map is whiter than the area below which is more colorful. In Panel c, we can observe the width of the measurements that give us the crystalline quality of the formed islands. Furthermore, we can also conclude that the uniformity of the width means that in every single measured spot the crystallinity did not change significantly. Finally, in Panel d, we observe the diversion in the peak position of the measured islands. The modulation of about 0.5 cm^{-1}, which is close to instrumental resolution can be explained due to the shift in peak position is the heat dissipation of the smaller islands compared with one of the big islands. Since the big islands dissipate heat slower than the smaller ones, the peak position should move towards lower frequencies [19, 20].

3.2 Discussion

We intend to arrive at Ge-islands after annealing with a recipe with the particular final size of islands, using various substrate temperatures and different original thin film thicknesses. We can achieve a particular size, for the 3-dimensional islands, by pre-determine the architecture of the final product we need. We have seen

surface diffusion models, driven by surface energy minimization, predicted that thin films can be transformed into rims and fingers on top of the substrate [21, 22]. The case which is studied in this chapter thesis, however, is driven by the formation of microcrystals which are working as nucleation point seed to form an island. By minimizing the energy into the crystalline seeds, can cause the refinement of the atoms inside this crystallite and therefore into a well-defined structure for the atoms. In the end, we have crystalline islands and a fully broken original thin film [12]. Compared to c-Ge film dewetting [23], the metastable a-Ge samples are involved under an annealing step. In the literature is possible to find examples of dewetting dynamics of crystalline SiGe thin films [4,13,24], or crystalline Ge [23], which their annealing temperature goes beyond 700 °C while for amorphous Ge the temperature to obtain crystalline islands is in the range of 600 °C.

According to our experiments, the dewetting of the a-Ge thin film begins at T=580 °C, however, results on a-Ge dewetting show that the island's formation starts at 275 °C [10] obtaining a full crystalline island configuration surface structure [10]. Indeed, in our case, the use of high annealing temperature can be detected on the appearance of GeOx on the surface [24], or even the use of thicker original thin film. As opposed to what was founded in reference [24], the morphology on the surface is dominated by the amorphous Ge film, along with the trenches formation. The native oxide is typically a few nm and in particular, Ge oxide is unstable and can be deformed quickly during the heat treatment [25, 26]. Thus, we choose to perform only the annealing step as a cleaning step, instead of using chemicals that can damage the surface outside of the protective environment of the MBE machine. Indeed, for the application purposes such as photonic devices, it must avoid any introduction of acids, like HF, to protect the surface from any damage. We observed dewetting experiments after the ex-situ cleaning step with HF that the surface was damaged

and dewetting was impossible to proceed properly. Sample S2 at Fig.1a, shows that dewetting occurs with the coexistence of Ge particles and the precursor amorphous thin film within the same area, while in spinodal solid state dewetting, the formed islands are coming from the retreating thin film [27]. One of the problems of this process is the diverse island's size, as we can observe from the statistical analysis of the present chapter. However, from the literature, we can say that this problem is well-known among the spontaneous dewetting processes, and it can be eliminated by using assisted methods of dewetting with lithographic operation on the surface [6-8]. Using these techniques we can obtain very narrow size dispersion with a small standard deviation. One of the most interesting features of the sample morphology is the dendritic shape observed in the a-Ge thin fil's openings. This characteristic is what makes this class of samples concerning the ones in crystalline films after dewetting. In the former case, the dewetting dynamics is regulated by the minimization of the surface energy [28] and it is indeed in conflict with the increase of the Ge vacuum interface caused by this dendritic shape [27].

Observations were done and from the analysis of the samples, we can conclude that two parallel phenomena are occurring which can affect the metastable state of the a-Ge thin film. The first one is the nucleation of the crystalline seeds in the a-Ge film and the surface energy minimization as mentioned in Ref. [27]. In crystalline Ge films, the only role at play is just the minimization of the surface energy for the dewetting dynamics. On the other hand, in the case of a-Ge thin film the minimization surface energy is coming in a second and minor role in the evolution of dewetting dynamics. But still, minimization of surface energy is the one responsible for shaping the c-Ge islands which present a 3D shape that is the minimum surface energy cost. Therefore, the overall concept is driven by the

nucleation of the crystals within the a-Ge and thus, the increase in size due to the mass transport into the nucleation points from the metastable a-Ge thin film.

In contrast with the higher temperatures, with the use of lower annealing temperatures (around 550 °C), only a low number of nuclei are present, and therefore there are only a few crystalline seeds for the aggregation of Ge adatoms. Those seeds eventually will form nano-islands by maximizing their size. In contrast, at a higher temperature, there is a higher probability to form extra nucleation points for the formed islands, and thus, the island's density is larger. The dewetting of the film is controlled by the diffusion of the Ge atoms from a-Ge thin film to the c-Ge islands, while in the case of c-Ge dewetting the diffusion occurs on top of Ge film [28]. As observed, the process continues while the Ge bridge is still present between the island and the a-Ge reservoir. Therefore, if an island is isolated, it cannot grow further in size, and in contrast, isolated a-Ge patches can remain unaltered if there is no crystalline seed to attract their mass close to them. In sample S3 we can see the proof of this model, where we can observe a cluster of small islands and the existence of a-Ge patches without any island in the neighborhood. The same process can be observed in sample S4 where there are higher density and lower size of the islands [27]. In this case, the dewetting is finished and we observe the metamorphosis of the a-Ge film into the nano-islands.

By increasing the annealing temperature above this certain point of T= 680 °C, we observe a decrease in the size of the islands, with the parallel exodus of the small islands. We also can see the reduction in the island’s size distribution and a large Ge mass transfer towards the bigger islands. In Fig.3, we can observe this phenomenon, where for each sample above the temperature of 750 °C (sample S5) there is an increase in the average size of the islands. In this case, the small islands are clearly reduced in number in contrast with the sample S4 where small islands are

dominating the sample's area. Finally, in sample S6 at temperature 780 °C, (see Fig. 3c), the number of the islands is low with the total mass of the original thin film to be concentrated into them. This effect is called Ostwald ripening by which the material of small islands is redistributed to bigger and more stable islands. This effect becomes stronger as we increase the annealing temperature driving the size distribution onto a lower number of islands.

3.3 Bibliography

1)Dimosthenis Toliopoulos, Alexey Fedorov, Sergio Bietti, Monica Bollani, Shiro Tsukamoto, Emiliano Bonera, Marco Abbarchi, Andrea Ballabio, Giovanni Isella, Stefano Sanguinetti,'Solid-state dewetting of amorphous Ge thin film SiO_2/Si (001)', Nanomaterials 2020, 10, 2542.

2)Abdennacer Benali, Jean-Benoît Claude, Nicoletta Granchi, Simona Checcucci, Mohammed Bouabdellaoui, Mimoun Zazoui, Monica Bollani, Marco Salvalaglio, Jérôme Wenger, Luc Favre, David Grosso, Antoine Ronda, Isabelle Berbezier, Massimo Gurioli, Marco Abbarchi, 'Flexible photonic devices based on dielectric antennas', Journal of Physics: Photonics, 2020, 2, 015002.

3)F. Leroy et al, 'How to control solid state dewetting: A short review', Surface Science Reports 2016 71, 391.

4)ESutter and P Sutter, 'Assembly of Ge nanocrystals on SiO2 via a stress-induced dewetting process', Nanotechnology, 2006, 17, 3724.

5)Carl V. Thompson, 'Solid-State Dewetting of Thin Films', Annu. Rev. Mater. Res, 2012, 42, 399.

6)Meher Naffouti, Rainer Backofen, Marco Salvalaglio, Thomas Bottein, Mario Lodari, Axel Voigt, Thomas David, Abdelmalek Benkouider, Ibtissem Fraj, Luc Favre, Antoine Ronda, Isabelle Berbezier, David Grosso, Marco Abbarchi, Monica Bollani, 'Complex dewetting scenarios of ultrathin silicon films for large-scale nanoarchitectures', Sci. Adv., 2017, 3, 1472.

7)M. Aouassa, I. Berbezier, L. Favre, A. Ronda, M. Bollani, R. Sordan, A. Delobbe, P. Sudraud, 'Design of free patterns of nanocrystals with ad hoc features via templated dewetting', Appl. Phys. Lett. 2012, 101, 013117.

8)I. Berbezier, M. Aouassa, A. Ronda, L. Favre, M. Bollani et al, 'Ordered arrays of Si and Ge nanocrystals via dewetting of pre-patterned thin films', J. Appl. Phys., 2013 113, 064908.

9)Marco Abbarchi, Meher Naffouti, Mario Lodari, Marco Salvalaglio, Rainer Backofend, Thomas Botteina, Axel Voigt, Thomas Davida, Jean-Benoît Claude, Mohammed Bouabdellaoui, Abdelmalek Benkouider, Ibtissem Fraj, Luc Favre, Antoine Ronda, Isabelle Berbezier, David Grosso, Monica Bollani, 'Solid-state dewetting of single-crystal silicon on insulator: effect of annealing temperature and patch size', Microelectronic Engineering, 2018, 1, 190.

10)Yutaka Wakayama, Takashi Tagami, Shun-ichiro Tanaka, 'Three-dimensional islands of Si and Ge formed on SiO2 through crystallization and agglomeration from amorphous thin films', Thin Solid Films, 1999, 350, 300.

11)Fabien Cheynis, Frédéric Leroy, Pierre Müller, 'Dynamics and instability of solid-state dewetting', C. R. Physique, 2013, 14, 578.

12)Meher Naffouti, Thomas David, Abdelmalek Benkouider, Luc Favre, Antoine Ronda, Isabelle Berbezier, Sebastien Bidault, Nicolas Bonod and Marco Abbarchi, 'Fabrication of poly-crystalline Si-based Mie resonators via amorphous Si on SiO2 dewetting', Nanoscale, 2016, 8, 2844.

13)P. P. Zhan, B Yang, P P Rugheimer, M M Roberts, D E Savage, Feng Liu and M G Lagally, 'Influence of germanium on thermal dewetting and agglomeration of the silicon template layer in thin silicon-on-insulator', J. Phys. D: Appl. Phys., 2009, 42, 175309.

14)C. Rosenblad, H. R. Deller, A. Dommann, T. Meyer, P. Schroeter, and H. von Känel. 'Silicon epitaxy by low-energy plasma enhanced chemical vapor deposition', J. Vac. Sci. Technol. A, 1998, 16, 2785.

15)M Aouassa , L Favre , A Ronda, H Maaref and I Berbezier, 'The kinetics of dewetting ultra-thin Si layers from silicon dioxide', 2012 New J. Phys. 14 063038.

16)Z.H. Cao · P. Liu · X.K. Meng · S.C. Tang · H.M. Lu, ‘In situ transmission electron microscopy observations of the crystallization of amorphous Ge films’, Appl Phys A, 2009, 94, 393–398.

17)J. Fortner, R. Q. Yu, and J. S. Lannin, ‘Raman scattering of amorphous germanium clusters and ultrathin films’, Journal of Vacuum Science & Technology A, 1990, 8, 3493.

18)M Bollani, D Chrastina, A Fedorov, R Sordan, A Picco and E Bonera, ‘Ge-rich islands grown on patterned Si substrates by low-energy plasma-enhanced chemical vapour deposition’, Nanotechnology, 2010, 21, 475302.

19)Poborchii, V., Bouabdellaoui, M., Uchida, N., Ronda, A., Berbezier, I., David, T., & Favre, L, ‘Raman microscopy and infrared optical properties of SiGe Mie resonators formed on SiO2 via Ge condensation and solid state dewetting’, Nanotechnology, 2020, 31(19), 195602.

20)Mitsai, E., Naffouti, M., David, T., Abbarchi, M., Hassayoun, L., Storozhenko, D., Mironenko, A., Bratskaya, S., Juodkazis, S., Makarov, S. and Kuchmizhak, A., ‘Si 1− x Ge x nanoantennas with a tailored raman response and light-to-heat conversion for advanced sensing applications’, Nanoscale, 2019, 11(24), pp.11634-11641.

21)D. J. Srolovitz, ‘Capillary instabilities in thin films. I. Energetics’, Journal of Applied Physics, 1986, 60, 247.

22)D. J. Srolovitz, ‘Capillary instabilities in thin films. II. Kinetics’, Journal of Applied Physics, 1986 60, 247.

23)F. Leroy, F. Cheynis, T. Passanante, and P. Muller, ‘Influence of facets on solid state dewetting mechanisms: Comparison between Ge and Si on SiO2’, Physical Review B, 2013, 88, 035306.

24)A. A. Shklyaev and A. V. Latyshev, ‘Dewetting behavior of Ge layers on SiO2 under annealing’, Scientific Reports, 2020, 10, 13759.

25)Bollani et al., ‘Templated dewetting of single-crystal sub-millimeter-long nanowires and on-chip silicon circuits’, Nature Communications, 2019, volume 10, Article number: 5632, s41467-019-13371-3

26)Y. Almadori, et al., ‘From Solid-State Dewetting of Ultrathin, Compressively Strained Silicon–Germanium-on-Insulator Films to Mastering the Stoichiometry of Si1–xGex Nanocrystals’, Journal of Physical Chemistry C, 2016, 120.13: 7412-7420

27)David T. Danielson, Daniel K. Sparacin, Jurgen Michel, and Lionel C. Kimerling, ‘Surface-energy-driven dewetting theory of silicon-on-insulator agglomeration’, Journal of Applied Physics, 2006, 100, 083507.

28)Zheng Gai, Hongbin Yu, and W. S. Yang, ‘Adatom diffusion on Ge.111. and the corresponding activation energy barrier’, Physical Review B, 1996, 53, 20.

Chapter 4: Fabrication and characterization of Si-based dielectric Mie resonators

This chapter is based on recently published work from D. Toliopoulos et. al. [1] and the results are presented in the following. More specifically, the fabrication of dielectric Mie resonators and their optical characterization is discussed. This work was part of the secondment period spent at the University of Marseille in France. The main goal of the experiments was to obtain well-defined nanoparticles by using the solid state dewetting technique discussed in the previous chapter to test their optical response. In the following, we will address individual monocrystalline islands fabricated by optical lithography and solid state dewetting. Afterward, extensive results from Dark Field spectroscopy and simulations will be presented.

As discussed in the previous chapters, Mie resonators are all-dielectric antennas with reduced absorption losses and high permittivity which make them an ideal candidate for light-matter interaction and light manipulation, potentially enriching the current performances of photonic devices [2]. Scattering with resonance by individual dielectric nano-islands can be broad [3] (around 50-100 nm mostly at visible and near-IR) and certainly interacting with the substrate where the film is deposited [4]. Likewise, individual resonators, the contrast intensity between min and max is poor. In order to surpass this issue, is to couple the nano-resonators between them, thus, forming oligomers that can provide sophisticated functions along with sharp resonances [2,5]. Nonetheless, this concept demands a more advanced fabrication technique to accurately fix the size, shape, and relative position

of the dielectric resonators by setting small gaps between them. An alternative method had been used by reference [6] is to immerge Mie resonances (Si nano-pillars) with the Fabry-Perot modes to improve resonances to be used as anti-reflective coatings.

In this chapter, the goal is to study and present more defined structural colors exploited from the Mie resonators with respect to the photonic modulation of the underlying thick SiO_2 by fabricating Si islands assisted with low-resolution optical lithography and plasma etching. Once the pattern is completed the sample will be inserted in the ultra-high vacuum of the MBE chamber to perform solid-state dewetting [7-13]. In this chapter, it is presented that Silicon nano-islands' far-field scattering intensity [4] can be coupled with the etalon effect. The efficiency of the Mie scattering out-couples the light interfering with the etalon depending on the nano-islands' size and drives the light at smaller angles compared to the one from the incident beam. Eventually, we got colors that cover the visible spectrum along with resonances with the contrast between min and max of the intensity.

4.1 Results

The Si on insulator thin film is a single crystal film which is deposited on a thick buried oxide layer resting on the top of Silicon (100) wafer (see Fig. 1, left panel). The thickness of the thin film is 125 nm and it was thinned to reach 20 nm by rapid thermal oxidation (RTO) in high temperature (950 ºC) with Oxygen flow atmosphere. The thinning process lasted for 3 hours for the surface of the Silicon to oxidize. Later, the substrate was dipped in a 10% HF solution with 90% Deionized H_2O to remove the recently formed oxide layer.

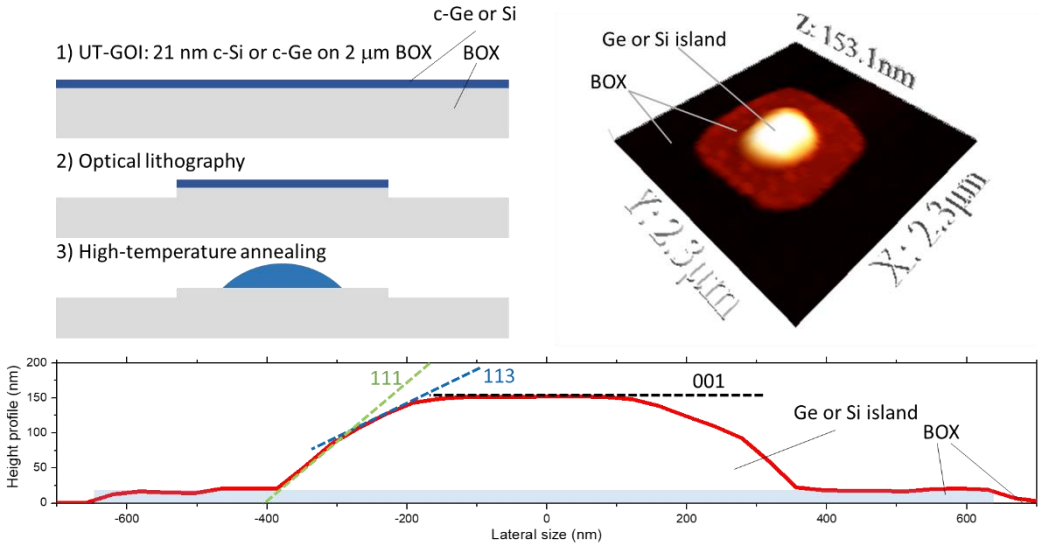

Figure 1: Left panel: Scheme of the fabrication process. 1) The crystalline, ultra-thin silicon on insulator (c-UT-SOI). 2) Optical lithography and plasma etching. 3) High temperature annealing in ultra-high vacuum. Right panel: A 3D representation of the island. Bottom panel: Atomic force microscope profile of an individual island. The main crystal facets are highlighted.

For the assisted dewetting experiments, the fabrication of the islands passes through a double step. First, it is patterned by optical lithography and later dewetting in high temperature as discussed also in the previous chapter [10, 12-14]. The patterns made by the optical lithography were obtained by spin-coating a positive photosensitive resist which was exposed to a near-UV laser at λ= 375 nm using power of 2.7 mW in an area of approximately 2µm. Then the exposed parts with the photoresist are removed by a developer. The final step is the plasma etching step which attacks the exposed Silicon area and thus leaving behind untouched the protected parts. The square size of the patches is between 3 and 4 µm in size (Fig. 2).

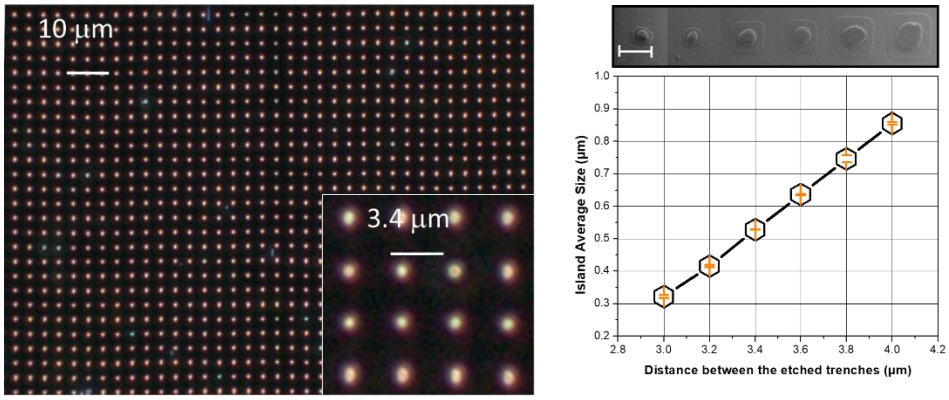

Figure 2: Left panel: Optical dark-field image of a typical array of organized dewetted Si islands. The inset shows the homogeneity of the islands obtained with a periodicity of 3.4 µm. Right panel: Average island size as a function between the etching pitch as obtained by scanning electron micrographs (SEM). The error bar represents the standard deviation. The line is a guide for the eyes. The top inset shows a typical SEM for each etched pitch.

The cleaning step of the samples consists of ethanol and acetone, NO_2 plasma archer and in the end a 5% solution HF under Nitrogen atmosphere inside a fume hood. Later on, the samples were transferred into the ultra-high vacuum of the MBE chamber. Likewise the previous chapter experiment, also in this case before the annealing there is a degassing stage where the substrate is exposed to heat treatment at 650 ºC for half an hour and then dewetting occurs at 750 ºC for another half an hour.

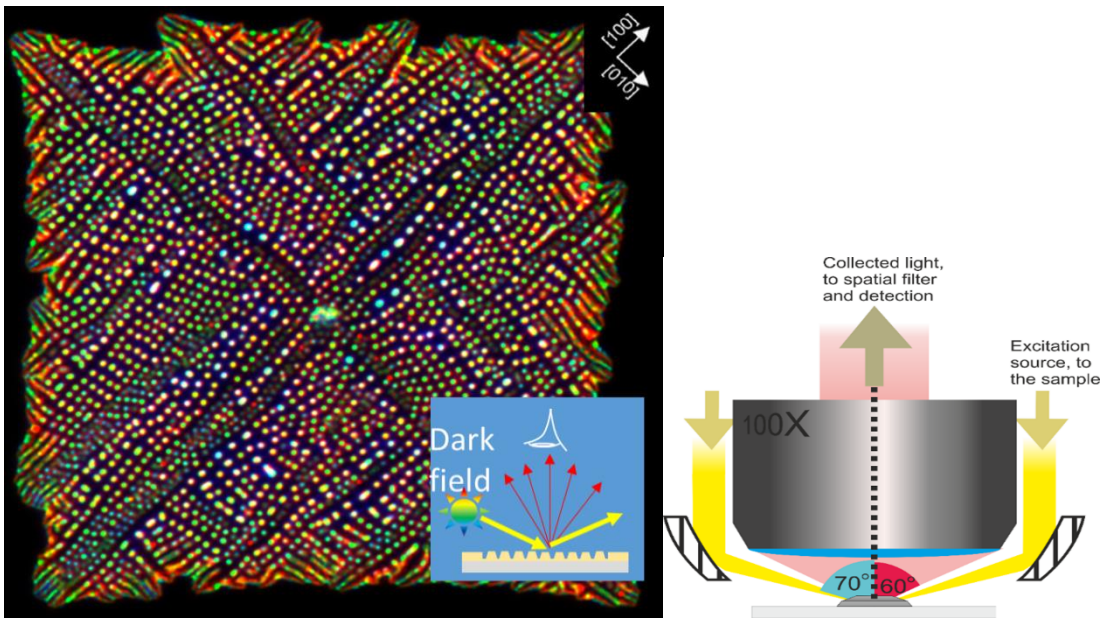

Figure 3: Left panel: Dark Field imaging of a fully spontaneous dewetted sample. Right panel: Collection of scattered light by an optical microscope.

An optical microscope (ZEISS Axio Observer) with a 100X magnification objective lens (numerical aperture NA = 0.9) was used to collect the Dark Field (DF) images and spectra. The microscope is working in both dark and bright modes. A CCD (Flame-T-VIS-NIR by Ocean Optics) along with a spectrometer was used to study the individual islands scattering profiles. Finally, an optical fiber was used (Ocean Optics multimode fiber, VIS-NIR, core diameter 200 mm) to collect the scattered light. Furthermore, an SEM set-up was used in FEI Helios 600 Nano-Lab within the University of Marseille to perform the imaging of the individual islands (Fig. 3 right panel). Micrographs were acquired using a through-the-lens detector secondary electron detector (5 kV acceleration voltage), probe current of 0.17 nA, and a working distance of 4.2 mm. A dark field image is shown in Fig. 3, the Left panel from a sample with the spontaneous dewetting pattern.

To clarify the influence of the 2 μm thick BOX layer on the island scattering spectra, numerical calculations were performed with a commercial three-

dimensional 3D finite-difference time domain (FDTD) code (CrystalWave, Photon Design). We consider a hemispherical Si island with a 200 nm base diameter and a refractive index n = 4, neglecting absorption. The Si island is excited with a broadband point-like dipole (emitting at λ = 600 nm, with a full width at half maximum FWHM = 300 nm) positioned in the middle of the island, with polarization parallel to the BOX surface. The flux of the Poynting vector across a box sensor, a cube of side 300 nm, positioned around the exciting dipole gives us the LDOS of the island at the dipole position [15].

After the solid state dewetting process, we were able to develop monocrystalline and smooth nano-islands, with the typical facets exposed as discussed before (see Fig. 1) [8-11,13,15]. In Fig. 2, we can see large arrays of islands with well-defined sizes (around 280-800 nm) along with regular organization [9,12,16,17]. Capturing the scattering profiles of the islands with the DF spectroscopy we can see good homogeneity in colors and therefore, also in size. The height of the island can differ from 90 to 150 nm, and this is because of the different size of the original patch size. However, small size nano-islands can be obtained by reducing the patch size with the lithographic method.

For the optical spectroscopy of the islands at the visible frequency, we had performed numerous characterization and some of the spectra are presented in Fig. 4 along with their HR-SEM characterization. We can observe High Resolution SEM images of different Mie-resonators in increased diameter size. The particles have in general a round shape. Moreover, in some other cases, we can see a small nose for the islands of 110 and 120 nm respectively, as a result of the dewetting method. The size of the particle was measured by calculating the average size in the different axis of the spheres. The scale bar in Fig. 4, at the bottom, corresponds to 200 nm. Each one of the images was taken selectively from a lithographic made pattern using laser

writing. (Fig. 2) [9, 10, 12, 15]. Slight shape asymmetries observed in some islands are ascribed to a non-complete dewetting that did not lead to the final equilibrium shape of silicon crystals. In principle, these defects could be improved with a longer annealing time or a higher temperature.

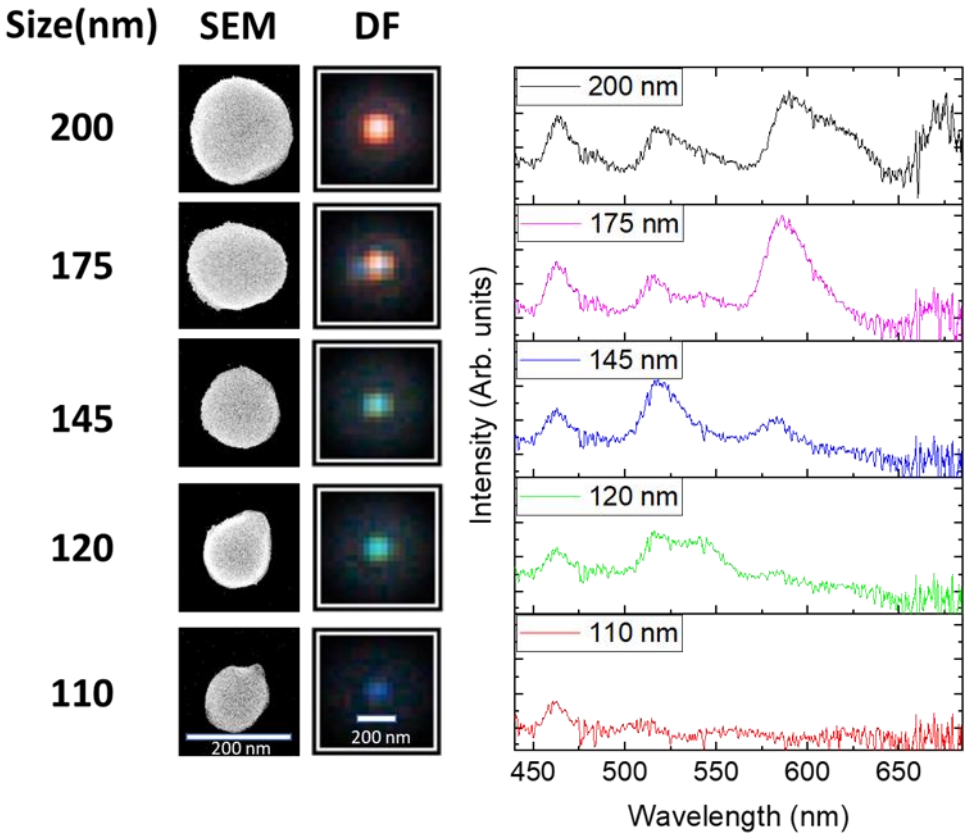

Figure 4: A selective SEM picture with clear DF spectra after refinement. We clearly see the photonic modes on the spectra.

Dark-field images reveal a net colorization from blue to red, when increasing particle size (Fig. 4), middle column). We can observe the redshift of the color as we increase the particle size from 110 nm to 200 nm with blue the smallest and red the largest one. In this case, the scale bar is 600 nm. The corresponding scattering spectra (Fig. 4, after normalization by the white lamp used for illumination) confirm this

tendency, showing several sharp bands that increase in number at long wavelengths for larger islands [10, 12]. These resonances share a similar spectral position and spacing between them, although some differences (up to 25-30 nm) are observed [4]. These differences can be accounted for by imperfections in the etching (locally thicker or thinner BOX), incomplete dewetting leaving some pristine c-UT-SOI nearby the islands, residual Si particles on the BOX nearby the islands, intermixing of Si and SiO_2 [17–19], and asymmetries in the dewetted islands [10].

The proof of the interference between the resonances and the substrate we perform simulations of a specular reflection from a 2 μm thick SiO_2, like the one used in our experiments, on top of Si substrate. The comparison deals with the observations on the far-field spectra which comes from the constructive and destructive interference of the incident light with the air-SiO_2 and SiO_2-Si interfaces with the strong spectral variations of the driving field in the resonators. Those simulations were superimposed with the dark field collected spectra from the individual islands (see Fig. 5b). Thus, the reflection with incident light at 0 degrees presents 5 broad peaks in the studied spectral range, having a contrast of about 3 (Fig. 5). While for 70 degree incidence, which is closer to the one from the light extracted in the dark field microscope, seems to present similarities, but only with 4 peaks. However, it seems to present a plateau on the top with a lower contrast of roughly 2 (Fig. 5a bottom panel). The last information is explained by observing the s and p polarized components of the reflection: the minima and maxima they present, in opposition of phase thus, providing a more complex behavior compared with the normal incidence, where the two components are identical. It worth noting that at incident angle, the s polarization is dominant with an intensity that is almost double of p polarization.

The scattering profile of the individual island presents four peaks with a large intensity contrast (between 3 and 6, depending on the peak taken into account) (see Fig. 5b). When comparing the case of s polarization at an incidence of 70 degrees, the spectral position and spacing between the scattering peaks show marked similarities with the reflection spectrum of the flat SiO_2 layer (highlighted by the vertical gray lines in (Fig. 5). Also, the s polarized reflection and the broadening of the resonances observed in the scattering spectrum are similar. They present a trend that continues to grow from 25 nm for the shorter wavelength, up to 35 nm for the longer wavelengths. The broadening is rather 3 to 4 times smaller than what is reported for similar islands developed via dewetting on top of 145 nm thick BOX [10], where the etalon effect is not present.

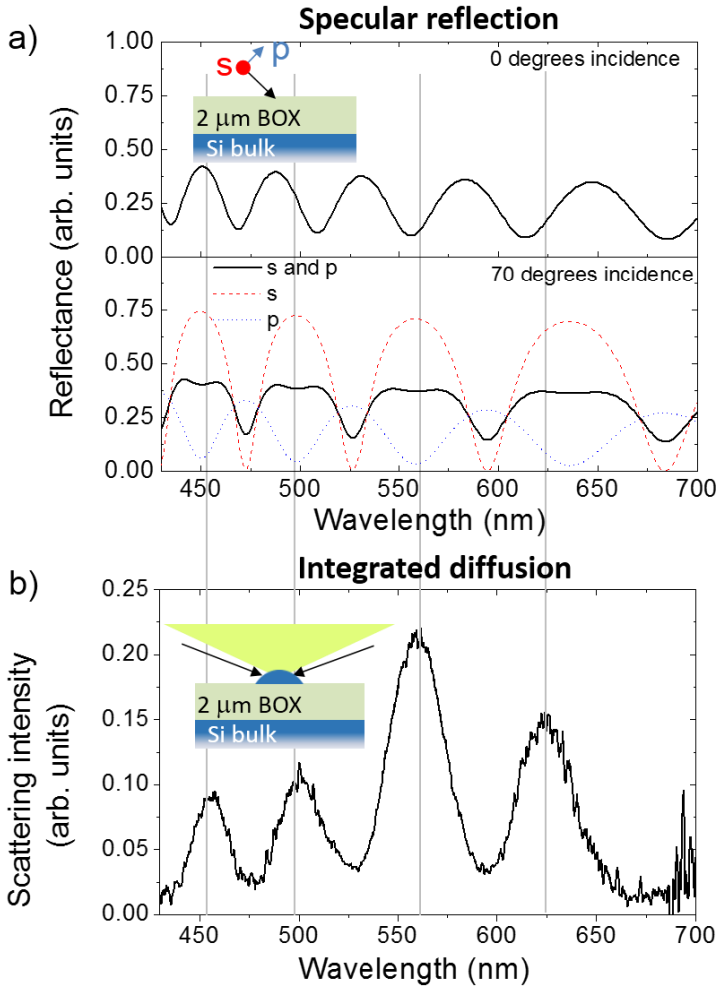

Figure 5: a) Simulated intensity of the specular reflection for s and p polarization from a 2 µm thick SiO_2 layer (BOX) atop Si bulk. Top panel: normal incidence. Bottom panel: 70 degrees incidence. The inset highlights the geometry considered in the model. b) Dark-field scattering spectrum of a dewetted island. The inset highlights excitation and collection conditions (respectively ~70 degrees incidence and within a 64 degrees aperture cone).

4.2 Discussion

During the past years, solid state dewetting for the fabrication of nano-islands had been studied and discussed a lot [10-12]. By utilizing Si and Si(Ge) thin films are possible to obtain Mie resonators in an organized or disorganized manner. Although, fixing organized structures of ordered nano-islands in nanoscale, requires

techniques such as reactive etching [5,21] and e-beam lithography or even focused ion beam [9,12,14,16]. Despite the fact that these methods can be efficient in the nanoscale to develop complex architectures, it can be also costly and not easy to use over full wafers. This is why in our case for the fabrication of nano-islands we use templated methods of photolithography. It is an inexpensive process which in fact can be functionalized in larger areas. However, our nominal resolution of the optical lithography was quite poor, around 2 μm. But, large ordered arrays can be obtained with a minimum distance between the nanoparticles to be 2 μm. Nevertheless, dewetting is the answer to this issue, because the patterned arrays can collapse to a single spot island with a base size of a few nanometers. By controlling the original patch size and the thickness of the thin film we can arrive at a well-ordered template with narrow size distribution and in fact better than reports which can be found in the literature [9,12,14,16]. Those references use a focus ion beam to obtain such ordered arrays. But still similar results can be found on reports with e-beam lithography [11,13]. It is worth mentioning at this moment that atomically smoothed objects with well-faceted interfaces are formed by self-assembly methods [8-10,13,15,21]. This is an important point when considering an application with electronic properties, is less likely to induce a pronounced roughness compared to other top-down methods.

Furthermore, dark field scattering profiles were measured for each one of the corresponding islands as shown in Fig. 4. We can see 4 peaks in the spectra with a broad peak in 600 nm for the 200 nm and 175 nm islands, while in the middle-ranged size islands (145 nm and 120 nm), the broad peak is moved to a lower wavelength around 525 nm signaling the scattered ‘greenish’ colored islands. The peak in the 600 nm is now weakened compared to the bigger islands. Finally, the smaller islands below 120 nm have the characteristic blue color, accompanied by a stronger peak at

460 nm. The previously observed peaks of 600 nm and 525 nm are now almost disappeared. The observation made on the sharp resonance peaks indicate colors that are similar to the ones obtained in ref [12] for SiGe and Si [22] Mie resonators. The colors are possible because of the interference of the sharp resonances that bounce from the etalon effect produced by the buried oxide on the top of the Si wafer. By mixing the top-down and bottom-up approaches, our resonances cannot be scattered and blend in size as for distinct bottom-up methods [23,24].

It is worth noting that similarities are spotted, between the spectrum of the *s* polarization reflection and dark field resonance scattering spectrum of the islands at the 70 degrees of incidence (Fig. 5(b)). Having that in mind we can conclude that some of the light at the air-SiO_2 and SiO_2-Si interfaces, is backscattered by the Mie resonator. However, for this experimental geometry, we cannot detect the incident beam's direct reflection of 70 degrees. Indeed, the area around the nano-islands is dark since the numerical aperture of the detection is 64 degrees. The reflected light is relocated at different angles by the resonant scattering, with respect to the incident ones, while features from the etalon mode interference are preserved.

In addition to the experiments, we perform FDTD simulations to confirm the picture we build, that the island's scattering spectrum is affected by interference effects. That way we can be sure that this phenomenon is not coming from the modification of the LDOS of the Si islands. We simulate the hemispherical Si islands on top of 2 μm thick silica which refractive index is around n=1.5. The whole system rests on 1 μm thick Si with n=4 with the same islands but only on top of Si oxide (see Fig. 6). In parallel to the buried oxide surface, we set a planar sensor in 1 μm distance, to simulate the collected far-field spectrum under several angles (Fig. 6(c)). We consider different conditions of the simulation compared to the experiments and

the goal of those is just to provide more information about the underlying system phenomenology.

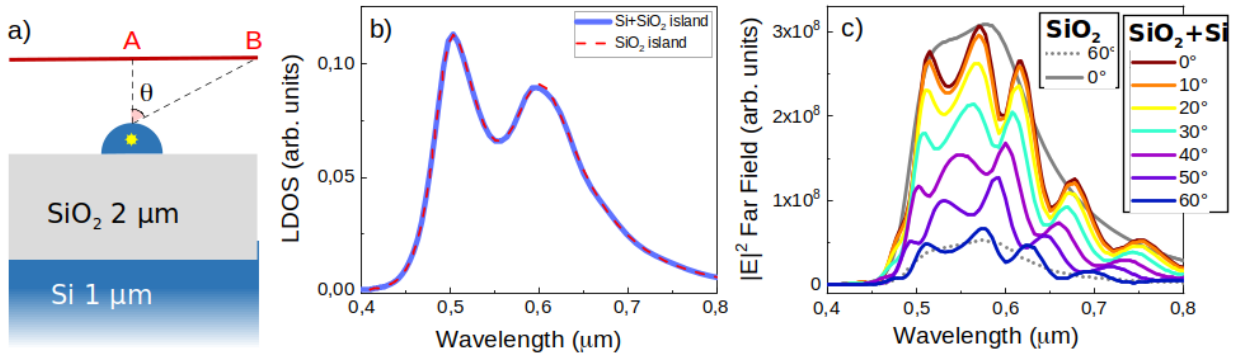

Figure 6: a) A sketch of the FDTD simulation. The structure consists of a silicon island and a 2 μm SiO_2 thin film on top of a 1 μm Si substrate. In the middle of the island is the broadband point-like dipole (emitting with a central wavelength of 600 nm, with a full width at half maximum FWHM = 300 nm) located by a yellow star sign, that acts as an excitation source. The far field sensor is represented by the red line, which is set in a way that point A corresponds at the acquisition angle θ of 0 degrees and point B acquisition angle of 60 degrees. b) Representation of Local Density of States (LDOS) of the island on 2 μm SiO_2 layer only (red dashed line) and on 2 μm SiO_2 plus 1 μm Si (blue line). c) Colored lines: far field simulated spectra acquired at different values of theta for the island atop 2 μm SiO_2 plus 1 μm Si substrate (from θ = 0 to 60 degrees). The continuous line represents the far field intensity from the island with the SiO_2 substrate only at 0 degrees, while the dashed line at 60 degrees.

In Fig. 6 (b) we can see the calculation at the position of the exciting dipole as shown in ref [15] in which 2 resonances in 500 nm and 600 nm are dominant. These two resonances can be identified by the electric and the magnetic modes respectively [4,10,12,21]. The Si-island's LDOS, didn't practically change by the presence of the Si substrate, which is concluded from the fact that the two curves are almost identical. On the other hand, the presence of the Si substrate influences the far field. In Fig. 6 (c) we see the collection of far-field spectra at far-field sensor's different

points. The solid and dashed lines correspond in smooth spectra simulated without the presence of the Si substrate, where we can observe the electric and magnetic dipole (ED and MD modes respectively), characterized by different relative weights. The scattering at 60 degrees is about 6 times weaker than the normal incident one at 0 degrees. The smooth spectra obtained without the Si substrate are superimposed with the far-field spectra which were obtained by the Si substrate which shows a clear intensity modulation. All in all, by the simulations we can answer the question of whether the modulation in the far-field scattering intensity is related to a modification of the LDOS of the nano-islands and the conclusion is that are not related. However, several speculations suggest that are related to the scattering by Mie resonators of the incident light beam propagating and later interfering with the silica film between the islands and the Silicon substrate.

4.3 Conclusions

We showed that solid state dewetting assisted from photolithographic methods can produce arrays in well-defined positions of Si-based nano-islands. By controlling the initial characteristics of the dewetting method we can arrive at the controlled size and islands featuring Mie scattering are in visible frequency. Furthermore, we couple the scattering resonances with etalon mode which allows us to set the position of minima and maxima and thus, enhance the contrast between them compared to the individual nano-islands. Finally, good structural colors can be obtained avoiding the expensive and difficulty in use for large areas fabrication tools. The results are important because such a class of resonators can be used for application [25-27] in quantum emitters as we will see in the next chapter.

The simulation indicates a spectral dependent emission steering of the Mie antenna when coupled with the dielectric etalon. This effect can be exploited for

quantum applications, such as the selective and different directionality in an exciton-biexciton cascade of a quantum emitter [30] embedded in Mie resonators.

4.4 Bibliography

1) D. Toliopoulos, M. Khoury, M. Bouabdellaoui, N. Granchi, J.-B. Claude, A. Benali, I. Berbezier, D. Hannani, A. Ronda, J. Wenger, M. Bollani, M. Guriolli, S. Sanguinetti, F. Intonti, AND M. Abbarchi, 'Fabrication of spectrally sharp Si-based dielectric resonators: combining etaloning with Mie resonances', Optics Express, Vol. 28, No. 25, 2020.

2) T. Liu, R. Xu, P. Yu, Z. Wang, and J. Takahara, "Multipole and multimode engineering in mie resonance-based metastructures," Nanophotonics 9(5), 1115–1137 (2020).

3) T. Coenen, J. van de Groep, and A. Polman, "Resonant modes of single silicon nanocavities excited by electron irradiation," ACS Nano 7(2), 1689–1698 (2013).

4) J. Van de Groep and A. Polman, "Designing dielectric resonators on substrates: Combining magnetic and electric resonances," Opt. Express 21(22), 26285–26302 (2013).

5) Y. Yang, I. I. Kravchenko, D. P. Briggs, and J. Valentine, "All-dielectric metasurface analogue of electromagnetically induced transparency," Nat. Commun. 5(1), 5753–5757 (2014).

6) A. Cordaro, J. Van De Groep, S. Raza, E. F. Pecora, F. Priolo, and M. L. Brongersma, "Antireflection high-index metasurfaces combining mie and fabry-perot resonances," ACS Photonics 6(2), 453–459 (2019).

7) C. V. Thompson, "Solid-State Dewetting of Thin Films," Annu. Rev. Mater. Res. 42(1), 399–434 (2012).

8) M. Aouassa, L. Favre, A. Ronda, H. Maaref, and I. Berbezier, "The kinetics of dewetting ultra-thin si layers from silicon dioxide," New J. Phys. 14(6), 063038 (2012). Research Article Vol. 28, No. 25 / 7 December 2020 / Optics Express 37742

9) M. Aouassa, I. Berbezier, L. Favre, A. Ronda, M. Bollani, R. Sordan, A. Delobbe, and P. Sudraud, “Design of free patterns of nanocrystals with ad hoc features via templated dewetting,” Appl. Phys. Lett. 101(1), 013117 (2012).

10) M. Abbarchi, M. Naffouti, B. Vial, A. Benkouider, L. Lermusiaux, L. Favre, A. Ronda, S. Bidault, I. Berbezier, and N. Bonod, “Wafer scale formation of monocrystalline silicon-based mie resonators via silicon-on-insulator dewetting,” ACS Nano 8(11), 11181–11190 (2014).

11) M. Naffouti, R. Backofen, M. Salvalaglio, T. Bottein, M. Lodari, A. Voigt, T. David, A. Benkouider, I. Fraj, L. Favre, A. Ronda, I. Berbezier, D. Grosso, M. Abbarchi, and M. Bollani, “Complex dewetting scenarios of ultrathin silicon films for large-scale nanoarchitectures,” Sci. Adv. 3(11), eaao1472 (2017).

12) T. Wood, M. Naffouti, J. Berthelot, T. David, J.-B. Claude, L. Métayer, A. Delobbe, L. Favre, A. Ronda, I. Berbezier, N. Bonod, and M. Abbarchi, “All-dielectric color filters using SiGe-based mie resonator arrays,” ACS Photonics 4(4), 873–883 (2017).

13) M. Bollani, M. Salvalaglio, A. Benali, M. Bouabdellaoui, M. Naffouti, M. Lodari, S. Di Corato, A. Fedorov, A. Voigt, I. Fraj, L. Favre, J. B. Claude, D. Grosso, G. Nicotra, A. Mio, A. Ronda, I. Berbezier, and M. Abbarchi, “Templated dewetting of single-crystal, ultra-long nano-wires and on-chip silicon circuits,” Nat. Commun. 10(1), 5632 (2019).

14) M. Naffouti, T. David, A. Benkouider, L. Favre, A. Ronda, I. Berbezier, S. Bidault, N. Bonod, and M. Abbarchi, “Fabrication of poly-crystalline si-based mie resonators via amorphous si on sio 2 dewetting,” Nanoscale 8(14), 7768 (2016).

15) D. Pellegrino, D. Balestri, N. Granchi, M. Ciardi, F. Intonti, F. Pagliano, A. Y. Silov, F. W. Otten, T. Wu, K. Vynck, P. Lalanne, A. Fiore, and M. Gurioli, “Non-lorentzian local density of states in coupled photonic crystal cavities probed by near-and far-field emission,” Phys. Rev. Lett. 124(12), 123902 (2020).

16) I. Berbezier, M. Aouassa, A. Ronda, L. Favre, M. Bollani, R. Sordan, A. Delobbe, and P. Sudraud, “Ordered arrays of si and ge nanocrystals via dewetting of pre-patterned thin films,” J. Appl. Phys. 113(6), 064908 (2013).

17) M. Naffouti, T. David, A. Benkouider, L. Favre, A. Delobbe, A. Ronda, I. Berbezier, and M. Abbarchi, “Templated solid-state dewetting of thin silicon films,” Small 12(44), 6115–6123 (2016).

18) F. Leroy, Y. Saito, S. Curiotto, F. Cheynis, O. Pierre-Louis, and P. Müller, “Shape transition in nano-pits after solid-phase etching of sio2 by si islands,” Appl. Phys. Lett. 106(19), 191601 (2015).

19) F. Leroy, T. Passanante, F. Cheynis, S. Curiotto, E. Bussmann, and P. Müller, “Catalytically enhanced thermal decomposition of chemically grown silicon oxide layers on si (001),” Appl. Phys. Lett. 108(11), 111601 (2016).

20) M. Trautmann, F. Cheynis, F. Leroy, S. Curiotto, and P. Müller, “Interplay between deoxidation and dewetting for ultrathin soi films,” Appl. Phys. Lett. 110(16), 161601 (2017).

21) M. Bouabdellaoui, S. Checcucci, T. Wood, M. Naffouti, R. P. Sena, K. Liu, C. M. Ruiz, D. Duche, J. Le Rouzo, L. Escoubas, G. Berginc, N. Bonod, M. Zazoui, L. Favre, L. Metayer, A. Ronda, I. Berbezier, D. Grosso, M. Gurioli, and M. Abbarchi, “Self-assembled antireflection coatings for light trapping based on sige random metasurfaces,” Phys. Rev. Mater. 2(3), 035203 (2018).

22) M. Naffouti, M. Salvalaglio, T. David, J.-B. Claude, M. Bollani, A. Voigt, A. Benkouider, L. Favre, A. Ronda, I. Berbezier, A. Delobbe, A. Houel, and M. Abbarchi, “Deterministic three-dimensional self-assembly of si through a rimless and topology-preserving dewetting regime,” Phys. Rev. Mater. 3(10), 103402 (2019).

23) M. Salvalaglio, M. Bouabdellaoui, M. Bollani, A. Benali, L. Favre, J.-B. Claude, J. Wenger, P. de Anna, F. Intonti, A. Voigt, and M. Abbarchi, “Hyperuniform

monocrystalline structures by spinodal solid-state dewetting," Phys. Rev. Lett. 125(12), 126101 (2020).

24) V. Flauraud, M. Reyes, R. Paniagua-Dominguez, A. I. Kuznetsov, and J. Brugger, "Silicon nanostructures for bright field full color prints," ACS Photonics 4(8), 1913–1919 (2017).

25) W. Chaabani, J. Proust, A. Movsesyan, J. Beal, A.-L. Baudrion, P.-M. Adam, A. Chehaidar, and J. Plain, "Large-scale and low-cost fabrication of silicon mie resonators," ACS Nano 13(4), 4199–4208 (2019).

26) A. Benali, J.-B. Claude, N. Granchi, S. Checcucci, M. Bouabdellaoui, M. Zazoui, M. Bollani, M. Salvalaglio, J. Wenger, L. Favre, D. Grosso, A. Ronda, I. Berbezier, M. Gurioli, and M. Abbarchi, "Flexible photonic devices based on dielectric antennas," JPhys Photonics 2(1), 015002 (2020).

27) 26. B. Rolly, B. Stout, and N. Bonod, "Boosting the directivity of optical antennas with magnetic and electric dipolar resonant particles," Opt. Express 20(18), 20376–20386 (2012).

28) R. Regmi, J. Berthelot, P. M. Winkler, M. Mivelle, J. Proust, F. Bedu, I. Ozerov, T. Begou, J. Lumeau, H. Rigneault, M. F. García-Parajó, S. Bidault, J. Wenger, and N. Bonod, "All-dielectric silicon nanogap antennas to enhance the fluorescence of single molecules," Nano Lett. 16(8), 5143–5151 (2016).

29) I. Suarez, T. Wood, J. P. M. Pastor, D. Balestri, S. Checcucci, T. David, L. Favre, J. B. Claude, D. Grosso, A. F. Gualdron-Reyes, M. Abbarchi, and M. Gurioli, "Enhanced nanoscopy of individual cspbbr3 perovskite nanocrystals using dielectric sub-micrometric antennas," APL Mater. 8(2), 021109 (2020).

30) N. Dotti, F. Sarti, S. Bietti, A. Azarov, A. Kuznetsov, F. Biccari, A. Vinattieri, S. Sanguinetti, M. Abbarchi, and M. Gurioli, "Germanium-based quantum emitters towards a time-reordering entanglement scheme with degenerate exciton and biexciton states," Phys. Rev. B 91(20), 205316 (2015).

Chapter 5: AlGaAs deposition on top of Ge islands and optical characterization

In the two previous chapters, we studied the solid state dewetting process, from which we can develop nanoparticles that act as Mie resonators. In this chapter, the results of the integration of dewetted islands with III-V semiconductors are presented and discussed. We observe sharp and strong emission lines which most likely are attributed to impurities and defects inside the AlGaAs [1-3]. So far, this is one possible interpretation on this kind of system. More experiments would clarify the nature of the extracted light, which goes beyond the current thesis, but could lead to an unexplored emission possibilities. Such emissions were tested by micro-Photoluminescence set-up in the University of Florence and LENS lab as an extensive secondment, providing a detailed study of emission properties on individual islands covered with AlGaAs. However, experiments on several samples revealed peculiar bright light sources from AlGaAs directly deposited on the top of the SiO_2 substrate. Those emission centers are still under investigation to realize their optical nature. Time-resolved and autocorrelation measurements showed $g^{(2)} \sim 0.5$ revealing the quantum nature of the phenomena. Furthermore, an extensive study of the AlGaAs deposited on Ge islands didn't show any optical response.

However, before we characterize the samples by their optical response, we deposit by molecular beam epitaxy (MBE), III/V semiconductor materials on dewetted structures to study the coupling properties between the Mie resonances and

the light sources. The Ge thin film is deposited on the top of thick SiO_2/Si substrates and small crystalline Ge particles (50 - 500 nm) have been obtained by spontaneous and assisted solid state dewetting [4]. A 50 nm to 100 nm of $Al_{0.25}Ga_{0.75}As$ film between two 15 nm layers of $Al_{0.4}Ga_{0.6}As$ has been deposited in the MBE on the top of Ge islands resulting in Ge/AlGaAs core/shell Mie resonators [5, 6, 7]. The core-shell structure is shown in Fig.1. With green color is the core Ge islands on the top of which the sandwich structure of AlGaAs is deposited. In particular, yellow and light blue are 15 nm $Al_{0.4}Ga_{0.6}As$ which include the $Al_{0.25}Ga_{0.75}As$ active layer. The red shell represents the 5 nm GaAs capping layer. The small blue dots inside the AlGaAs structure, are Ge atoms or molecules coming from the Ge islands through diffusion during the annealing step. In Fig. 1, right panel, there is a representation of the band structure of the deposited material.

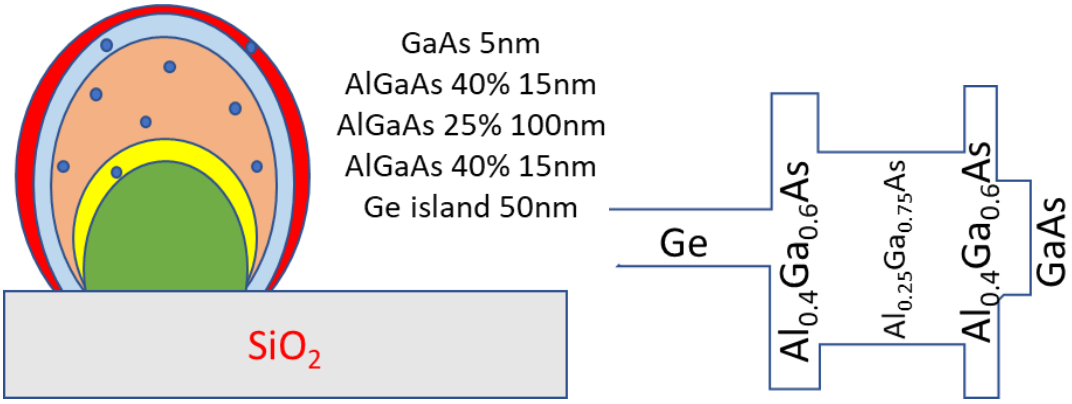

Figure 1: Left panel: Cartoon representation of epitaxial regrow on Ge islands. A sandwich was chosen to enclose the direct bandgap layer between two barriers. Right panel: Schematic representation of the band structure of the system. An active layer between two barriers.

The two $Al_{0.4}Ga_{0.6}As$ barriers are working as a cavity to confine carriers generated by the laser that is expected to recombine in the Ge impurity centers [1]. The incorporation of Ge atoms inside the AlGaAs matrix, as observed in Ref. 1-3,

can possibly produce intrinsic centers, capable of excitonic and multi-excitonic emission at liquid nitrogen temperatures, as well as single photon emission [1-3]. Also, by creating a high bandgap AlGaAs layer between the Ge island and the low bandgap AlGaAs layer we can reduce the absorption from Ge. By introducing high bandgap AlGaAs between the active layer and the GaAs capping layer, we try avoid non-radiative recombination in the structure's surface. Furthermore, we used 5 nm of GaAs capping layer on the top of all, working as a protective layer which means that the surface of AlGaAs is highly active when exposed to the atmosphere. The surface states can drain carriers from the structure below and reduce the recombination of carriers in the impurity center.

Four samples were annealed at standard annealing time of 2 hours and later deposited with AlGaAs, inside the same MBE chamber and in one experimental step (samples Δ3 - Δ6), and two samples with the pattern were just dewetted as references (samples Δ1 and Δ2) without any deposition. In Table 1 the samples that were fabricated are placed with all the necessary information. The experiment was monitored by RHEED and the morphology of the samples was characterized by Scanning electron microscopy.

Sample	Pattern	Annealing Temp. (°C)	$Al_{0.25}Ga_{0.75}As$ Thickness (nm)
Δ1	e-beam	600	-
Δ2	e-beam	650	-
Δ3	spont. dew.	600	50
Δ4	spont. dew.	600	100

Δ5	e-beam (positive)	650	100
Δ6	e-beam (negative)	680	100

Table 1: Sample description for the performed experiments.

For this set of experiments, we test the III-V semiconductor growth on lithographic and spontaneous dewetting conditions. We use nanopatterning with e-Beam Lithography [8] to fix arranged nanoparticle arrays with a certain size and island's density. Patterning is important to make sure the density is low and thus, there is no interaction between neighboring nano-islands, favoring the single photon emission observation. Furthermore, creating a pattern is easier to identify individual islands in nanoscale so we can study morphology and the optical characteristics of a marked island.

Within this chapter, photoluminescence results from two selected samples, samples Δ5 and Δ6 are shown (see Table 1). In both samples, there is patterning made by e-beam Lithography, one with positive and one with negative resist. Yhe growth and dewetting conditions were the same as shown in Table 1. We have been working on the low temperature optical characterization for these samples of AlGaAs deposition on dewetted islands.

5.1 Morphological Results

As it was already discussed in the previous chapter, the first step is to control the dewetting conditions and later arrive at a desirable configuration for each nanoparticle size. Before AlGaAs deposition, precise island's size in certain predefined positions should be ensured. We use either spontaneous dewetting

(sample Δ1 and Δ2) or dewetting assisted methods, such as e-beam lithography to achieve desirable results on nanoparticles' size (Δ3 and Δ4). The next step is to deposit III-V material on the top of arranged crystalline nanoparticles (samples Δ5 and Δ6). In Fig. 2, we can see a summary sketch of the experimental progress before the III-V deposition. A 30 nm thick thin film is deposited on top of 2 μm SiO_2/Si (001) substrate. The sample either with spontaneous or assisted dewetting develop Ge islands which later are used for epitaxial AlGaAs deposition.

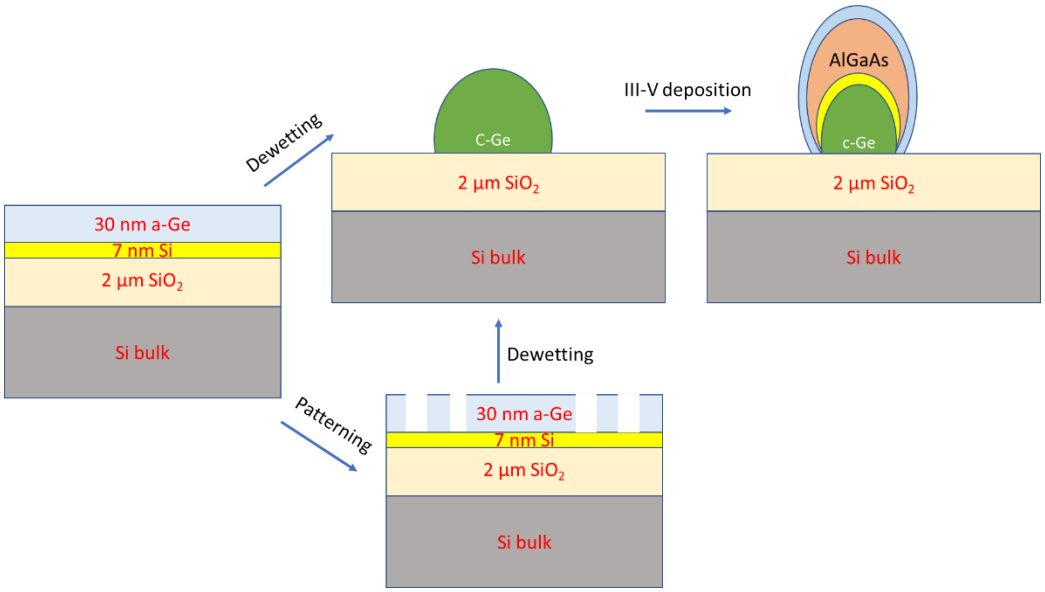

Figure 2: This cartoon summarizes the experimental progress of the samples that need to be processed before the deposition of semiconductor material. In the first image on the left, a thin a-Ge layer or a thin Si layer is deposited on top of 2 μm of SiO_2/Si substrate. In the following, the sample is processed in two possible ways. Either with spontaneous dewetting which occurs inside the ultra-high vacuum of an MBE system, or it passes through a lithographic step where the thin film is separated into patches of a certain size. After that, solid state dewetting occurs once again, but this time the islands are well organized. Finally, AlGaAs deposition occurs inside the same MBE system.

In order to keep well-defined nanoparticle size and island's density within the sample Δ1, we use e-beam lithography to develop a pattern with square patches from

500 nm^2 the smallest to 2500 nm^2 the biggest. The e-beam creates a chessboard of parallel vertical and perpendicular lines, leaving behind an array of patches with a certain distance between them [9]. This distance can differ from 200 nanometers to 2 micrometers. Each square patch, in a post-annealed sample, will lead to one island per patch in predefined distance between each island. As shown in Fig. 3 in the right panel, the patch is a square with predetermined dimensions where the island will appear after solid state dewetting [11]. This leads to a post annealed sample with predetermined island size and shapes all over the pattern area. By securing the pre-fixed island's position in this step, we keep islands away from each other to avoid any perturbation in the light extraction. Fig. 3 shows such a pattern in a post anneal sample. In Fig. 3, left panel, we show islands are well discrete between them, fabricated in the desired size for epitaxial growth.

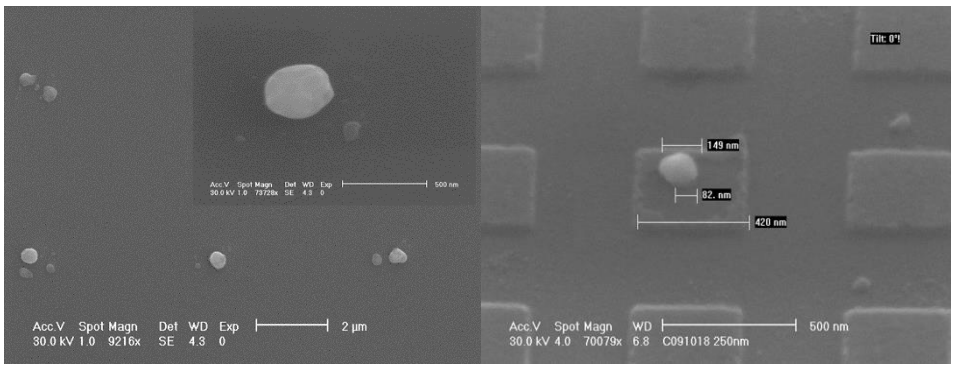

Figure 3: SEM picture of a set of 5 islands from a post annealed sample Δ1, patterned with e-beam lithography. The ordering between them is observed with a certain size and shape.

However, in sample Δ2, we try another array of patches which are bigger compared to the one in sample Δ1 and also round patterns (see Fig. 5). The patches sizes range from 1 μm^2 to 2.5 μm^2. We observed that patch size is getting too big, approximately 2.5 μm^2, and thus the dewetting on the patches' film leads to more than one island. In some cases, we can observe multiple of them such as Fig. 4 where the sample was patterned by e-beam Lithography creating different patch sizes. After

dewetting, we arrive in a patch with many islands and therefore the concept of single photon emitter is jeopardized.

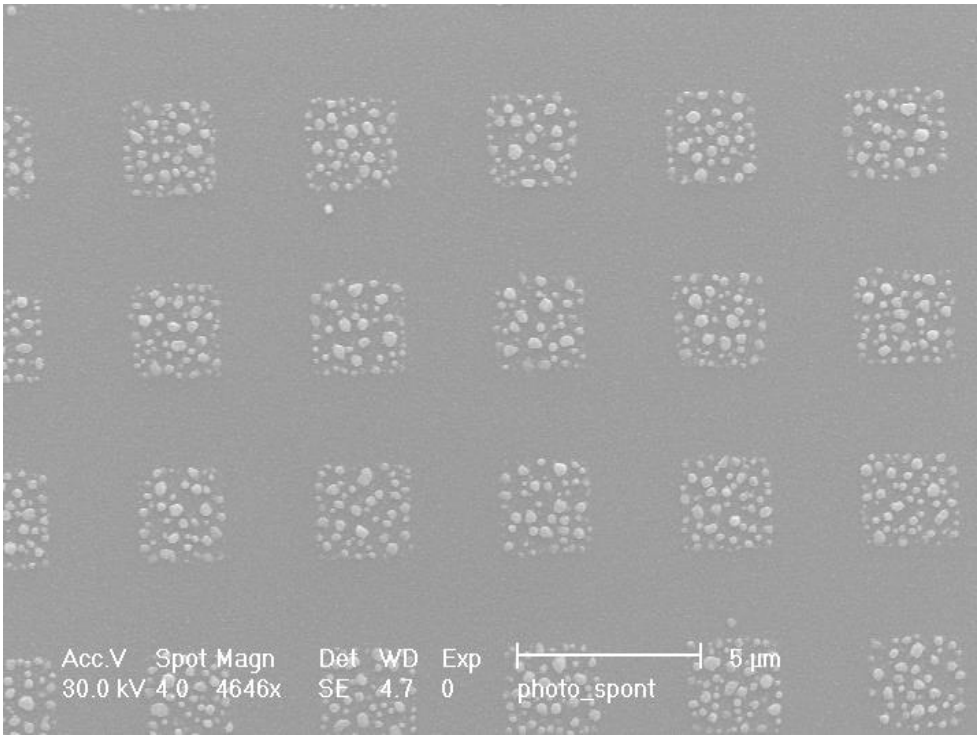

Figure 4: SEM picture in low magnification indicating the big patch patterns of sample Δ2 made by e-beam Lithography. Inside the patches, there are multiple islands after solid state dewetting. We can conclude that only smaller patches can develop a single island.

By assisted dewetting methods, we can extract valuable information for the nature of dewetting, and as discussed in the previous chapter, we can control the size and the conditions of the formed islands [11]. By testing several patterning configurations we manage to find the best conditions to create individual island positions away from its neighbor islands. For that reason, within the same sample we try to insert extra circular patterns with a small pillar in the middle. The diameter of the circular pattern is around 2 μm. On the top of the pillar, there is a portion of original thin film which after dewetting will become an island. The pillar in the middle has a diameter of around 100 nm. The middle pillar pattern has a certain

radius away from the rest of the film of 1 μm. In Fig. 5, we observe individual islands in well-defined positions on top of a cylinder surrounded by SiO_2. Each of these islands before the sample annealing belonged to a portion of the thin film with boundaries well defined, considered as a step in the thin film's original continuous formation. Those boundaries can be seen below the islands, where we can even observe traces of the original film. We also observe a parasitic smaller island very close to the bigger one, mostly appearing from the incomplete dewetting process [4]. The boundaries are more visible in Fig. 5, it is easy to detect where spontaneous dewetting stops and where the pattern starts. An individual island is confined into a circular patch with a rough environment of silicon oxide. Since the circular pattern is patterned with the same diameter and same height, the formed island is expected to be formed with the same dimensions.

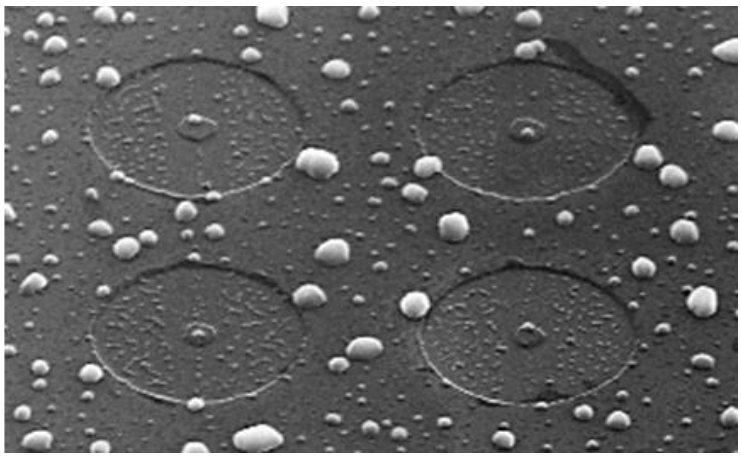

Figure 5: SEM picture of a circular pattern on sample Δ2 after the annealing step.

Investigating the samples Δ1 and Δ2 we determined the suitable conditions for the desirable island's size and thus, we proceeded with the deposition step. At first, we test the island formation with spontaneous dewetting and direct epitaxial re-grow of III-V materials. Our goal is to investigate whether or not we can develop Ge islands with a shell of AlGaAs on demand. We ensure that Ga and As atoms are

attaching the Ge islands and they do not spread among them on the top of SiO_2. Pictures from sample S3 confirm that a low amount of deposited AlGaAs D=50 nm permits the adatoms to attach to the Ge islands. In Fig. 6, we observe core-shell Ge nanoislands covered with AlGaAs. The deposition seems inhomogeneous on top of the islands. Inserted High-Resolution SEM image in Fig. 6 reveals the facets formed from the deposited material. However, keeping the amount of AlGaAs only 50 nm we observe some parasitic growth between the nano-islands.

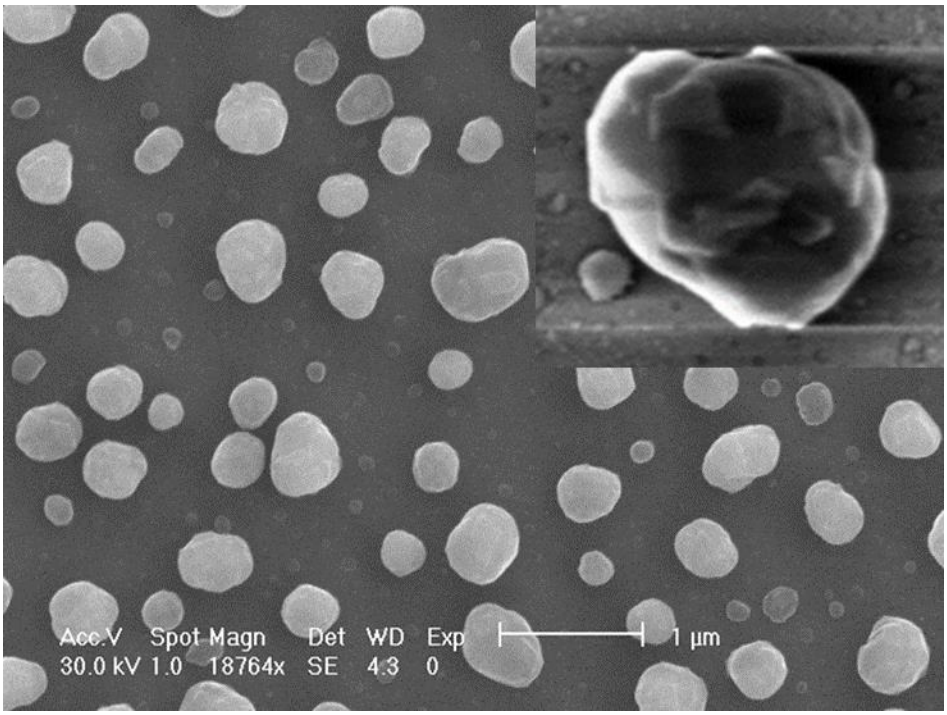

Figure 6: SEM picture of deposited AlGaAs on top of Ge islands of sample Δ3. We can see that we do not observe AlGaAs in the surroundings because of the low amount of deposited material. In the picture included, we see a closer look with an HR-SEM, the post deposited Ge island, with flakes of deposited AlGaAs on the top.

Increasing the amount of AlGaAs in sample Δ4 at 100 nm, we observe differences compared to sample Δ3. In figure 7, we see an SEM picture from the post annealed sample Δ4 with epitaxial growth of 100 nm AlGaAs on top of the Ge nano-islands. We can see that AlGaAs is not only grown on top of Ge islands but also on

the top of very small ones and also between the islands. Fig. 7 inserted picture, is a typical example of AlGaAs deposition on top of Ge islands where AlGaAs look deposited everywhere in the surroundings. However, the faceting shape after deposition is well defined [12].

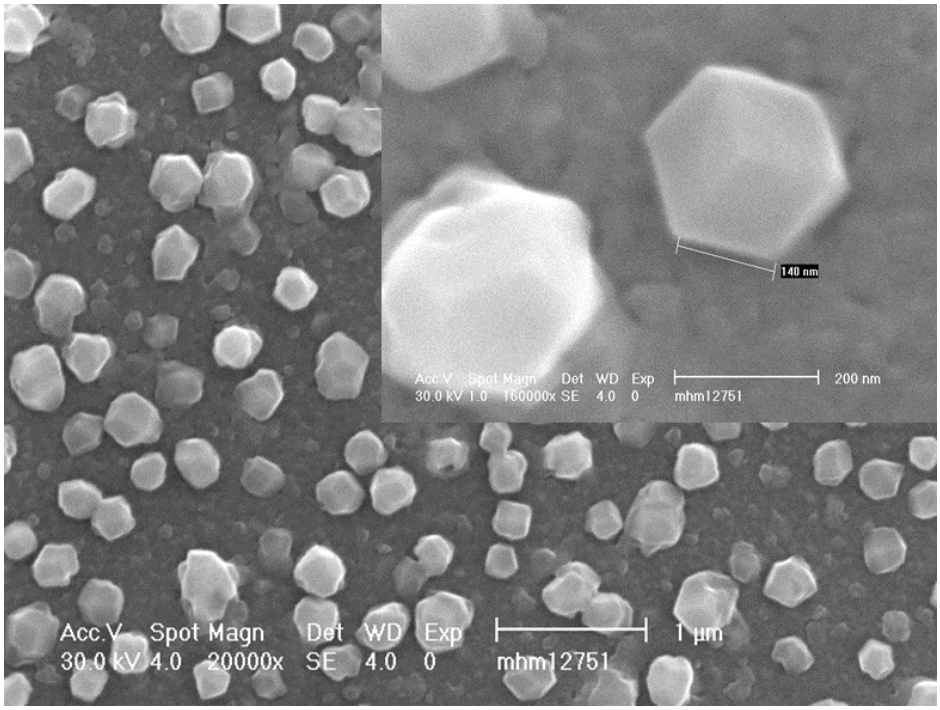

Figure 7: SEM picture of spontaneous dewetted sample Δ4 with AlGaAs on top. Inside the picture, we can see a high magnification of an island with well-defined shape and faceting.

So far, in the samples Δ1-Δ4 were studied the patterning and the deposition condition to proceed to the deposition step. In samples Δ5-Δ6 we test the deposition of AlGaAs following the observations obtained in previous samples. Micro-photoluminescence experiments were performed on samples Δ5 and Δ6 where AlGaAs is present. Both samples were patterned in order to obtain island isolation and therefore to make sure there is no match of their optical response and secondly because patterns are easy to spot and re-find this position easily. It is important to create a mark in order to test the emission properties of the marked areas and return

to each individual emitter whenever needed [13]. By patterning the sample surface, it is easy to create a cheeseboard of numbers and letters which helps us to identify the direction and the position of the examined individual island. In Fig. 8, we can see 3 SEM pictures from sample Δ5, from lower to higher magnification of a patterned sample. The small red lens on the picture represents the pattern and the spot where we focus our collimation lens to perform the photoluminescence experiments. As we can see, the sample has 16 patterns with square or circular patches for the development of the islands. Each pattern has 7 x 7 circular patches of different sizes. In the end, there is an island standing on the top of a column. The island size ranges from 100 nm to 300 nm depending on the size of the pattern. Moreover, the radius of the circular pattern is 1 μm and in the case of square pattern, the distance between the islands ranges between 0.5 μm to 5 μm.

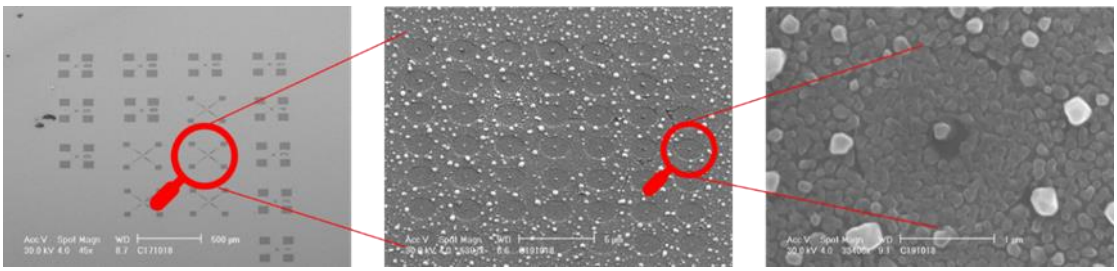

Figure 8: SEM pictures from lower to higher magnification on a patterned sample with circular and square patches. From left to right the cartoon lenses show the focus area of the next image. Finally, we see the island on top of a column which is also the focus area of the laser after collimation from the objective lens.

5.2 Micro-Photoluminescence Results

PL measurements performed at low temperature (T=10 K) with the samples placed in a cold-finger helium flow cryostat. A frequency-doubled Nd-yttrium aluminum garnet laser with λ_{exc}= 532 nm was used for continuous-wave measurements [14]. Typical micro-PL spectra of sample Δ5, at 50 mW excitation

power, is reported in Fig. 9. Spectra from each one circular pattern from two columns were obtained. The main contribution broadband is located at 1.5 eV peak position, which is speculated to be attributed to the emission from the GaAs capping layer on the top of the structure as shown in Fig. 1. A less intense contribution peaks are spotted in higher energy around 1.8 eV which can be attributed to emission from the AlGaAs or other impurities in the AlGaAs matrix [15].

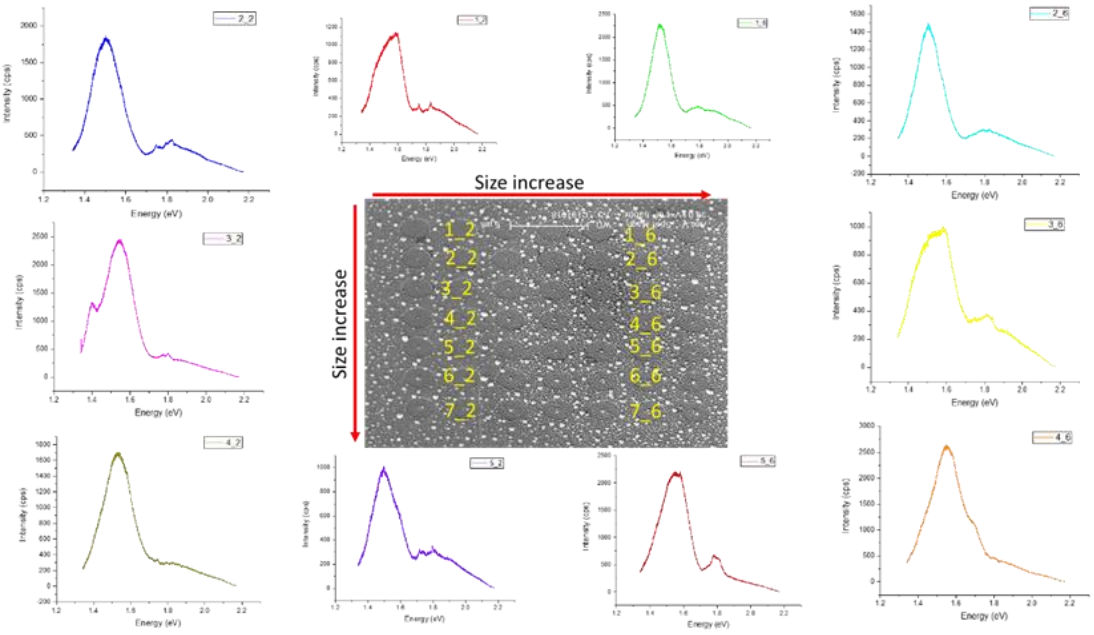

Figure 9: Several micro-PL spectra of individual islands from the SEM picture in the middle. The size is increasing from left to right and from top to bottom.

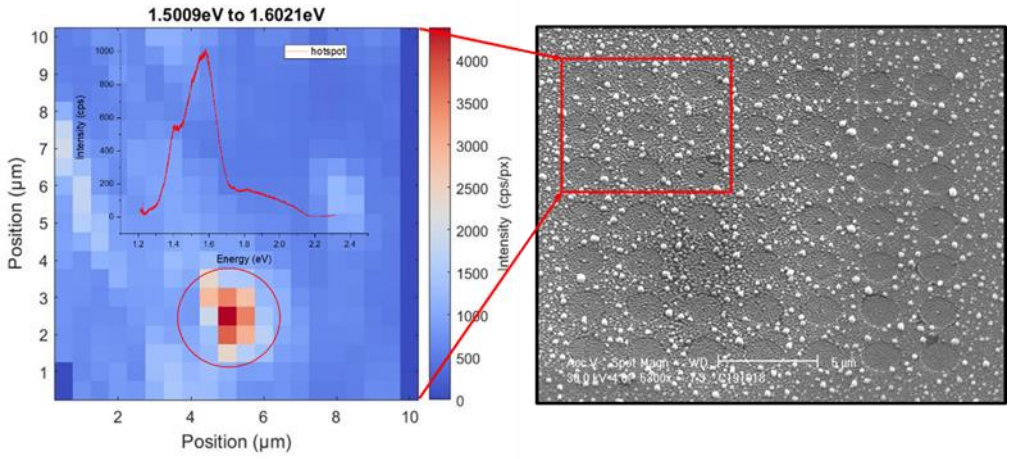

Figure 10: micro – PL map of the patterned sample corresponding to the area covered with the red square. The strongest light emission is coming from the middle bottom position of the dictated map, which means that only one out of the 9 patches is enough intense. The scanned area is 10 x10 μm2, the step was set at 0.5 μm, and the integration time at 1sec.

In order to investigate more precisely the optical response of sample Δ5, a series of maps were done to find strong emitting centers. However, none of the individual islands present strong narrow emitting lines, since the more intense peak is very broad and is coming only from one spot inside the pattern as shown in Fig. 10 map. The rest of the area is completely out of any photoluminescence signal.

In the following, we perform a similar study for the sample Δ6. The pattern is fixed to develop a post anneal island array of several islands with a size of 200 nm as shown in Fig. 11. However, the sample Δ6 presents a reverse preparation process for lithography [16]. The red line represents the profile scan of the sample. In the middle, identical size islands rest on top of SiO_2 substrate. In the 4 corners of the picture, there are indicators controlling the position of the central pattern. Around the pattern, there is an area without any Ge original film and therefore, no Ge islands should appear after dewetting.

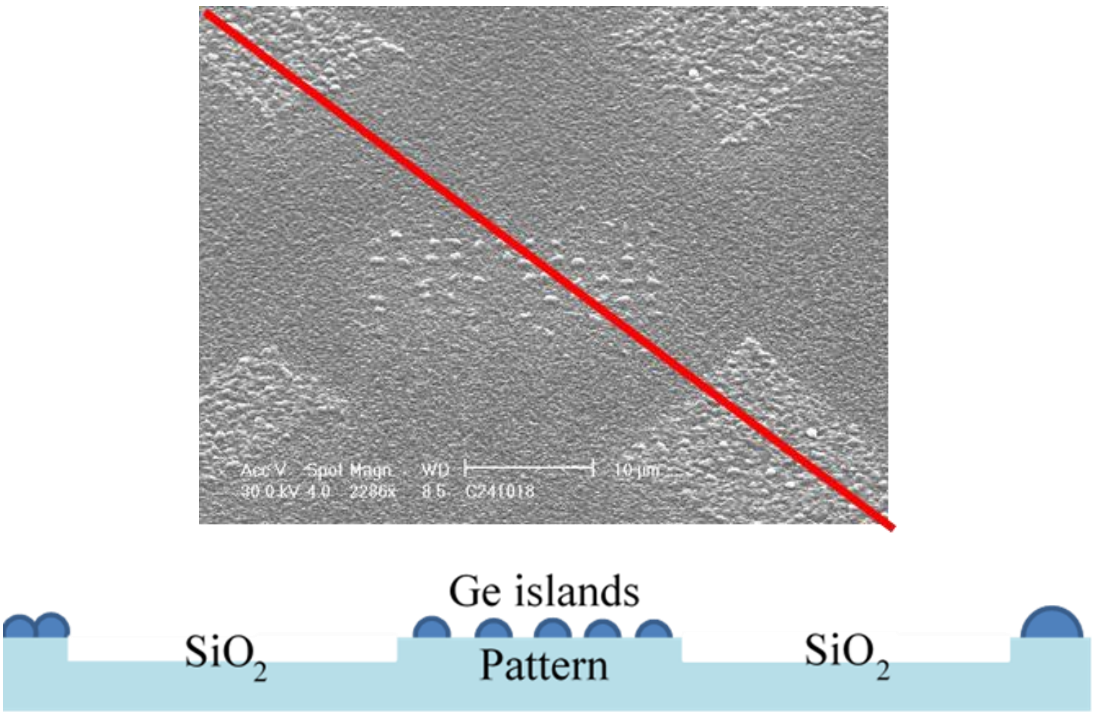

Figure 11: SEM picture of a patterned patch. The red line represents the profile of the cartoon below the SEM image.

In Fig. 12, we compare the spectra of several random spots inside the pattern named (Pattern_spot) and one random spot outside of the pattern (NoGe Spot), in the 'no Ge' area of the sample as shown in the SEM picture inside the Fig. 12. The measurements were performed in the same excitation power conditions at P_{in}=400 μW and the same focus of the objective lens. The emission intensity appears to be much higher compared to the ones observed in the patterned area. The unexpected results show that the emission from the area outside the pattern is much more intense than the one observed inside the patterned area, where the individual Ge islands are. In fact, an intense broad peak appears at 1.9 eV and less intense ones at 1.75 eV and 1.8 eV.

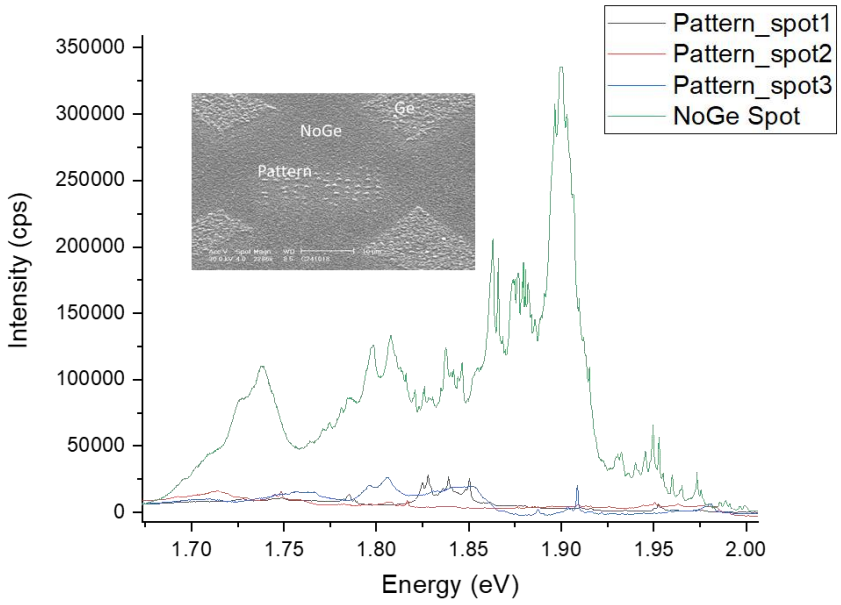

Figure 12: micro-PL spectra of the patterned area at a direct comparison with the spectra taken outside of the patterned area.

After observing strong emitting properties of the 'no Ge' area, it is necessary to find more emitting points and study them deeper. In Figure 13, a strong emitting point is presented adjusting the excitation power on a lower scale. We can see that even with much less excitation power, which is at P_{in}=3.6 μW, the emission intensity is very strong with a narrow emission peak, located at 1.85 eV energy. Several emission spots were found during scan with the micro - PL set up to confirm the abundance of the investigated strong emission.

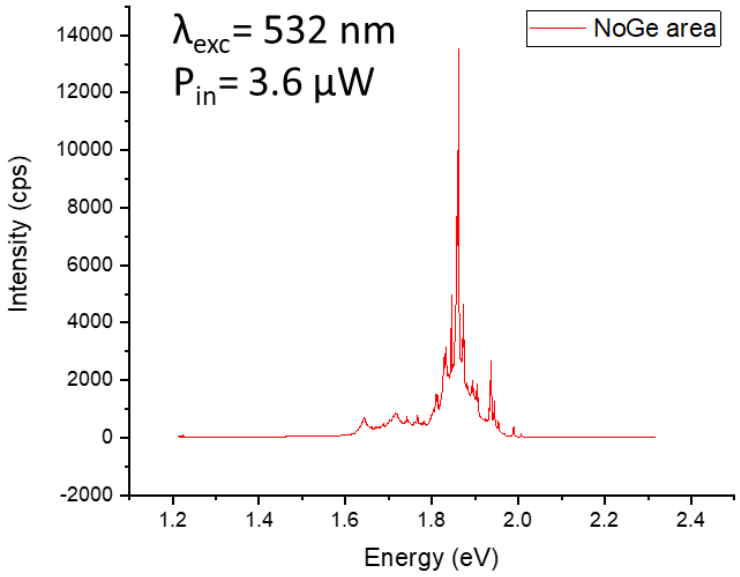

Figure 13: micro-PL spectra from an emission point on top of an island in the 'no Ge' area.

To investigate the nature of this emission point we performed power dependence measurements to understand if it is possible to attribute this emission to excitation recombination. To perform these experiments we needed to select a strong emitting spot with a narrow line and measure at each excitation power the emission line. In Fig. 14, the experimental result of power dependence is presented. The emission line located at 1.78 eV is measured in very low excitation power ranging from 5 µW until 50 µW. At this point, we have shown that it is possible to find and study strong and sharp emission lines but still those lines need to be examined further. The attribution of the emission lines can be light source from impurities to defects coming from the preparation process or some other factors which goes out of control of the experimental set up. It is true that several defects from atoms to molecules, can be found in the matrix and reveal different light properties.

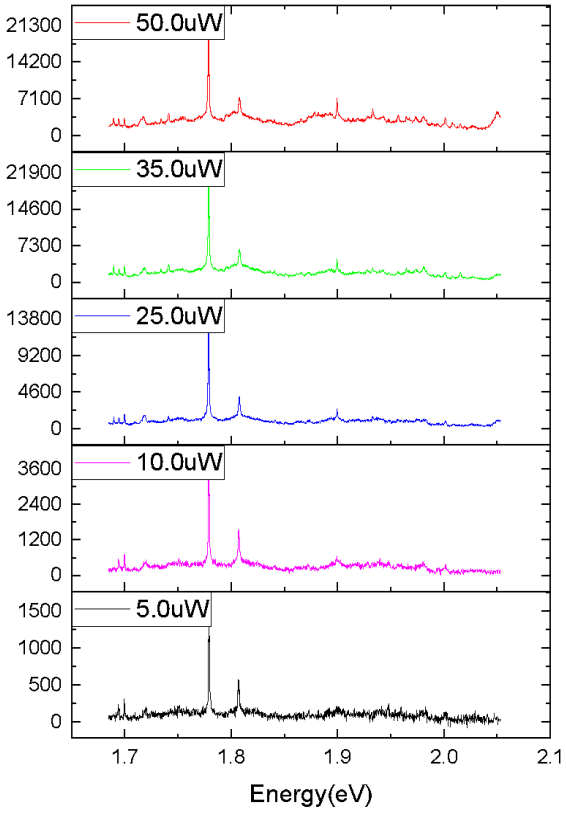

Figure 14: Power dependence measurements on excite and bi-exciton emission lines.

In the following, in Fig. 15 the maximum peak analysis of each graph is presented to confirm the exciton and bi-exciton nature of the emission lines observed in the previous power dependence measurement experiments [3].

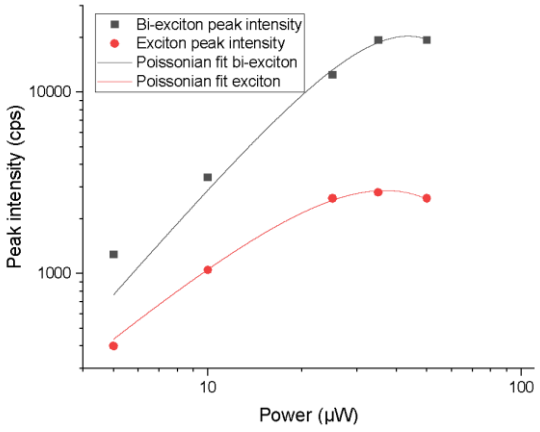

Figure 15: Power intensity vs power plot of the power dependence measurements of the previous emission spectra.

The observed peak lines present narrow emission lines of the emitters within the sample. In figure 16, the studied emission line is excited with P_{in}=6 μW, and the FWHM we observed was around 700 μW.

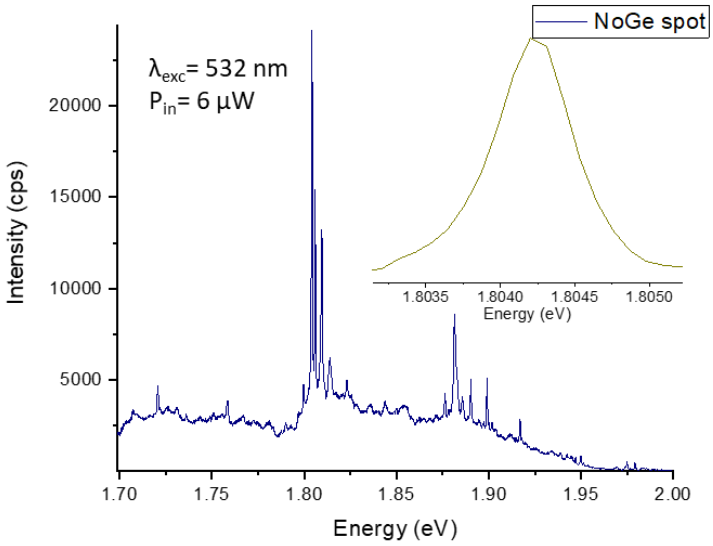

Figure 16: Narrow emission lines from a strong emitted spot in the no Ge area. The FWHM is shown in the inserted picture.

Finally, we checked if the observed center is capable of single photon emission by time-resolved and autocorrelation measurements. For this purpose, we need to switch the excitation laser from a continuous to a pulsed one [14]. In Fig. 17, the left panel is presented with a narrow single line excited with a blue laser at 400 nm. The excitation power is P_{in}= 25 μW and the objective is focused to optimize the maxim intensity of the investigated emission line. The time resolved measurements reveal a decay time of around 1,5 ns which is in accordance with the decay time of the exciton recombination.

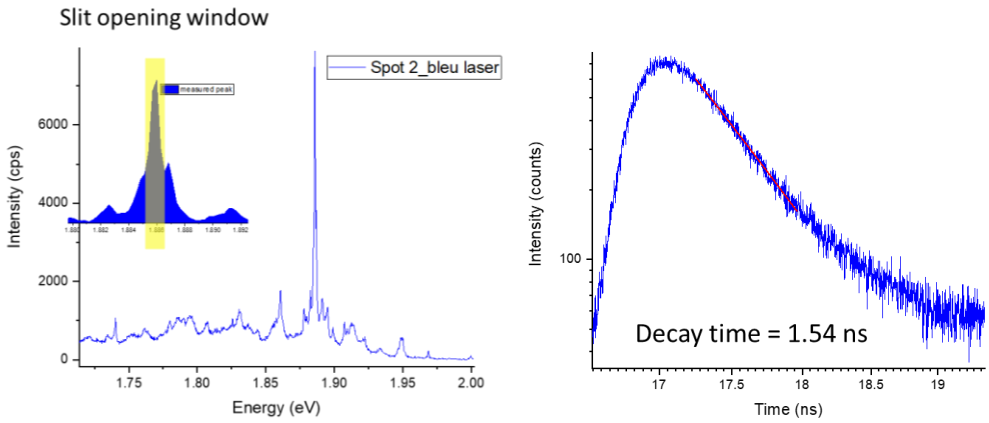

Figure 17: In the left panel the emission spectra of individual islands with blue laser excitation. The respective time resolved measurements is shown on the right panel.

Autocorrelation measurements were performed for the same emission peak in the previous figure with the same power used for the time resolved measurements. The experiment lasted for 3 hours since the oscillations from the He flow was large and the slit opening was too small to stay centered in the emission line. The center of the emission was often corrected to make sure that we measure the right emission point. Despite these limitations and the background contribution of the surroundings, to the measurements, there is a strong indication of an existing single photon source. The $g^2(0)$ measurement is close to 0.5, which is the limit to provide some evidence of a single photon source. However, the result was affected by the noise introduced by the background contribution, so that a lower value is expected. In the following figure (fig. 18), the $g^2(0)$ experimental results are presented.

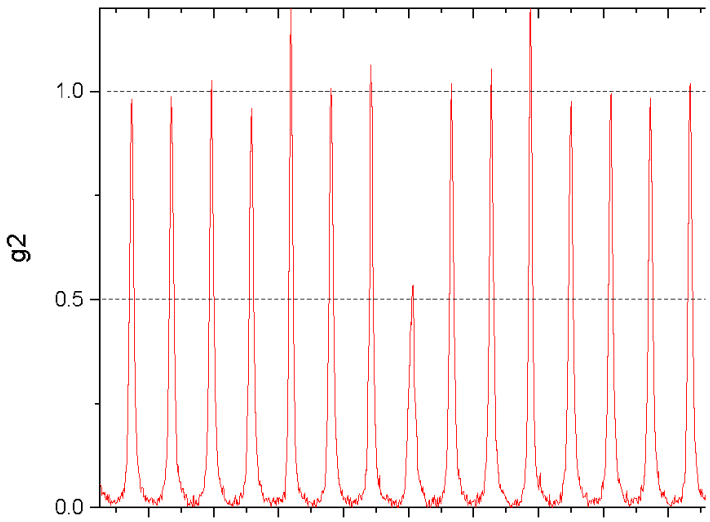

Figure 18: Autocorrelation measurements of the spectra captures in figure 17. The result of $g^2(0)= 0.5$ is an indication of single photon source behavior of this emitted island.

Discussion

AlGaAs deposition morphology and low temperature optical characterization of AlGaAs deposition on dewetted islands were investigated in this chapter. SEM image collected after the deposition of III/V materials shows that the deposited AlGaAs seems to spread over the entire surface of the sample (sample Δ3-Δ6), in regions where Ge islands have been formed, but also in regions where the amorphous Ge layer has been previously removed leaving exposed the underlying SiO_2 layer (sample Δ5 and Δ6). The latter samples were patterned with an e-beam lithographic process to introduce individual islands. The only difference between the sample S5 and sample S6 is the preparation for the lithographic step. In sample Δ5 a positive resist was deposited and later the Ge film was etched, while instead in sample Δ6, the negative resist was deposited to protect the pattern and the rest of the Ge thin film was removed. For more information on this process see reference number [16]. The result seems to come from an unexpected source that could be related to the

unconventional deposition of AlGaAs. The photoluminescence characterization shows that the optical response is coming from an area where the Ge thin film had removed previously during the preparation of the sample for the lithographic process. In fact, during the deposition of III/V materials, the Al has been deposited before the opening of the As shutter. A possible interpretation is that Aluminum forms Al_2O_3 islands reacting with the exposed SiO_2 ("No Ge" area), acting as crystalline seeds for the AlGaAs regrow [17]. Micro-photoluminescence (PL) at T = 10 K in the dewetted Ge island regions, showed no signal or very weak signal related to AlGaAs, probably due to a high defect concentration. Surprisingly, we observed sharp emission lines in the "No Ge" area. The sharp peaks are characterized by a typical FWHM of 0.5 meV, and the measurement of the normalized second-order autocorrelation function, $g^2(\tau)$, gives a value of 0.5 at zero delay time, indicating the single-photon emitter nature of the collected light. An explanation of this result is still unclear and more experiments need to be done, but the emission is more likely to be originated from luminescent defects in AlGaAs, for instance, Ge, Si, O or more. Further investigation on growing conditions are expected to confirm this picture, but also to obtain single photon emission from AlGaAs deposited on the dewetted structures. The current chapter can be used as a guide for future experiments in order to explore more the idea of Ge droplets which work as nano-resonators or any kind of resonators to amplify the extracted light for single photon purposes. Studies have shown that impurities work [1] and they work very well under certain conditions [2-3]. However, the starting point is here and lot of interesting properties can be found as soon as we have more details and more experiments in this direction.

5.3 Bibliography

1) F. Sarti, G. Muñoz Matutano, D. Bauer, N. Dotti, S. Bietti, G. Isella, A. Vinattieri, S. Sanguinetti, and M. Gurioli,'Multiexciton complex from extrinsic centers in AlGaAs epilayers on Ge and Si substrates', Journal of Applied Physics 114, 224314 (2013).
2) Nicola Dotti, Francesco Sarti, Sergio Bietti, Alexander Azarov, Andrej Kuznetsov, Francesco Biccari, Anna Vinattieri, Stefano Sanguinetti, Marco Abbarchi, and Massimo Gurioli,'Germanium-based quantum emitters towards a time-reordering entanglement scheme with degenerate exciton and biexciton states', PHYSICAL REVIEW B 91, 205316 (2015).
3) S. Minari, L. Cavigli, F. Sarti, M. Abbarchi, N. Accanto, G. Mu~noz Matutano, S. Bietti, S. Sanguinetti, A. Vinattieri, and M. Gurioli,'Single photon emission from impurity centers in AlGaAs epilayers on Ge and Si substrates', APPLIED PHYSICS LETTERS 101, 172105 (2012).
4) Dimosthenis Toliopoulos, Alexey Fedorov, Sergio Bietti, Monica Bollani, Shiro Tsukamoto, Emiliano Bonera, Marco Abbarchi, Andrea Ballabio, Giovanni Isella, Stefano Sanguinetti,'Solid-state dewetting of amorphous Ge thin film SiO2/Si (001)', Nanomaterials, 10, 2542, (2020).
5) Yuta Tsuchimoto, Taka-aki Yano, Tomohiro Hayashi, and Masahiko Hara, 'Fano resonant all-dielectric core/shell nanoparticles with ultrahigh scattering directionality in the visible region', OPTICS EXPRESS 14451, (2016).
6) ANDREY B. EVLYUKHIN, KHACHATUR V. NERKARARYAN AND SERGEY I. BOZHEVOLNYI, 'Core-shell particles as efficient broadband absorbers in infrared optical range', OPTICS EXPRESS 17474, Vol. 27, No. 13, (2019).
7) RUNMIN LI, XIN ZHOU, MINGCHENG PANMAI, JIN XIANG, HAIYING LIU, MIN OUYANG, HAIHUA FAN, QIAOFENG DAI, AND ZHONGCHAO WEI, 'Broadband zero backward scattering by all-dielectric core-shell nanoparticles', OPTICS EXPRESS 28891, Vol. 26, No. 22, (2018).
8) I. Berbezier, M. Aouassa, A. Ronda, L. Favre, M. Bollani et al, 'Ordered arrays of Si and Ge nanocrystals via dewetting of pre-patterned thin films', J. Appl. Phys., 2013 113, 064908.

9) I. Berbezier, M. Aouassa, A. Ronda, L. Favre, M. Bollani et al, ‘Ordered arrays of Si and Ge nanocrystals via dewetting of pre-patterned thin films’, J. Appl. Phys., 2013 113, 064908.
10) A. A. Shklyaev and A. V. Latyshev, ‘Dewetting behavior of Ge layers on SiO2 under annealing’, Scientific Reports, 2020, 10, 13759.
11) M. Aouassa, I. Berbezier, L. Favre, A. Ronda, M. Bollani, R. Sordan, A. Delobbe, and P. Sudraud, “Design of free patterns of nanocrystals with ad hoc features via templated dewetting,” Appl. Phys. Lett. 101(1), 013117 (2012).
12) F. Leroy, F. Cheynis, T. Passanante, and P. Muller, ’Influence of facets on solid state dewetting mechanisms: Comparison between Ge and Si on SiO2’, PHYSICAL REVIEW B 88, 035306 (2013).
13) D. Toliopoulos, M. Khoury, M. Bouabdellaoui, N. Granchi, J.-B. Claude, A. Benali, I. Berbezier, D. Hannani, A. Ronda, J. Wenger, M. Bollani, M. Guriolli, S. Sanguinetti, F. Intonti, and M. Abbarchi, ‘Fabrication of spectrally sharp Si-based dielectric resonators: combining etaloning with Mie resonances’, Optics Express, Vol. 28, No. 25, 2020.
14) Andrea Ristori, Travis Hamilton, Dimosthenis Toliopoulos, Marco Felici, Giorgio Pettinari, Stefano Sanguinetti, Massimo Gurioli, Hooman Mohseni, Francesco Biccari, ‘Photonic jet writing of quantum dots self-aligned to dielectric antennas’, Adv. Mat. Submitted.
15) Mayer, B., Rudolph, D., Schnell, J. et al. ‘Lasing from individual GaAs-AlGaAs core-shell nanowires up to room temperature’, Nat Commun 4, 2931 (2013).
16) M. Bollani, M. Salvalaglio, A. Benali, M. Bouabdellaoui, M. Naffouti, M. Lodari, S. Di Corato, A. Fedorov, A. Voigt, I. Fraj, L. Favre, J. B. Claude, D. Grosso, G. Nicotra, A. Mio, A. Ronda, I. Berbezier, and M. Abbarchi, “Templated dewetting of single-crystal, ultra-long nano-wires and on-chip silicon circuits,” Nat. Commun. 10(1), 5632 (2019).
17) Michiel de Goede, Lantian Chang, Meindert Dijkstra, Raquel Obregón, Javier Ramón-Azcón, Elena Martínez, Laura Padilla, Jaume Adan, Francesc Mitjans, and Sonia M. García-Blanco, ‘Al2O3 Microresonators for Passive and Active Sensing Applications’, Advanced Photonics (2018).

Chapter 6: Conclusions

The aim of this Ph.D activity was to develop single photon sources on Si exploiting light matter interaction with a nano-photonic structure for improving the emission efficiency. The path we aimed to follow was to embed individual localized impurities in a semiconductor nanocrystal with suitable size to act as a dielectric Mie resonator, also denominated as dielectric antennas. The main body of this project is then focused on the fabrication and optimization of the optical properties of the Ge Mie resonators which served as proper seed for epitaxial growth of III-V with quantum emitters. Initial steps have been made in order to study the light matter interaction between the localized impurities and the dielectric Mie resonators.

Solid state dewetting was used to fabricate Ge nanocrystals of different sub-micrometric size. The main novelty of our approach was the use of a thin film of a-Ge, instead of c-Ge, for the solid state dewetting, which turned out as an alternative path with interesting film's kinetics. The formed nano-islands are crystalline, with a density and a size that are controlled by the annealing temperature, time, and temperature ramp. Surface tension plays a role only in determining the final shape of the nano-islands, which show a compact, 3D shape driven by surface energy minimization. We assessed that two temperature activated mass transfers are relevant during the process. The first, which dominates at intermediate temperatures (T> 550 °C), is the diffusion of Ge atoms from the a-Ge to the crystalline nuclei. The second, which determines the island size distribution at high temperature, is the Ostwald ripening.

For photonic applications, it is demanding to get the appropriate size of the Mie antenna. We defined a solid state dewetting protocol for obtaining the proper

size for the epitaxial regrowth, thus to match with the light matter coupling wavelength region. In addition, we also exploited assisted methods with lithographic patterns, to optimize the density of dielectric antennas.

Epitaxial growth of AlGaAs on the Ge seeds was performed to create an III-V layer on which to incorporate the quantum emitters. We performed a systematic study of the amount of deposited material and its emission energy, in order to find a good match between the wavelength of the light emitter and the Mie resonance, as well as to assess the quality of the fabricated nano-antennas. We finally aimed to include individual color centers as quantum emitters in the AlGaAs layer. The target impurity was Ge, due to the natural and unavoidable incorporation of Ge in the AlGaAs from the seeds. Indeed, it was known from the literature that these extrinsic centers are capable of excitonic and multi-excitonic emission at nitrogen temperatures, as well as single photon emission.

Monocrystalline islands will act both as seeds for the epitaxial regrowth as well as sub-wavelength antennas, and therefore extensive study of the scattering profile of individual islands was done at University of Marseille as a secondment within the 4photon network. The so-called Mie resonators present a scattering spectrum measured by dark field optical microscope. The bright colors seen with dark field microscopy originate from the Mie resonances that are formed within each particle, depending on its size and shape. We showed that the use of a thick SiO_2 layer below the nanoantennas, which acts as an etalon, can be used to enhance the optical response. Dark-field images reveal a net colorization which tends to the red when increasing particle size. The corresponding scattering spectra confirm this tendency, showing several sharp bands that increase in number at long wavelengths for larger islands. These resonances share a similar spectral position and spacing between them.

The integration of quantum emitters was the final challenge. As could happen in any scientific project, the initial idea failed and unexpected results were found. We tested the presence of optically active impurity centers in our samples were tested by micro-Photoluminescence set-up in the University of Florence and LENS lab during an extensive secondment. This activity provided an extensive study of the AlGaAs deposited Ge islands, which unfortunately didn't show any quantum emitter and the problem is still under discussion and certainly needs further investigations. At the same time, experiments on several samples revealed bright light sources from AlGaAs directly deposited on the top of initially aluminized surface of the SiO_2 substrate. Time resolved and autocorrelation measurements showed g (2) ~ 0.5 revealing the quantum nature of the emission.

Those emission centers are under investigation to understand their nature and the possibility to control them. Still, we believe that they can be an unexpected and yet promising way to integrate quantum emitters on oxide layers on the top of any Si photonic structures, thus paving the route for many interesting developments.

Appendix A: Faceting shape of Si nanoislands

Analysis of morphological characterization of faceting shape of Si islands from spontaneous dewetting was performed with an ultra-thin tip of AFM. Those experiments were very important for this thesis in order to understand whether the faceting shape of the formed island, acting as Mie resonators, are similar to the ones observed in the literature [a]. In Fig. 1 a 10 x10 μm area from a dewetted sample is studied from a Si sample after solid state dewetting at T= 750 ºC inside the MBE chamber of the set-up described in Chapter 3. The annealing time was 2 hours and the morphology was monitored by RHEED in situ real time.

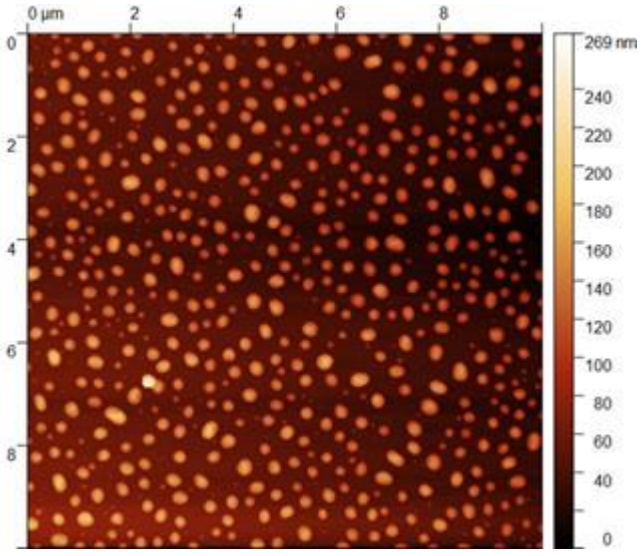

Figure 1: Si islands characterized by AFM on a 10x10 μm area.

Results show that after solid state dewetting occurred we find out that the minimized energy facets {113}, were exposed. Fig. 2, is shown AFM

characterization with an ultra-sharp tip, of a 0.5 μm x 0.5 μm area, in different angles exposing the faceting profile of the highlighted island.

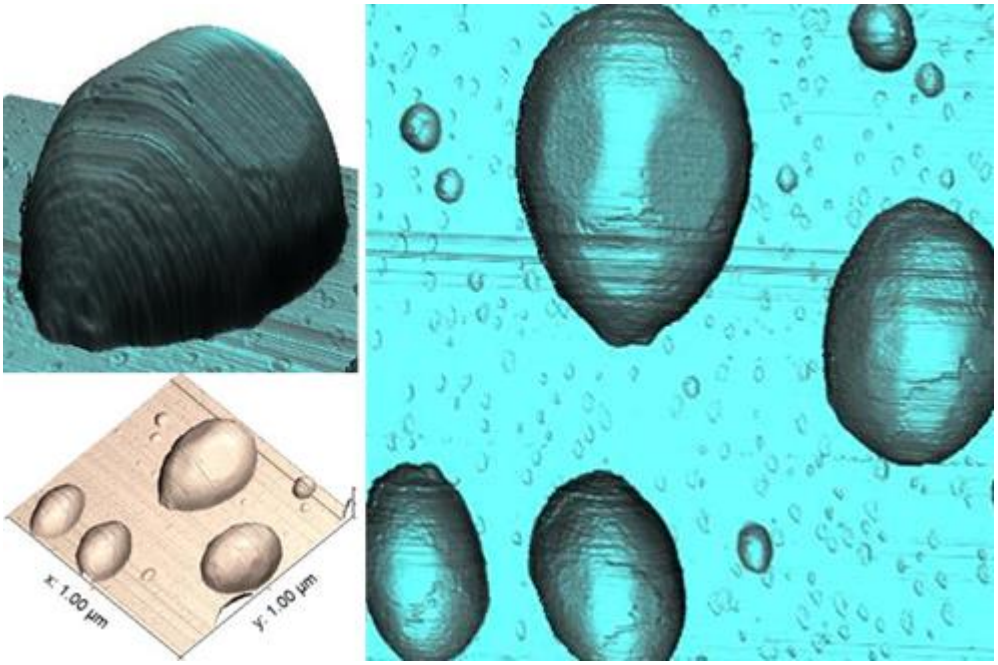

Figure 2: Ultra-thin tip AFM measurement of a 1μm x 1μm area. The studied island is shown in different angles to spot the faceting shape.

The contact angle between (001) surface and the larger linear line it was found 41º which corresponds to {113} facet. Those results are coming in agreement with reference [b] where the dominant exposed facet is {113}. However, comparing islands coming from different experimental conditions, such as dewetting and crystal growth [a-e] we observe differences in the dominant exposed facets of SiGe islands. In reference [a] the SEM characterization showed that the faceting shape of the islands is covered with facets, such as {501}, {311}, {23 15 3} and {111}, which are usually observed on the sides of large Ge and Si islands. Moreover, it is possible to find a lot of small facets but not a dominant one on crystalline islands. In references [d, e] the dominant observed facets correspond to {105} coming in disagreement with the previous reported island's shape. The round shape of the

islands is not crucial for the selection of exposed facets, because as we see in the reference [d] and [e], the pyramidal shape has the same exposed facets comparing one of the round-shaped islands. According to this work though, the preferable shape and exposed facets are round shapes and {113} faceting observed globally in the whole sample. However, substrate and dewetting conditions should play an important role in this mechanism. In the current thesis, we discuss those differences supported by kinetic theory. Stabilized facets according to temperature could be a stable or metastable system and according to ref [f-g] temperature is playing a dominant role in the dominant exposed facet. Our results present perfect agreement with those references, where the {113} facet is the dominant one, below a certain temperature.

Bibliography

a) A.A. Shklyaeva, A.E. Budazhapova, 'Submicron- and micron-sized SiGe island formation on Si (100) by dewetting', Thin Solid Films 642 (2017) 345–351.

b) D. Dutartre, A. Talbot and N. Loubet, 'Facet Propagation in Si and SiGe Epitaxy or Etching', ECS Transactions, 3 (7) 473-487 (2006).

c) P P Zhang, B Yang, P P Rugheimer, M M Roberts, D E Savage, Feng Liu and M G Lagally, 'Influence of germanium on thermal dewetting and agglomeration of the silicon template layer in thin silicon-on-insulator', J. Phys. D: Appl. Phys. 42 (2009) 175309 (6pp).

d) Armando Rastelli, Hans von Kaanel, 'Island formation and faceting in the SiGe/Si (001) system', Surface Science 532–535 (2003) 769–773.

e) Moritz Brehm, Herbert Lichtenberger, Thomas Fromherz, Gunther Springholz, 'Ultra-steep side facets in multi-faceted SiGe/Si (001) Stranski-Krastanow islands', Nanoscale Research Letters 2011, 6:70

f) F. Cheynis,a) F. Leroy, T. Passanante, and P. Muller,'Agglomeration dynamics of germanium islands on a silicon oxide substrate: A grazing incidence small-angle x-ray scattering study', APPLIED PHYSICS LETTERS 102, 161603 (2013).

g) F. Leroy, F. Cheynis, T. Passanante, and P. Muller, 'Influence of facets on solid state dewetting mechanisms: Comparison between Ge and Si on SiO2', PHYSICAL REVIEW B 88, 035306 (2013).

List of publications in journals and International Conferences

- Dimosthenis Toliopoulos, Alexey Fedorov, Sergio Bietti, Monica Bollani, Shiro Tsukamoto, Emiliano Bonera, Marco Abbarchi, Andrea Ballabio, Giovanni Isella, Stefano Sanguinetti,'Solid-state dewetting of amorphous Ge thin film SiO2/Si (001)', Nanomaterials 2020, 10, 2542.

- D. Toliopoulos, M. Khoury, M. Bouabdellaoui, N. Granchi, J.-B. Claude, A. Benali, I. Berbezier, D. Hannani, A. Ronda, J. Wenger, M. Bollani, M. Guriolli, S. Sanguinetti, F. Intonti, AND M. Abbarchi, 'Fabrication of spectrally sharp Si-based dielectric resonators: combining etaloning with Mie resonances', Optics Express, Vol. 28, No. 25, 2020.

- Andrea Ristori, Travis Hamilton, Dimosthenis Toliopoulos, Marco Felici, Giorgio Pettinari, Stefano Sanguinetti, Massimo Gurioli, Hooman Mohseni, Francesco Biccari, 'Photonic jet writing of quantum dots self-aligned to dielectric antennas', submitted to Advanced Materials, 2020.

- Dimosthenis Toliopoulos, Andrea Ballabio, Alexey Fedorov, Sergio Bietti, Andrea Barzaghi, Stefano Di Corato, Monica Bollani, Shiro Tsukamoto, Giovanni Isella, Emiliano Bonera, Marco Abbarchi, Stefano Sanguinetti, 'Crystallization and solid state dewetting of amorphous Ge thin films', Poster presentation, ICPS, International Conference, Montpellier, France, 2018.

- Dimosthenis Toliopoulos, Andrea Ballabio, Alexey Fedorov, Sergio Bietti, Monica Bollani, Shiro Tsukamoto, Giovanni Isella, Emiliano Bonera, Marco Abbarchi, Stefano Sanguinetti, 'Optically active AlGaAs layer grown on monocrystalline Ge

Mie Resonators', Poster presentation, PLMCN- International Conference, Moscow, Russia, 2019.

- Dimosthenis Toliopoulos, Andrea Ballabio, Alexey Fedorov, Sergio Bietti, Monica Bollani, Shiro Tsukamoto, Giovanni Isella, Emiliano Bonera, Marco Abbarchi, Stefano Sanguinetti, 'Annealing temperature and Ge amorphous thin film thickness dependence on solid state dewetting process on Si (001) with 1μm SiO 2 layer', 3rd Joint AIC-SILS conference, Rome, 2018.

Outreach activities

- Meet me tonight, European Researchers' Night call, 'Cryptography and quantum cryptography', Milan, Italy, 2018.
- MSC 'Fellow of the week',blog article for 'Quantum Supremacy'.
- Best video award for the short video 'Quantum entanglement and superposition', 2019.
  link: https://www.youtube.com/watch?v=rVNebPOI5uk
- Athens Science Festival, Quantum Cryptography', Athens, Greece, 2019.

  Abstract of the talk: Quantum cryptography is a promising method to secure our telecommunications, eliminating once for all any interception of users or even national and international communication systems. In the past, many tries were completely failed, even if the cryptographic method was sophisticated and complex to transfer the messages from the transmitter to the receiver, since humans always found a solution to solve the cryptographic messages. With quantum cryptography, nature itself can provide us the possibility to secure our messages without any interference with it. Let's take a closer look into this mystery of physics and quantum mechanics.

Acknowledgements

It seems it is quite usual to record acknowledgements by declaring that there are too many debts that need to be repaid. However, there is not such a currency with strong exchange value to give back all the valuable lessons I learn during all these years of this Ph.D thesis. Lessons which at first glance seem to be all constrictive. But, like every story ever told is the result of lessons experienced, and like light interacting with matter, there are constructive and destructive interferences. However, they do not cease to be valuable lessons. The people I met during these years were more than valuable to me and the only way to reply to their help is by expressing my deepest and honest gratitude. First, I would like to thank my supervisor prof. Stefano Sanguinetti in University of Milano – Bicocca who gave me the opportunity to work in such an environment and to benefit from the experience and knowledge of his group in L-NESS and foremost for his patience and collaboration. In the workplace in L-NESS, in Como, where I spent most of my time during these 3 years, I had the chance to meet also prof. Shiro Tsukamoto to whom I own a lot, not only for his collaboration but also because he was the teacher of mine and together with Dr. Sergio Bietti were the two columns of my psychological support and friendly advice. I can't forget to thank Dr. Alexey Fedorov, my closest advisor for the experimental processes. With him I was able to benefit from his lessons about the MBE machine, but I can't forget the countless hours discussing physics and science. The interaction with him was an example of destructive interference at first, but then transformed into constructive interference with fruitful and valuable lessons on how to think like a scientist. The person I would like to thank from the people I met in Como-Milano, is my dearest friend, flatmate and collaborator Artur Tuktamyshev. His calmness and smile were always a way to make

me feel good being around him. I also found the discussions I had with him about our Ph.D thesis extremely helpful along the valuable advice I got from him. Finally, I would like to thank prof. Monica Bollani for the collaboration and discussion I had during my stay in Como.

Except my experience in Como I had the opportunity to meet people during my secondments in Florence and in Marseille. In both places I stayed long enough to interact and meet amazing people who not only were valuable collaborators but also friends of mine. First, I would like to thank prof. Massimo Gurioli, my co – supervisor in Florence. He makes my 6 months stay in Florence unstressed and he shared with me his valuable experience in the photonics field. He always impressed me with his knowledge and his kindness. With him I learned how to scientifically approach experimental data and analyze them towards the assumptions and conclusions. Furthermore, I would like to thank Dr. Francesco Biccari, my collaborator and kind friend. With him I discussed and performed the micro-PL experiments. I learned valuable lessons and I benefited from his experience and together with Andrea Ristori my time in Florence were unforgettable. Andrea is my dear friend where we spend countless hours in lab 6 in LENS. When I think of kind and amazing people I met during my Ph.D he will be the first example.

My second secondment was in France this time and in University of Marseille. In this place I met prof. Marco Abbarchi. I have no words to express how many things I own to him. First of all, he made my stay in Marseille and in his group my favorite 5-month period during the Ph.D. I am amazed by the environment I met in his group. I felt immediately like I was part of the team and thus it motivated me a lot to learn more and more. There were also many times when my friend Marco supported me with my difficulties and made me feel valuable and strong. I will

always be grateful to him. Of course, there I met amazing people and I would like to thank my friends Momo, Jibe, Mehrnaz, Mario, Drisse, Jerome, Ilia and Gabrielle.

Furthermore, I would like to thank my 4photon friends with whom I collaborate during these years. I had an amazing time every time we met for the conferences and workshops. Antonio, Andrea, Leonardo, Giorgos, Adonai, Geoffrey, Meryem, Shivangi, Liang, Panaiot, Piotr, Raja and Jonathan. I hope to have the chance to collaborate again in the future. Furthermore, I would like to thank my parents, Apostolis and Mary for the unconditional support in my life and my sister Dimitra who is always there to support me in any difficulties. The current thesis however, is devoted to my grandfather who died during the writing process of this text. I will always remember him. Finally, last but not least, my best friends Chrysanthos, Nikos, Kostas, Odysseas, Michalis, Notis, Marilena, Maria, Charis, Giannis, Alex and Marco who really stand by my side discussing and listening to me. I will be always grateful for their support and encouragement which are worth more than I can express on paper.

Dimosthenis 2020-2021